Preprints.org

Article

Not peer-reviewed version

Valorization of Tungsten Mining Waste and Clay Residues in the Production of Technical Ceramic Materials for Sustainable Construction and Architectural Rehabilitation

Jorge Alberto Duran-Suarez * , Maria Paz Saez-Perez , Alberto Martinez-Ramirez , Laura Crespo-López

Posted Date: 13 April 2026

doi: 10.20944/preprints202604.0805.v1

Keywords: mining sludge; sustainable ceramic bricks; sintering temperature; vitrification and densification; toxic elements immobilization; microstructural features

Preprints.org is a free multidisciplinary platform providing preprint service that is dedicated to making early versions of research outputs permanently available and citable. Preprints posted at Preprints.org appear in Web of Science, Crossref, Google Scholar, Scilit, Europe PMC.

Copyright: This open access article is published under a Creative Commons CC BY 4.0 license, which permit the free download, distribution, and reuse, provided that the author and preprint are cited in any reuse.

Preprints.org (www.preprints.org) | NOT PEER-REVIEWED | Posted: 13 April 2026 doi:10.20944/preprints202604.0805.v1

Disclaimer/Publisher's Note: The statements, opinions, and data contained in all publications are solely those of the individual author(s) and contributor(s) and not of MDPI and/or the editor(s). MDPI and/or the editor(s) disclaim responsibility for any injury to people or property resulting from any ideas, methods, instructions, or products referred to in the content.

Article

Valorization of Tungsten Mining Waste and Clay Residues in the Production of Technical Ceramic Materials for Sustainable Construction and Architectural Rehabilitation

Jorge Alberto Duran-Suarez [1,*], Maria Paz Saez-Perez [2], Alberto Martinez-Ramirez [1] and Laura Crespo-López [3]

[1] Conservation and Sculpture Department, Faculty of Fine Arts, University of Granada, 18071 Granada, Spain
[2] Building Constructions Department, Advanced Technical School for Building Engineering, University of Granada, 18071 Granada, Spain
[3] Scientific Instrumentation Center, University of Granada, 18071 Granada, Spain
* Correspondence: giorgio@ugr.es

Abstract

Mining and industrial activities generate large volumes of waste, up to 99% of the extracted material, forming a major global residue source. In this context, the valorization of mining sludge for sustainable construction materials gains relevance. This study examines the fabrication of ceramic bricks incorporating mining sludge from the Panasqueira mine, evaluating sludge incorporation levels and sintering temperatures to optimize resource use and reduce environmental impacts. Bricks were produced by blending residual clays from Víznar (Granada, Spain) with Panasqueira sludge at substitution rates of 10, 25 and 50%, and fired at 800, 950 and 1100 °C. The samples were characterized by XRF, XRD, water absorption tests, porosimetry, ultrasound pulse velocity, compressive strength testing, ESEM, leaching analysis and colorimetry to assess their chemical, physical and mechanical behavior. Both clays and sludge are rich in SiO_2 and Al_2O_3, suitable for ceramic processing, while fluxing oxides promote vitrification and densification. Incorporating 25 and 50% sludge reduces porosity, increases ultrasonic velocity and improves mechanical strength, achieving optimal performance at 1100 °C. Moreover, firing immobilizes toxic metals and allows controlled color development, confirming the technical and environmental suitability of these bricks, whose microstructure and stability depend on sludge content and firing temperature, essential factors for sustainable construction and architectural rehabilitation.

Keywords: mining sludge; sustainable ceramic bricks; sintering temperature; vitrification and densification; toxic elements immobilization; microstructural features

1. Introduction

Extractive mining industries constitute one of the most extensively developed activities worldwide. It is estimated that in 2021 approximately 17,896 million metric tons of minerals were produced globally [1], generating millions of tons of waste annually, many of which are classified as hazardous to human health and the environment. Several authors estimate that the largest fraction of the extracted ore, between 97% and 99% of the total mass, consists of solid residues that ultimately end up in waste dumps or storage facilities [2]. This implies that the amount of useful material obtained represents only a minimal portion of the total mineral processed, and this fraction is even smaller in the extraction of noble metals such as gold [3]. Consequently, at least seven billion tons of mine tailings are generated annually worldwide, and a 2.70% annual growth in mining waste is

© 2026 by the author(s). Distributed under a Creative Commons CC BY license.

Preprints.org (www.preprints.org) | NOT PEER-REVIEWED | Posted: 13 April 2026 doi:10.20944/preprints202604.0805.v1

projected for the period between 2026 and 2034 [4]. According to Eurostat statistics, the countries with the highest rates of mining waste generation are Romania, Bulgaria, and Serbia.

Multiple studies address the development of new materials using various wastes generated by the mining industry as secondary raw materials. Conventionally, stony waste produced during mining activities have been used in pavement or road construction [5–7]; as backfilling material in both open-pit and underground mines [8–10]; and in the manufacturing of other construction materials, such as aggregates of different types for concrete production [11], mortars [12], and various ceramic products [13–17]. The feasibility of using mining sludges in glass production has also been explored [18,19]. Currently, the production of geopolymeric materials from mining residues is considered the most promising technology for converting these wastes into new manufactured products due to their high silicon and aluminum content [20–22].

Furthermore, the construction sector demands enormous quantities of resources and materials and accounts for the largest share of waste generated within the European Union. According to Eurostat statistics, in 2020 construction contributed 37.5% of the total waste generated, followed by waste derived from mining and quarrying, which accounted for 23.4%. Together, these sectors represent more than half of the waste generated annually at the European level. Moreover, when establishing a connection between material extraction activities, the manufacture of construction products, and the construction sector itself, the sum of these actions is responsible for between 5% and 12% of total national greenhouse gas emissions [23].

In recent decades, an increased awareness of environmental sustainability has emerged globally and particularly within the regulatory framework of the European Union, notably through the communication of the New Circular Economy Action Plan. In contrast to earlier industrial waste management policies largely based on massive, sometimes uncontrolled and hazardous stockpiling, new strategies have been implemented that focus on both the reduction and the reuse of waste, which is now increasingly regarded as a suitable secondary raw material for the production of new products [24]. This shift has played a decisive role in the management, valorization, and recovery of waste across various industrial sectors.

Currently, the production of construction materials represents the main strategy for the recovery of mining wastes [25–27]. In this context, research efforts worldwide have surged, highlighting the potential for utilizing various by-products—previously deemed unusable—as partial substitutes for primary raw materials in brick production. These industrial waste materials can be incorporated into ceramic pastes in the form of powders and/or aggregates. A substantial body of research focuses on the development of traditional ceramic bricks incorporating organic waste as starting materials [28–30] as well as inorganic waste [31–33]. Furthermore, several authors have demonstrated the feasibility of producing bricks with satisfactory properties using different proportions of mining sludges as raw materials [34–37].

In addition, the enormous consumption of natural resources in general, and of clay deposits in particular, for the manufacture of ceramic products leads to the gradual depletion of non-renewable resources [38]. Therefore, the development of strategies based on the use of by-products as substitutes for traditional raw materials becomes imperative to reduce the demand for primary mineral resources and to prevent landscape degradation [39]. In line with this, the processing of ceramic materials incorporating waste involves the design and initial mixing of the raw materials in predetermined proportions, the shaping of pieces through techniques such as modelling, molding, or extrusion, and finally, sintering, which consists of subjecting these materials to thermal ranges between 900 and 1260 °C. As a result of this methodological process, thermally transformed materials with adequate chemical and physical properties are obtained, and in some cases, even with superior performance compared to commercial products.

The aim of this study is to obtain new ceramic materials based on the recycling of mining sludges from the Panasqueira mine (Portugal). Numerous previous investigations have highlighted the potential use of waste generated by the Panasqueira mining activity for the production of new sustainable materials with diverse applications. For instance, [40] developed geopolymer composites

© 2026 by the author(s). Distributed under a Creative Commons CC BY license.

Preprints.org (www.preprints.org) | NOT PEER-REVIEWED | Posted: 13 April 2026 doi:10.20944/preprints202604.0805.v1

incorporating coarse mining residues for the production of terrazzo tile prototypes. In the doctoral thesis by [41], new ceramic materials were designed and produced using mineral waste, with the waste incorporated into the mixtures in high proportions (up to 90%). Other authors, such as [42], proposed various construction materials for civil engineering applications in which mining waste play a central role, bituminous mixtures, concretes, and other materials for prefabricated elements, all based on the concept of alkali-activated materials. Similarly, [43], demonstrated the production of geopolymeric compounds from mixtures (in different proportions) of tungsten mining sludges and brick waste using sodium silicate and sodium hydroxide as alkaline activators. Along the same lines [44], geopolymer-based foams incorporating residual mining sludges and expanded cork granules through the chemical foaming technique with aluminium powder. More recently, other researchers have explored the design and production of magnesium-based mortars cured under accelerated carbonation, capable of absorbing surrounding CO_2 and incorporating mining sludges, among other industrial residues, as aggregates [45].

This work proposes a new alternative for the valorization of sludges derived from the mining activity of Panasqueira, consisting in the production of bricks doped with these by-products. In addition to reducing the amount of clay required for ceramic manufacture, the study aims to optimize the firing temperature of the designed materials without compromising the quality of the final products. Another objective is to determine the improvement of the physical and mechanical properties of the doped ceramics according to the different percentages of mining sludges incorporated (10, 25, and 50 wt%) and/or firing temperatures applied (800, 950, and 1100 °C). Finally, this research seeks to contribute to environmental sustainability through the production of new materials based on the valorization of solid waste, reducing their disposal and accumulation in landfills.

The amount of mining sludges incorporated into the manufacture of the bricks was selected based on results reported by other researchers. In general, waste contents above 60–70% tend to impair the performance of the final products [46,47], which is why no more than 50% sludge was added to obtain manufactured materials with suitable properties. Likewise, the working temperatures were chosen according to previous studies on brick production using similar starting materials [39,48]. Furthermore, this selection is motivated by the need to assess potential mineralogical and textural changes as a function of the intensity of applied thermal treatment.

2. Materials and Methods

The materials used to design the sustainable bricks products consist of natural clay residues derived from ceramic industries and extractive mining waste primarily tungsten-bearing tailings together with water for homogenization and compaction of the mixture, followed by subsequent drying and firing at different ceramic transformation temperatures.

The clayey raw material used for the manufacture of the technical bricks was supplied by the company Cerámica Castillo Siles S.L., located in the municipality of Víznar (Granada Province, Spain). As ceramic additives, mining tailings sludge originating from the residual deposits of the Panasqueira mine, specifically from the Cabeço do Pião and Aldeia da Panasqueira areas, located in the Beira Interior region of Portugal, was incorporated into the formulations (Figure 1).

© 2026 by the author(s). Distributed under a Creative Commons CC BY license.

Preprints.org (www.preprints.org) | NOT PEER-REVIEWED | Posted: 13 April 2026 doi:10.20944/preprints202604.0805.v1

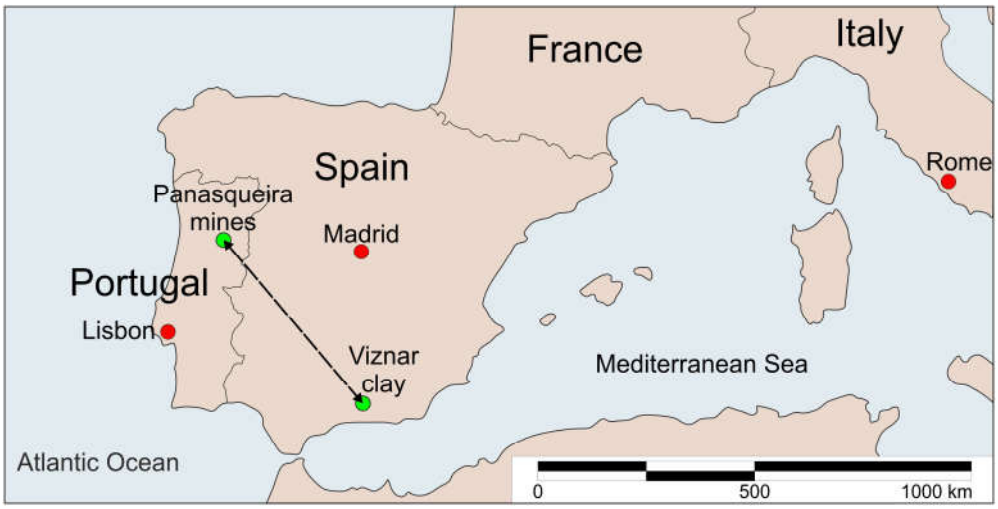

Figure 1. Geographical location of the origin of the raw materials. The arrow links the two sites under study: the Panasqueira area in the Beira Interior region (GPS 40°10′08″N, 7°45′25″W; elevation 764 m), Portugal, and the clay deposits of Víznar in the province of Granada, Spain (GPS 37°13′58″N, 3°33′16″W; elevation 1066 m).

Geologically, the Víznar area (Granada, Spain) is composed of carbonate rock massifs dominated by limestones and dolomites associated with the Granada Basin. The region exhibits significant Neogene–Quaternary sedimentary sequences and includes various lithologies, such as Jurassic–Cretaceous limestones and dolomites, Neogene conglomerates, sandstones and sands, and Quaternary silts and clays. These clayey materials constitute the natural extractive base for the local ceramic industry [49].

The geology of the Panasqueira region (Covilhã, Portugal) consists of marine sedimentary sequences of Ediacaran and Cambrian age, dominated by schists and greywackes, affected by low-grade metamorphism and Hercynian deformation. The area includes post-tectonic granite intrusions, altered granitoids and extensive quartz vein systems hosting metallic mineralisations of tungsten–wolframite, tin–cassiterite, copper and beryllium [50,51].

The Panasqueira mining complex, located in the Serra da Estrela and near the Serra do Açor and the Zêzere River, is internationally recognised for its long extractive history and its production of strategic minerals since the mid-19th century and continuing to the present. Tungsten and tin have been the main exploited resources, although other mineral species such as cassiterite and beryl, as well as metals such as copper and lead, have also been documented [42,50,52–56]. Tungsten extraction constitutes the most significant mining activity in Panasqueira. This metal is considered of strategic importance for several industrial sectors, including high-strength steel production, electronics and the chemical industry. The Panasqueira tungsten deposit is one of the largest in Europe and has historically represented a key supply source for the international market [57–59].

2.1. Experimental Process for Traditional Bricks with Mining Sludges

The ceramic pastes were formulated by blending natural clay residues from Víznar (Granada, Spain) with mining tailings sludge from the Panasqueira mines (Covilhã, Portugal). Three additive proportions were established by weight: 10% (MC10), 25% (MC25) and 50% (MC50). Additionally, control samples composed exclusively of clay residues (CC) were prepared as reference specimens to comparatively assess the influence of the mining tailings on the properties of the newly developed ceramic materials. The four brick typologies were fired at 800, 950 and 1100 °C. The main characteristics of the resulting ceramic samples are summarised in Table 1.

Table 1. Ceramic sample groups showing the percentage of mining sludge added relative to the additive-free control samples, the ceramic firing temperatures, and the water volume used per kilogram of mixture. Target samples (without mining sludges) and sustainable bricks made of clay and mining sludge at 10, 20, and 50%.

© 2026 by the author(s). Distributed under a Creative Commons CC BY license.

Preprints.org (www.preprints.org) | NOT PEER-REVIEWED | Posted: 13 April 2026 doi:10.20944/preprints202604.0805.v1

	Tª (ºC)	Target samples	Sustainable bricks (wt% of sludge)		
			10%	25%	50%
	800	CCL	MC10L	MC25L	MC50L
	950	CCM	MC10M	MC25M	MC50M
	1100	CCH	MC10H	MC25H	MC50H
Water (mL)		300	235	225	150

The ceramic pastes were formulated by dry-mixing the clayey raw material with the mining sludge, except for the control samples (without sludge), to which water was subsequently added until the required plasticity was achieved. The resulting mass was manually homogenised and shaped in detachable wooden moulds with a capacity for pieces measuring 16 × 12 × 4 cm. After filling the mould, the surface was levelled using a wooden strip. Once the initial moisture loss had occurred, the moulds were removed and the shaped bricks were cut into cubic specimens of 4 × 4 × 4 cm, yielding a total of twelve standardised samples per batch for the different tests.

The hygroscopicity of the wooden mould facilitated demoulding, allowing the pieces to be cut 7 h after fabrication. Subsequently, the specimens were dried under controlled laboratory conditions (22 ± 5 °C; 45 ± 2% RH) for three days. A total of four samples per group were produced, resulting in 48 specimens overall. Prior to firing, all samples were oven-dried at 60 °C for 24 h to minimise adverse effects during firing associated with rapid moisture removal. Each series of specimens was subjected to thermal cycles in a Herotec CR-35 electric kiln (T_max = 1350 °C), following a common protocol consisting of a heating rate of 120 °C/h from room temperature to the target peak temperature, a 30-minute dwell at the selected temperatures (800, 950 and 1100 °C), and free cooling to room temperature (Figures 2 and 3).

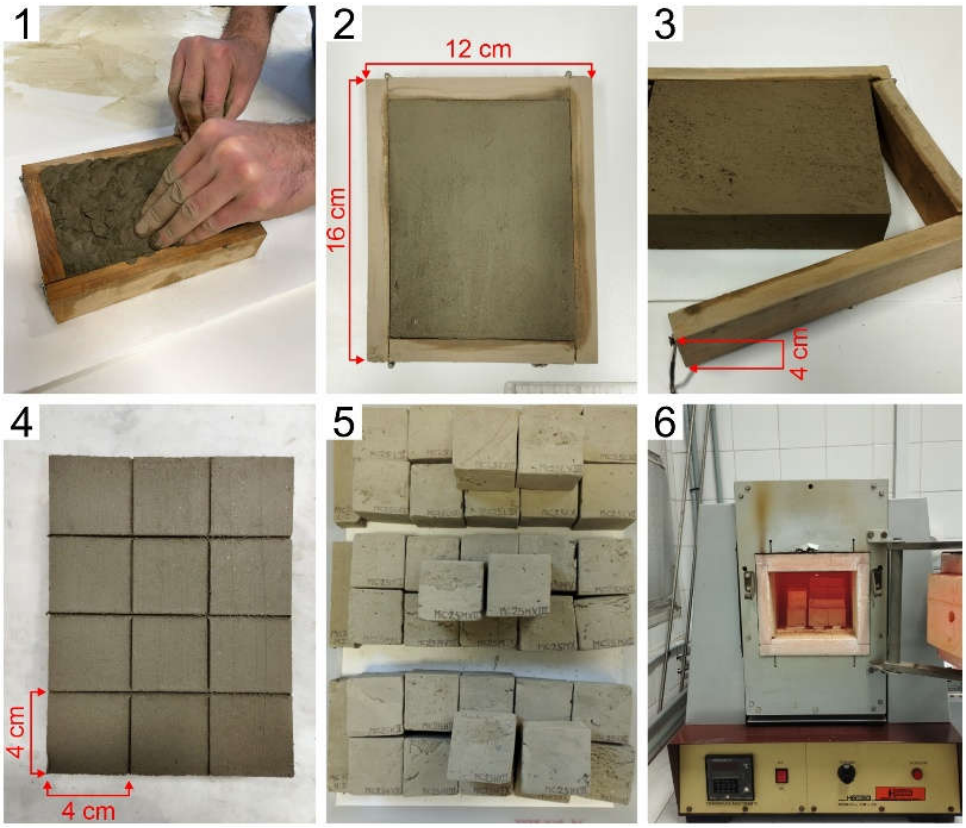

Figure 2. Preparation process of the specimens used for the manufacture of tungsten-residue-based bricks. Steps 1 to 6: mixing and moulding of the paste, levelling of the mixture, removal of the mould frame, cutting into twelve 4 × 4 × 4 cm samples, oven drying, and firing according to the programmed heating schedule at the selected temperatures.

© 2026 by the author(s). Distributed under a Creative Commons CC BY license.

Preprints.org (www.preprints.org) | NOT PEER-REVIEWED | Posted: 13 April 2026 doi:10.20944/preprints202604.0805.v1

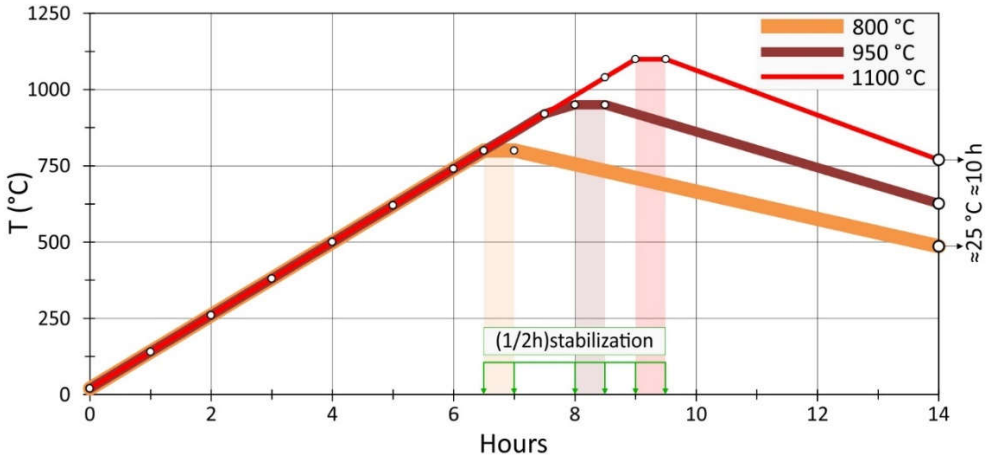

Figure 3. Firing curves of the studied samples, showing a heating rate of 120 °C/h up to the target temperature for each group, a 30-minute dwell at the maximum temperature reached, and free cooling to approximately 25 °C over a period of 10 hours.

2.2. X-Ray Fluorescence

The elemental chemical composition of the raw materials was determined by X-ray fluorescence (XRF) using a PANalytical Zetium wavelength-dispersive sequential spectrometer equipped with a rhodium-anode ceramic tube, a 4 kW generator, and a decoupled θ/2θ goniometer. For major-element analysis and semiquantitative analysis, the samples were prepared as fused beads and pressed pellets, respectively. Semiquantitative values were obtained using PANalytical's Omnian software package. Four samples in total were analyzed using this technique.

2.3. X-Ray Diffraction

The mineralogical characterization of the raw materials and of the different ceramic typologies was performed by X-ray diffraction (XRD) using a PANalytical X'Pert PRO diffractometer. All samples were finely ground in an agate mortar and subsequently dry-sieved to obtain the <80 μm fraction. The working conditions were: CuKα radiation, 45 kV and 40 mA, a scanning range of 3–70° (2θ), and a step speed of 0.1° 2θ·s^{-1}. Mineral phase identification was carried out, and a total of fourteen samples were examined using this technique.

2.4. Hydric Tests

Water absorption by free immersion and the subsequent drying behavior were determined according to standards [60,61], respectively. Three specimens per brick typology were tested, yielding a total of 36 samples. All tests were performed under controlled laboratory conditions (20 ± 5 °C; 60 ± 5% RH) using distilled water. Mass variations were recorded with a Radwag PS 6000/C/2 balance with a precision of ±0.1 g. A total of eighteen samples were examined in the absorption and desorption test.

The water content by weight and the absorption coefficient for each sample were calculated using Equation 1 (EQ1) and Equation 2 (EQ2), respectively. The drying index was determined from the integral of the drying curve, following Equation 3 (EQ3).

EQ1

$$Al = \frac{M_s - M_0}{M_0} 100$$

EQ2

$$Ac = \frac{M_s - M_0}{Vol}$$

© 2026 by the author(s). Distributed under a Creative Commons CC BY license.

Preprints.org (www.preprints.org) | NOT PEER-REVIEWED | Posted: 13 April 2026 doi:10.20944/preprints202604.0805.v1

EQ3

$$ID = \frac{\int_{t_0}^{t_f} f(\Delta M)dt}{IA * t_f}$$

2.5. Mercury Intrusion Porosimetry

The pore system, its quantification, and the pore-size distribution ranges were evaluated by mercury intrusion porosimetry (MIP) using an AutoPore IV 9500 V1.07 porosimeter (Micromeritics). Prior to analysis, the specimens were pre-dried with silica gel in a hermetically sealed container for seven days. The accessible porosity and the percentage pore-size distribution for the twelve typologies tested (mesopores, macropores and air voids/cracks) were determined according to the procedures outlined in reference [62]. Twelve samples in total were used in the MIP test.

2.6. Ultrasonic Pulse Velocity

The ultrasonic pulse transmission velocity was measured using a Tico Proceq device equipped with 54 kHz transducers of 50 mm diameter. The test was performed in direct transmission mode, using an aqueous gel couplant (TELIC S.A.U.). All specimens were measured, with four samples per group. Measurements were taken in the three spatial directions, both before and after firing, following standard [63], which specifies the laboratory determination of pulse velocities and ultrasonic elastic constants of rock. The propagation velocity of P-waves was recorded in m/s. A total of sixteen samples were used, with three measurements performed on each face of the hexahedral sample.

2.7. Compressive Strength

Uniaxial compressive strength was evaluated using a Shimadzu Autograph AGS-X testing machine, applying an increasing load at a crosshead displacement rate of 1 mm/min until specimen failure. The maximum load capacity of the equipment was 45 kN. The tests were performed in accordance with standard [64–66], which specify the determination of compressive strength in natural and dimension stone materials. A total of thirty-six specimens were tested, corresponding to three samples per typology.s

2.8. Environmental Scanning Electron Microscopy

Morphological and textural characterization was carried out using environmental scanning electron microscopy (ESEM) with a high-resolution FEI QuemScan 650FEG operating in high-vacuum mode (<6 × 10^{-4} Pa), equipped with secondary electron detectors (SED) and backscattered electron detectors (BED). Chemical microanalysis was performed using a Dual EDS XFlash 6/30 X-ray system (Bruker). Images, spectra and elemental distribution maps were processed using the CDuranorrelative Workflow and Maps Tiling & Stitching software packages. All samples were coated with a carbon film prior to analysis. Twenty-six samples in total were used for the ESEM study.

2.9. Leaching Test

The leaching test was carried out following the procedure described in [67]. The method is based on extracting the aqueous phase from a suspension of a previously milled solid sample and determining the concentration of chemical elements released into the aqueous medium. The procedure consists of taking a representative solid sample (20 ± 0.05 g), subsequently grinding it in an agate mortar and sieving it to 150 μm; oven-drying the material at 150 ± 5 °C to constant mass; transferring it to a 500 mL volumetric flask; and adding the leaching liquid (200 mL of deionized water).

The solid and liquid components were agitated at 400 rpm at room temperature for 60 ± 2 minutes. After 15 minutes from the end of the extraction, the suspension was filtered through an ash-

© 2026 by the author(s). Distributed under a Creative Commons CC BY license.

Preprints.org (www.preprints.org) | NOT PEER-REVIEWED | Posted: 13 April 2026 doi:10.20944/preprints202604.0805.v1

free paper filter for gravimetric analysis. The filtrate (eluate) was collected, and the concentrations of leached chemical elements (μg/L) were determined by semiquantitative multi-element analysis using inductively coupled plasma mass spectrometry (ICP-MS) with a NexION 300X instrument (Perkin-Elmer), which provides detection limits in the ng/L range for most elements, a linear dynamic range of 8–10 orders of magnitude, and semiquantitative precision better than 30%.

Using this procedure, both the mining sludge sample and the ceramic samples fired at 800 and 1100 °C were analyzed, for sludge incorporation levels of 10%, 25% and 50%. The leachate obtained from the mining sludge was used as the reference pattern against which the leachates from the ceramic samples were compared. The acidity or basicity of the eluates was also monitored using environmental pH sensors developed by [68], with a precision of ±0.1 pH units. pH measurements were conducted in aqueous media. Sixty samples in total were used in this test.

2.10. Colorimetry

The chromatic properties of the raw materials and the ceramic products were determined using a Konica Minolta CM-2600d/2500d spectrophotometer. Measurements were performed under CIE D65 illumination [69], recording the L (lightness), a and b* (chromaticity) coordinates using the Spectra Magic software. A total of fourteen samples were analyzed, and in accordance with standard [69], mean values were obtained from six measurements taken on each face of the hexahedral specimens.

3. Results

3.1. X-Ray Fluorescence (XRF)

The elemental chemical composition of the raw materials is presented in Table 2. Both materials exhibit high silicon oxide (SiO_2) contents and substantial proportions of aluminium oxide (Al_2O_3) and iron oxide (Fe_2O_3). The clay from the study area also contains notably elevated concentrations of calcium oxide (CaO), whereas magnesium oxide (MgO) and potassium oxide (K_2O) appear in comparatively lower amounts. The clay displays a higher loss on ignition (LOI) than the mining sludges (13.86% and 4.60%, respectively), primarily due to the release of structurally bound water inherent to clay minerals, as well as the decarbonation of calcium carbonates.

The major-element analysis underscores the predominance of SiO_2 and Al_2O_3, which together account for more than two-thirds of the total composition in both raw materials (clay >60%; sludge >70%). This chemical configuration is particularly favourable for densification and hardening during high-temperature firing, promoting the formation of stable ceramic structures. Silicon oxide acts as the principal network former in the vitrified matrix, a key component in ceramic and glass production, conferring rigidity, mechanical strength, thermal stability, and chemical durability. Aluminium oxide, in turn, functions as a network stabiliser and reinforcing agent within the silicate framework, enhancing hardness as well as thermal and mechanical resistance [70–73].

Table 2. Results of the elemental chemical analysis of major oxides obtained by XRF for the clay material and the mining residues, together with the semi-quantitative analysis of the sludges (wt%).

Major (%)	SiO2	Al2O3	Fe2O3	MnO	MgO	CaO	Na2O	K2O	TiO2	P2O5	Zr	LOI (%)	∑ (%)
Clay	47,46	14,77	5,55	0,07	3,78	10,11	0,67	2,58	0,77	0,12	0,019	13,86	99,74
Sludge	57,72	13,15	11,14	0,11	1,92	0,66	0,9	2,41	0,56	0,34	0,013	4,60	93,51
Semi-Q (%)	Sr	Cr	Ba	Ni	Nb	Rb	As	Y	Zn	Sn	Co		
Sludge	0,009	0,013	0,019	0,009	0,001	0,035	1,139	0,002	0,759	0,046	0,010		
Sludge	Cu	Ga	Cd	I	Ce	W	Bi	F	Cl	Au	SO3		
	0,201	0,002	0,013	0,046	0,016	0,147	0,005	1,213	0,015	0,004	5,836		

In addition, regarding the major-oxide analysis, the presence of alkali and alkaline-earth oxides is noteworthy due to their role as fluxing agents. These include Na_2O, which lowers the melting point

© 2026 by the author(s). Distributed under a Creative Commons CC BY license.

Preprints.org (www.preprints.org) | NOT PEER-REVIEWED | Posted: 13 April 2026 doi:10.20944/preprints202604.0805.v1

and promotes the formation of a liquid–glass network; K_2O, which stabilises the vitreous phase; CaO, which enhances vitrification and contributes to matrix densification; and MgO, which provides phase stability and favours the development of neoformed phases. Together with these, the previously mentioned Fe_2O_3 also acts as a flux under the oxidising atmosphere in which the sustainable bricks were fired, in addition to contributing to the formation of intermediate mineral phases such as hematite [74–79].

Regarding the semi-quantitative elemental composition of the mining sludges, the XRF results reveal a high concentration of arsenic (As), reaching 1.139 wt%, which confirms their potentially hazardous character. Lower concentrations of chromium (Cr) and cadmium (Cd) were also detected, together with the presence of other elements of interest such as rubidium (Rb), tin (Sn), zinc (Zn), copper (Cu), and tungsten (W). It is also noteworthy that fluorine (F) exhibited the highest elemental concentration recorded (1.213 wt%). Of particular significance is the role of several minor elements as fluxing agents: strontium (Sr), which promotes the formation of liquid phases; barium (Ba), which acts both as a flux and as a catalyst of the glassy network [80]; zinc (Zn), which reduces the viscosity of the liquid phase in ceramics; rubidium (Rb), which serves as a flux and glass-network modifier, contributing to a lower viscosity of the liquid phase; and fluorine (F), whose relatively high proportion, despite being a minor constituent, acts as a flux by reducing viscosity and enhancing the vitrification of ceramic matrices [81].

The XRF analysis, together with the chemical characterization of the raw materials, both the clay itself and the mining sludges, demonstrates that the preparation of the ceramic products is, a priori, supported by highly favourable compositional properties across a wide thermal window. This allows us to conclude that these raw materials exhibit excellent suitability for ceramic technology. Individually, the raw materials can sustain conventional ceramic firing ranges between 900 and 1250 °C [82–85], largely due to their SiO_2 and Al_2O_3 contents, which can promote mullite formation, along with other components that act as densifying agents and fluxes. In addition, the proposed clay–sludge mixtures present optimal firing ranges that should fall within approximately 900–1125 °C for the 90–10% blend, 1050–1175 °C for the 75–25% blend, and 1100–1225 °C for the 50–50% blend.

3.2. X-Ray Diffraction (XRD)

The XRD results for the raw materials, clay and sludges (Figure 4), reveal that the detected phases, chlorite, illite, paragonite, kaolinite, quartz (highly predominant), calcite, microcline, dolomite, muscovite, clinoclore and magnetite, provide the compositional basis for the successful production of functional ceramic materials. This is particularly relevant for the manufacture of sustainable bricks derived from the recycling of the aforementioned clay and sludge materials. These mineralogical assemblages are consistent with the chemical composition of the raw materials and supply essential components for ceramic manufacturing. In particular, kaolinite and illite, together with muscovite and paragonite, constitute the principal contributors of Al_2O_3 and SiO_2, which under optimal firing conditions can promote the formation of secondary mullite and an aluminosilicate glassy phase [86,87].

Moreover, the significant contribution of microcline (K) and paragonite (Na) is noteworthy, as they act respectively as sources of K-feldspar and sodium, both functioning as fluxes within the mixture and consequently lowering the sintering–vitrification temperature. Their presence promotes the formation of an adhering liquid phase among the various compounds and grains [88,89]. Similarly, chlorite, clinoclore and illite, due to their variable iron contents, favour the formation of hematite depending on the firing temperature. The influence of hematite is not limited to modifying the color of the ceramic products; rather, it also behaves as a neoformed phase capable of occupying pores in the final material, thereby enhancing ceramic technological performance, in a manner comparable to the role of mullite [90,91]. Furthermore, the carbonates present in calcite and dolomite may contribute to lowering the melting point of the mixture.

© 2026 by the author(s). Distributed under a Creative Commons CC BY license.

Preprints.org (www.preprints.org) | NOT PEER-REVIEWED | Posted: 13 April 2026 doi:10.20944/preprints202604.0805.v1

Finally, the substantial presence of quartz leads to the formation of secondary silicates, contributes to stoichiometric balance, minimizes deformation and shrinkage in ceramic materials, and enhances the mechanical strength of the final ceramic products [92,93].

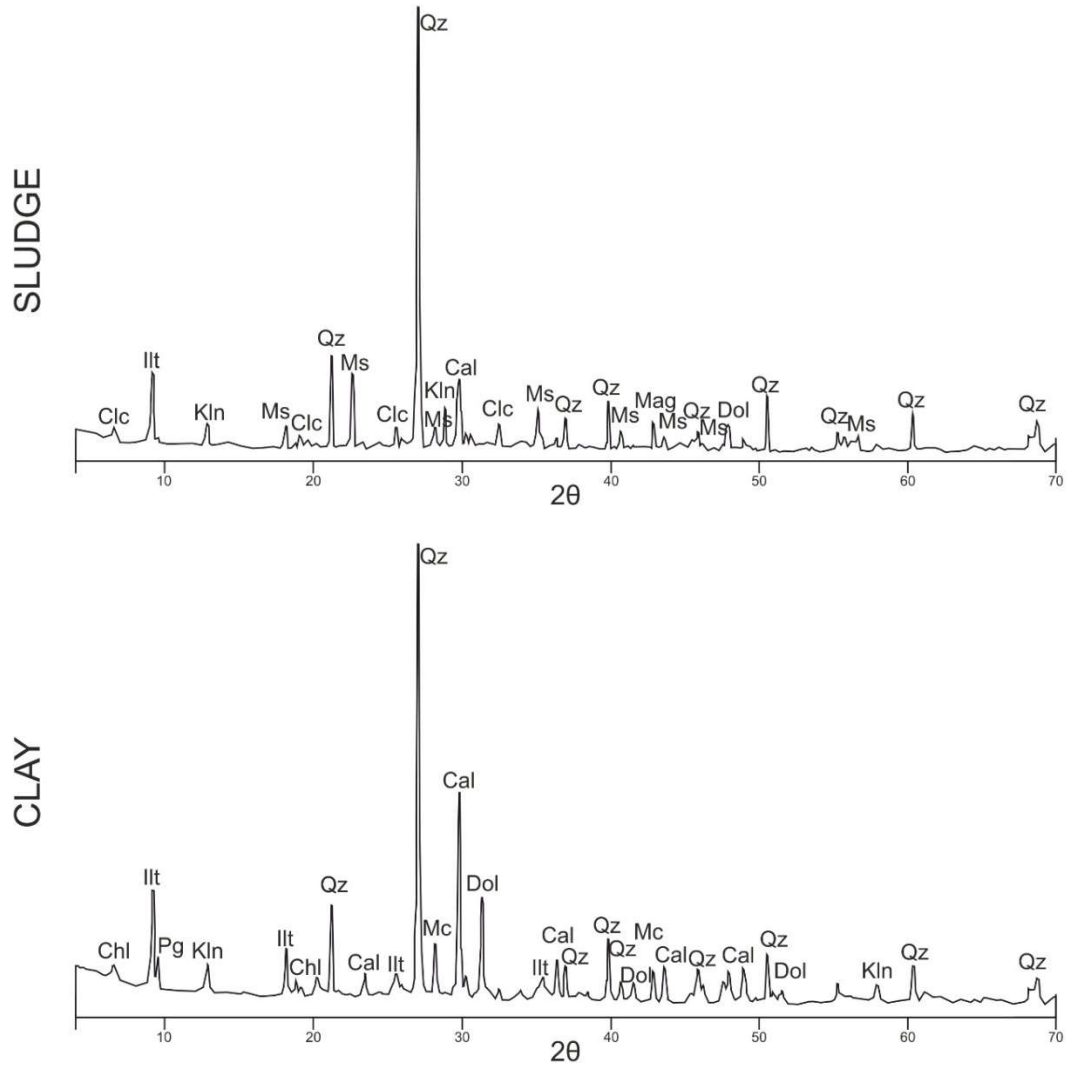

Figure 4. Mineralogy of the raw materials (clay and sludges) obtained from X-ray diffraction analysis. According to [94,95]. Chl = chlorite; Ilt = illite; Pg = paragonite; Kln = kaolinite; Qz = quartz; Cal = calcite; Mc = microcline; Dol = dolomite; Ms = muscovite; Clc = clinoclore; Mag = magnetite.

The results obtained for the CC ceramic samples (control ceramics without tungsten-mining additives) indicate that the clay-based raw materials contain the following minerals (Figure 5): chlorite, illite, paragonite, kaolinite, quartz, calcite, microcline, and dolomite. As a consequence, slight, moderate, and substantial mineralogical transformations occur across the three thermal ranges applied for the preparation of these reference ceramics, produced without mining additives. At 800 °C, only illite, quartz, calcite, and hematite are detectable, with a very limited amorphous phase. These features are likely related to the dehydroxylation of the constituent clays (illite, kaolinite, and paragonite), leaving remnants of illite that remain only partially transformed, either as thermally unaltered residues or as material lacking long-range order, that is, displaying a partially amorphous structure. Calcite is still present at this temperature because decarbonation is incomplete, while hematite is observed, likely derived from the breakdown of chlorites and/or micas [96]. Quartz remains thermally stable at this temperature.

© 2026 by the author(s). Distributed under a Creative Commons CC BY license.

Preprints.org (www.preprints.org) | NOT PEER-REVIEWED | Posted: 13 April 2026 doi:10.20944/preprints202604.0805.v1

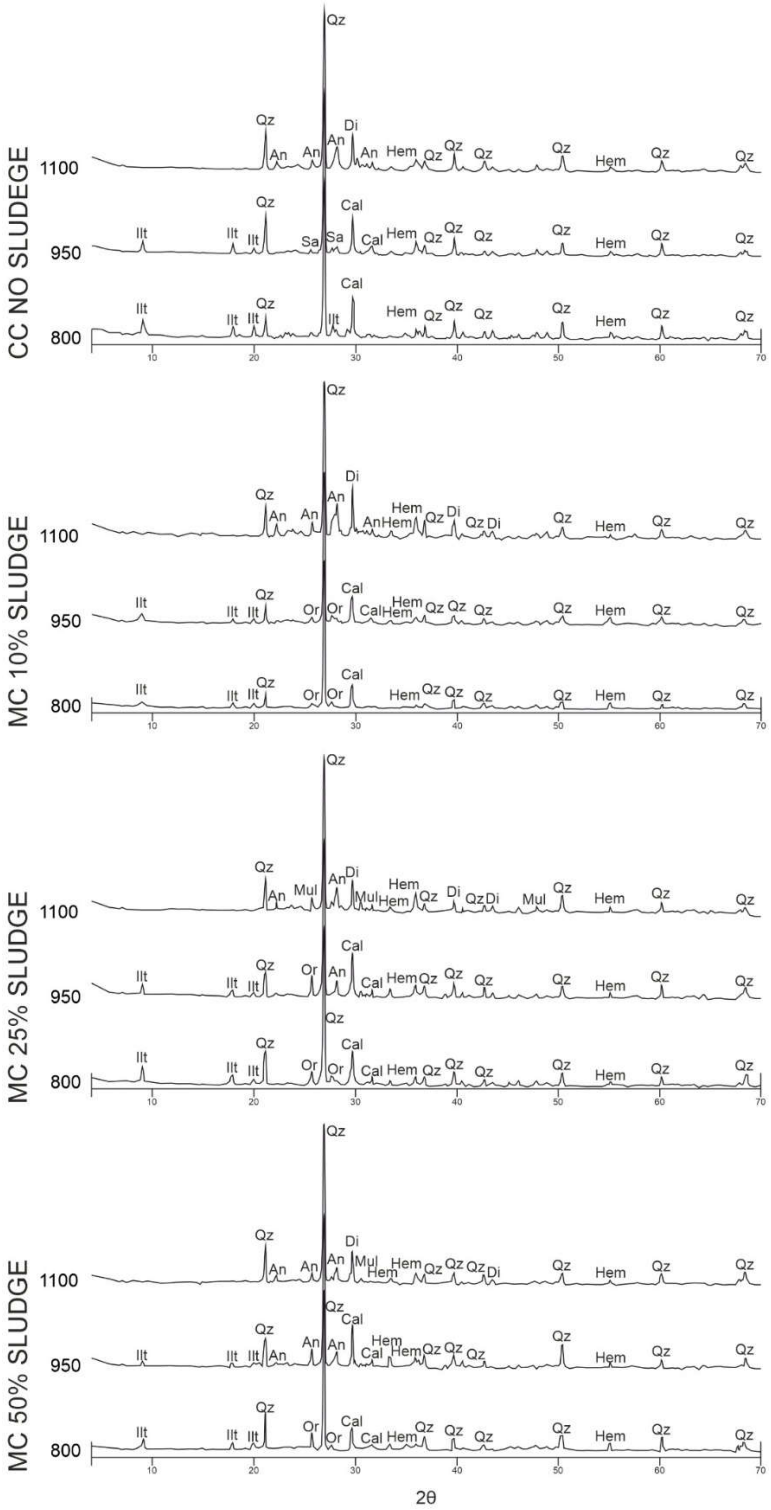

Figure 5. Mineralogy of ceramics without tungsten-mining residues (CC) and with tungsten-mining residues incorporated at 10% (MC10), 25% (MC25), and 50% (MC50), fired at 800, 950, and 1100 °C, obtained from X-ray diffraction analysis. According to [94,95]. Ilt = illite; Qz = quartz; Or = orthoclase; Cal = calcite; Hem = hematite; Sa = sanidine; An = anorthite; Di = diopside; Mul = mullite.

In summary, the ceramic products fired at 800 °C exhibit very limited ceramic maturity in the strict sense, due to the almost complete absence of stable crystalline phases and vitreous material. At 950 °C, illite is still detected as a remnant phase, indicating incomplete dehydroxylation; sanidine appears as an alkali feldspar, likely derived from the mobilization of microcline and paragonite;

© 2026 by the author(s). Distributed under a Creative Commons CC BY license.

Preprints.org (www.preprints.org) | NOT PEER-REVIEWED | Posted: 13 April 2026 doi:10.20944/preprints202604.0805.v1

calcite persists due to the refractory nature of carbonates, which prevents full decomposition at this temperature, or possibly as a product of reprecipitation; and both hematite and quartz remain stable.

In the control ceramic (CC) fired at 1100 °C, the mineralogical assemblage becomes significantly simplified, comprising exclusively quartz, anorthite [97], diopside [98], and hematite, the latter acting as a stable or recrystallized phase derived from chlorite breakdown. Illite and sanidine disappear, likely incorporated into the feldspathic amorphous matrix and vitreous phase, while other phases emerge. Anorthite forms from the decomposition of calcite and dolomite, which at this temperature react with aluminosilicates originating from illite and/or kaolinite, producing a ceramic body with high firing maturity and a high degree of sintering, thereby imparting hardness and thermal stability to the final product.

Similarly, diopside develops as a result of ceramic metamorphism involving Ca (from calcite), Mg (from calcite or chlorite), and Si (from quartz or even kaolinite). Its presence at this temperature reflects the calcareous chemical character of the precursor clays, in this case from the clay residue [99,100].

With regard the ceramics incorporating mining residues (Figure 5), particularly those composed of 10% residue and 90% clay, the mineral phases identified are as follows: at 800 °C, illite, quartz, orthoclase, calcite and hematite;
similarly, at 950 °C, illite, quartz, orthoclase, calcite and hematite are still present. However, at 1100 °C, illite, orthoclase and calcite disappear, giving way to new or persistent phases such as quartz, anorthite, diopside and hematite.

The overall behaviour is relatively similar to that observed in the control ceramics, with the distinctive feature of the incorporation of orthoclase at the two lower temperature ranges (800–950 °C), derived from other potassium-bearing minerals such as microcline, illite, muscovite or paragonite. Illite persists up to the intermediate temperature (950 °C), reflecting incomplete dehydroxylation and the presence of clay minerals that are not yet thermally altered, together with calcite that has not undergone full decarbonation. Likewise, hematite appears at all temperatures as a pore-filling phase, originating from the breakdown of chlorite, micas and magnetite present in the mining residues, the latter derived from Fe and associated with redox processes during firing.

The appearance of anorthite at 1100 °C is consistent with reactions involving Ca, Al and Si, together with a relative dolomitisation reflected by the formation of diopside, an association of Ca, Mg and Si that forms through reactions between the clay minerals and free silica, producing plagioclase and pyroxene crystals. Orthoclase and illite dissolve into the liquid and glassy phase due to the dissolution or volatilisation of potassium during firing. Quartz remains stable across all temperatures, while the presence of anorthite and diopside at 1100 °C indicates that the resulting ceramic body exhibits optimal technological properties, including increased densification, reduced porosity, high hardness and enhanced thermal-shock resistance [101–103].

For the ceramics containing 25% mining residues and 75% clay residues, the mineral phases identified are as follows: at 800 °C, illite, quartz, orthoclase, calcite and hematite; at 950 °C, illite, quartz, orthoclase, anorthite, calcite and hematite; and at 1100 °C, quartz, anorthite, mullite, diopside and hematite. On the one hand, the higher proportion of tungsten-mining residues increases the availability of carbonates and magnesium in the thermal reactions. On the other hand, at the lowest temperature (800 °C), the behaviour resembles that observed in the 10% mixture, where the resulting material does not yet exhibit fully developed ceramic characteristics. Illite remains undecomposed; orthoclase persists due to the presence of potassium, undergoing recrystallization and exhibiting partial thermal stability; calcite is still present due to incomplete decarbonation; and hematite is derived from Fe-bearing components in the starting materials.

At 950 °C, in addition to the newly formed mineral phases, early anorthite appears as a consequence of the increased availability of Ca, the likely smaller particle size and, consequently, greater specific surface area, and the onset of a liquid phase due to potassium released from orthoclase and illite acting as fluxes within the mixture [104,105].

© 2026 by the author(s). Distributed under a Creative Commons CC BY license.

Preprints.org (www.preprints.org) | NOT PEER-REVIEWED | Posted: 13 April 2026 doi:10.20944/preprints202604.0805.v1

At 1100 °C, mullite emerges alongside anorthite and diopside, indicating the development of ceramic quality. Mullite formation is attributed to the high reactivity of Al and Si, likely derived from minerals such as kaolinite. In this residue proportion, the early formation of anorthite, occurring at temperatures lower than expected (≈1000 °C), is indicative of improved ceramic technological performance, manifested through increased densification, higher refractoriness, and greater hardness. Together with mullite, these phases confer optimal mechanical strength and high refractory performance to the ceramic products [106,107].

In the mixture containing 50% tungsten-mining residues and 50% clay residues, the mineral phases identified are as follows: at 800 °C, illite, quartz, orthoclase, calcite and hematite; at 950 °C, illite, quartz, anorthite, calcite and hematite, where orthoclase is replaced by anorthite at this temperature; and at 1100 °C, the phase assemblage matches that of the 25%-residue mixture, consisting of quartz, anorthite, mullite, diopside and hematite. The results at 800 °C and 1100 °C are therefore essentially identical to those observed in the mixture with 25% mining residues, with the only differences in neoformed phases occurring at the intermediate temperature of 950 °C. This behaviour is attributed to the reactive sensitivity of Ca and Mg toward the formation of a liquid phase within the 850–1000 °C interval, likely enhanced by the smaller particle size and corresponding increase in specific surface area. The partial formation of a liquid phase acts as a nucleation medium for adjacent materials, and overall, the higher proportion of tungsten-mining residues modifies the metastability of the mixture. Whereas the 25% mixture retains orthoclase and illite, with incipient anorthite not yet detectable by X-ray diffraction, the 50% mixture suggests a higher availability of Ca and Mg, together with increased nucleation–diffusion effects facilitated by the emerging liquid phase [108], and greater interparticle contact resulting from the larger specific surface area.

Taken together, the system exhibits enhanced chemical reactivity and a favourable transition toward thermodynamically more stable phases, such as anorthite, at the expense of metastable phases, notably orthoclase.

It appears evident that as the proportion of tungsten-mining residues increases, up to a theoretical limit at which an excess of fluxing agents could lead to over-melting of the ceramic bodie, and when medium-to-high firing temperatures (950–1100 °C) are applied, the resulting materials exhibit enhanced ceramic performance. This improvement is associated with the formation of a larger amount of stable and densifying phases, in which anorthite and diopside contribute to increased mechanical and thermal resistance while reducing porosity and promoting compaction in the sustainable ceramic bodies.

Similarly, greater chemical reactivity is observed, and consequently increased sintering, due to the higher availability of Ca and Mg, which act as fluxes within these temperature ranges, promoting the formation of a liquid phase and thereby yielding higher density, improved mechanical strength and reduced porosity. Finally, the metastability of the resulting ceramic materials diminishes, giving rise to thermodynamically more stable phases, which enhances durability and strengthens the sustainable value of the final products [109–111].

The absence of mullite in the ceramics produced with tungsten-mining residues and clay residues in a 10–90% proportion indicates a relative drawback in terms of ceramic technological quality (i.e., ceramics with lower refractoriness and earlier vitrification). This absence may be attributed to an alumina deficiency within the kaolinite–illite–muscovite system, and even paragonite, which may be partially diluted by the excess of calcium, magnesium and carbonates in general, thereby limiting the availability of essential aluminosilicates required for mullite nucleation. It may also reflect a greater tendency for the system to form anorthite and diopside instead of mullite, as the Ca and Mg present exert a partial sequestration effect on Al and Si. Furthermore, the early development of a liquid–glassy (amorphous) phase may inhibit the crystallization capacity necessary for mullite growth [86,112–115].

Table 3 summarises that when only clay-based materials are used in the so-called control ceramics, the technological variations observed are primarily controlled by dehydroxylation, restructuring of phyllosilicate groups, and the decarbonation of Ca- and Mg-bearing compounds.

© 2026 by the author(s). Distributed under a Creative Commons CC BY license.

Preprints.org (www.preprints.org) | NOT PEER-REVIEWED | Posted: 13 April 2026 doi:10.20944/preprints202604.0805.v1

With this mineralogical composition, no fully developed ceramic material is obtained at 800 °C; ceramic characteristics are only developed at higher temperatures, between 950 and 1100 °C.

Table 3. Mineralogy of the materials studied: raw materials, ceramics without additives (CC), and ceramics containing different proportions of tungsten-mining residues relative to clay (10, 25, and 50%), determined by X-ray diffraction (XRD).

	CLAY	SLUDGE	CC			MC10%			MC25%			MC50%		
			800	950	1100	800	950	1100	800	950	1100	800	950	1100
Chlorite	X													
Illite	X	X	X	X		X	X		X	X		X	X	
Paragonite	X													
Kaolinite	X	X												
Quartz	X	X	X	X	X	X	X	X	X	X	X	X	X	X
Calcite	X	X	X	X		X	X		X	X		X	X	
Microcline	X													
Dolomite	X	X												
Clinochlore		X												
Muscovite		X												
Magnetite		X												
Anorthite					X			X		X	X		X	X
Sanidine				X										
Diopside					X			X			X			X
Hematite			X	X	X	X	X	X	X	X	X	X	X	X
Orthoclase						X	X		X	X		X		
Mullite											X			X

The incorporation of tungsten-mining residues at 10, 25 and 50% enhances the reactivity of the mixtures, promoting the early formation of phases such as anorthite, which progressively replaces orthoclase. At 1100 °C, the resulting mineral assemblages converge toward a similar set of stable ceramic phases, namely quartz, anorthite, diopside, hematite and, occasionally, mullite [116].

3.3. Hydric Tests

The results of the water absorption and desorption tests performed on the bricks are presented in Figure 6, which shows the mass variations as a function of time. According to the absorption curves, all tested ceramic samples exhibit a free water absorption capacity ranging from 13.77% to 22.02%, representing differences of nearly 50% between the lowest and highest values. Overall, the general trend observed in all ceramic samples indicates that higher firing temperatures lead to slightly lower water absorption values [117–119].

The test lasted approximately 60 days, until the samples became fully saturated under atmospheric pressure. It should be noted that the highest absorption rate in all samples occurred within the first 10–20 minutes from the beginning of the test.

In the specific case of the control samples (CCL, CCM, and CCH), which do not incorporate tungsten-mining additives, it was observed that their water absorption increases with rising firing temperature, from 19.51% at 800 °C to 20.96% at 950 °C, and 21.53% at 1100 °C. Although these values are very similar across the three temperatures, they represent a slight overall increase of just over 9% between 800 °C and 1100 °C. This behaviour is likely associated with a somewhat greater formation of liquid phase in the more highly sintered ceramics (i.e., those fired at higher temperatures), which promotes the development of pores with larger diameters [120,121], particularly vacuolar-type pores, potentially originating from gas release at elevated thermal ranges [122–124].

Regarding the group of sustainable bricks, those incorporating 10% tungsten-mining waste (MC10L, MC10M, and MC10H) exhibit water absorption values of 20.45% at 800 °C, 22.00% at 950

© 2026 by the author(s). Distributed under a Creative Commons CC BY license.

Preprints.org (www.preprints.org) | NOT PEER-REVIEWED | Posted: 13 April 2026 doi:10.20944/preprints202604.0805.v1

°C, and 22.34% at 1100 °C. The maximum percentage differences are slightly above 8%, indicating relatively modest variations in absorption across the firing temperatures. This behaviour may be attributed to the tendency of fluxing additives to become increasingly reactive at elevated temperatures, which, at 1100 °C, may promote the development of additional meso and macroporosity [125–128].

The group of ceramics incorporating 25% tungsten-mining waste (MC25L, MC25M, and MC25H) exhibits maximum water absorption values of 18.39% at 800 °C, 19.15% at 950 °C, and 15.31% at 1100 °C. In this case, the values at 800 °C are lower than those of the previously discussed samples, increasing slightly at 950 °C, but decreasing at 1100 °C relative to both 800 °C and 950 °C. The difference between the minimum and maximum values represents a moderate variation, amounting to approximately 17% between 1100 °C and 800 °C, which is a considerable change that may be attributed to the higher flux content in the chemical composition of the mining sludges, particularly Fe, Na, and K (see Table 2) [129–133].

Finally, for the sustainable bricks incorporating 50% tungsten-mining waste at different firing temperatures (MC50L, MC50M, and MC50H), the water absorption values are 16.16% at 800 °C, 16.35% at 950 °C, and 13.73% at 1100 °C, with a difference of nearly 4% between the maximum and minimum values. These results indicate, first, that at higher temperatures (1100 °C) the extent of liquid-phase formation in the sustainable bricks becomes significant, leading to a microstructure dominated by micropores [134,135]. As a consequence, the amount of absorbed water is much lower than that observed in the rest of the ceramic production. Second, these findings support the conclusion that increasing the proportion of tungsten-mining waste in the bricks reduces their water uptake, thereby enhancing their potential long-term durability [136,137].

The desorption index values of the bricks range from 0.69% to 0.81%, corresponding to the sustainable bricks MC50M and MC10H, respectively. In all cases, the bricks studied exhibit medium-to-low drying indices, as complete drying generally occurs within approximately five days.

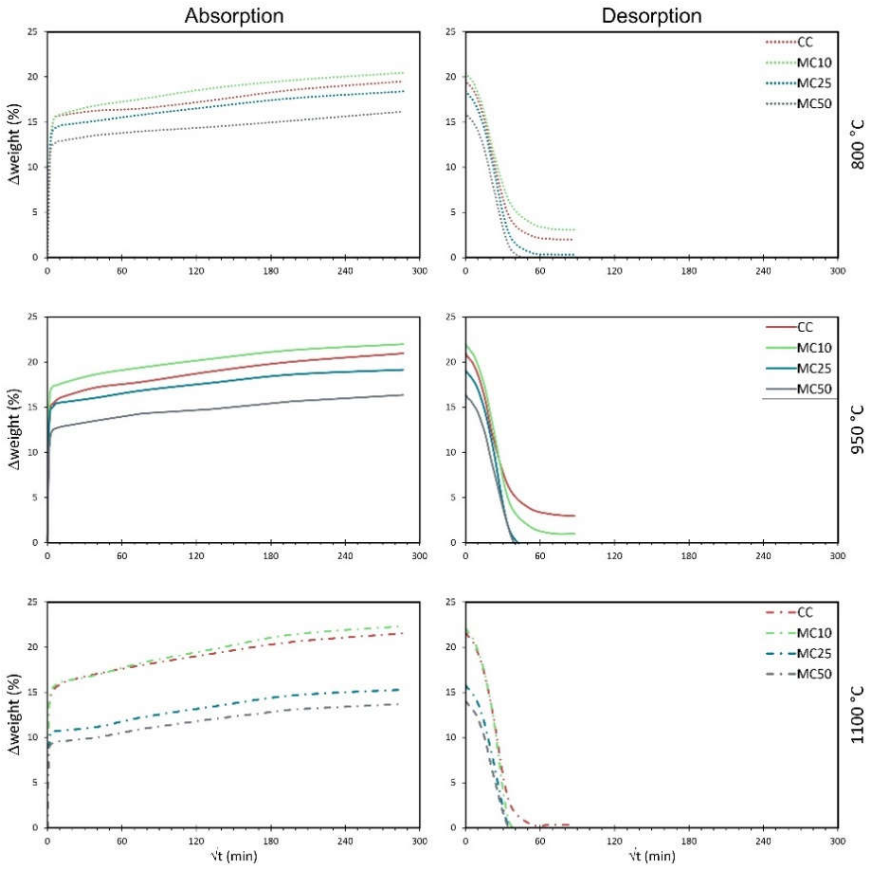

© 2026 by the author(s). Distributed under a Creative Commons CC BY license.

Preprints.org (www.preprints.org) | NOT PEER-REVIEWED | Posted: 13 April 2026 doi:10.20944/preprints202604.0805.v1

Figure 6. Absorption and desorption curves of the bricks without tungsten-mining additives (CC, fired at 800, 950, and 1100 °C), as well as the sustainable bricks incorporating tungsten-mining waste at the different firing temperatures (MC10%, MC25%, and MC50, fired at 800, 950, and 1100 °C).

3.4. Mercury Intrusion Porosimetry (MIP)

The results of the mercury intrusion porosimetry analysis are summarized in Table 4. The total porosity values of all sustainable brick samples, including ceramic materials without additives and those incorporating tungsten-mining by-products, exhibit substantial variability as a function of the formulation, the additive proportions, and the firing temperature [138,139]. These results reveal a consistent trend toward lower total porosity with increasing firing temperature, which is partially aligned with the proportion of mining-derived additive incorporated into each specimen [140–142].

These maximum and minimum values, 38.60% for CCL and 24.80% for MC50, represent a difference of nearly 56% between both extremes. This indicates that substantial changes occur between the samples fired at low and high temperatures (from 800 °C to 1100 °C). In general, the incorporation of tungsten-mining residual sludges tends to reduce total porosity, an effect that is reinforced at higher firing temperatures and is particularly evident at a 50% additive proportion at 1100 °C [143,144].

Table 4. Mercury intrusion porosimetry data for bricks without additives and sustainable bricks incorporating tungsten-mining waste. Po corresponds to the percentage of mercury-accessible pores relative to the total sample volume, indicating the pore-size categories of mesopores, macropores, and air voids/cracks.

		Pores typology μm (%)		
	Po (%)	Mesopores (0.002 – 0.05)	Macropores (0.05 – 10)	Air voids/cracks (> 10)
CCL	38,60	16,03	81,32	2,65
CCM	37,61	8,51	89,33	2,16
CCH	37,40	56,61	40,35	3,03
MC10L	38,40	16,15	78,05	5,80
MC10M	35,80	4,64	92,97	2,39
MC10H	34,90	3,49	92,54	3,97
MC25L	38,57	20,22	76,16	3,62
MC25M	34,92	6,12	89,34	4,54
MC25H	33,81	4,86	90,57	4,57
MC50L	37,59	8,26	86,38	5,36
MC50M	31,77	6,69	89,37	3,94
MC50H	24,80	6,57	85,70	7,73

The pore-size distribution is predominantly unimodal, with average diameters ranging from 0.05 to 10 μm. However, notable variations in the proportions of mesopores, macropores, and air voids/cracks are observed depending on the sample type and firing temperature (Figure 7). Quantitatively, the highest proportion of pore sizes across all samples corresponds to macropores, with maximum and minimum values ranging from 92.97% to 40.35%, representing differences greater than 57%. The mesopore fraction is highly heterogeneous (56.61% to 3.49%), whereas, interestingly, the air-void/crack category exhibits relatively consistent values (7.73% to 2.16%).

A particular case is represented by the so-called control ceramics (CC). It can be inferred that increasing the firing temperature leads to a marked reduction in the macropore percentage, decreasing from 81% in CCL to 40% in CCH. This behavior suggests a densification effect induced solely by the thermal treatment, without the contribution of additional fluxing agents such as those present in the tungsten-mining sludges.

In contrast, the sustainable ceramic bricks incorporating tungsten-mining sludges exhibit a relatively opposite trend, as increasing the firing temperature promotes the formation of macropores,

© 2026 by the author(s). Distributed under a Creative Commons CC BY license.

Preprints.org (www.preprints.org) | NOT PEER-REVIEWED | Posted: 13 April 2026 doi:10.20944/preprints202604.0805.v1

reaching a maximum value of 92.97% in MC10M. This behavior is undoubtedly attributable to the presence of fluxing agents in the tungsten-mining waste sludges, as well as to their inherent compositional heterogeneity (see Table 2), and to a vacuole-formation process within the vitreous phase, directly associated with gas release caused by the excess of fluxing components [145,146]. Finally, although the air-void/crack fraction is minor in all bricks, its presence is variable and may be conditioned by internal contraction stresses generated during the high-temperature firing of the liquid phase. However, this interpretation is debatable, given the high residual content (50%), which not only acts as a fluxing component but also functions as a temper and as a structural framework former [147–149].

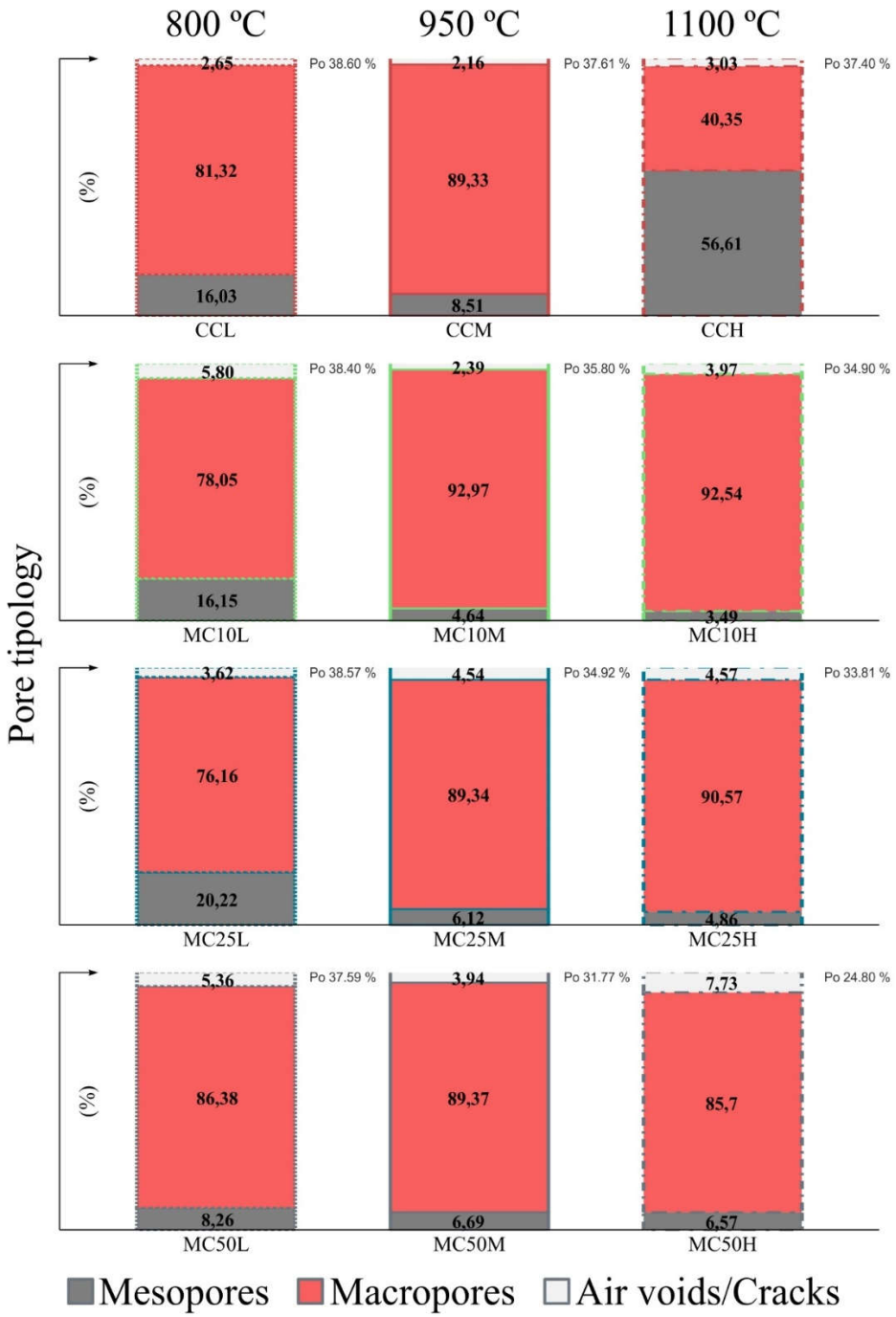

Figure 7. Pore typology of bricks without additives and sustainable bricks incorporating tungsten-mining residues fired at 800, 950, and 1100 °C. Macropores predominate in all samples compared with mesopores and air voids/cracks. Po indicates the total porosity of each sample relative to its volume.

© 2026 by the author(s). Distributed under a Creative Commons CC BY license.

Preprints.org (www.preprints.org) | NOT PEER-REVIEWED | Posted: 13 April 2026 doi:10.20944/preprints202604.0805.v1

3.5. Ultrasonic Pulse Velocity

The ultrasonic pulse velocity (Vp) values obtained for the different samples under study, both without additives and with tungsten mining additives, together with the required unfired reference samples used to assess the potential influence of the additive on the clay-based material, as well as the firing temperature, are presented in Table 5. In general, the unfired samples exhibit low ultrasonic transmission values, with a slight increase depending on the absence or presence of sludge at 10, 25, and 50%. The values range from 1492 m/s to 1680 m/s, representing small differences of slightly more than 10%. This behaviour is consistent with the expected increase in mechanical strength as a function of the amount of sludge incorporated [150–152].

Table 5. Mean values and standard deviations of the ultrasonic pulse velocity test (m/s) for the samples analysed, including NF (unfired), CC (ceramic material without tungsten-mining additive), MC10, MC25, and MC50 (ceramics incorporating 10, 25, and 50% additive), and L, M, and H (firing temperatures of 800, 950, and 1100 °C).

	Sample	$\bar{x}$	σ	Sample	$\bar{x}$	σ	Sample	$\bar{x}$	σ	Sample	$\bar{x}$	σ
NF	CC	1492	53	MC10	1515	58	MC25	1549	48	MC50	1680	33
800	CCL	2019	52	MC10L	1490	54	MC25L	1991	47	MC50L	2010	52
950	CCM	2283	66	MC10M	2200	82	MC25M	2256	35	MC50M	2389	37
1100	CCH	2592	52	MC10H	2600	49	MC25H	2840	57	MC50H	2963	41

With respect to the fired samples without additives, referred to as the control samples (CC at 800, 950, and 1100 °C), consistent increases in ultrasonic velocity are observed, ranging from 2019 to 2592 m/s. This represents nearly a 30% improvement in the compaction of the samples made entirely of clay-based material. This behaviour is consistent with established ceramic science, as temperatures close to 800 °C promote dehydroxylation and particle packing, followed by the development of phases exhibiting optimal levels of vitrification between 950 and 1100 °C, where the formation and growth of an amorphous liquid phase occur. These processes enhance the sintering of the constituent materials and promote the closure of a significant proportion of pores, although small shrinkage-induced fissures may appear in the ceramic matrix [153,154].

In the remaining sustainable ceramic bricks incorporating 10, 25, and 50% sludge, there is a general trend of increasing ultrasonic velocity as the proportion of tungsten-mining additive increases (10, 25, and 50%). As expected, ultrasonic pulse velocity also increases with the rise in firing temperature from 800 to 1100 °C. At 800 °C, the values exhibit an increase of approximately 35% as the additive content rises from 10% to 50%, although it is noteworthy that the 10% mixture shows very low values, around 1490 m/s, which are similar to those of the unfired samples. This is attributed to the mere dehydroxylation of the clays and the absence of vitrification–sintering at this temperature. At 950 °C, the increases do not reach 10% when comparing ceramics with the lowest additive content to those containing 50%. In particular, the ultrasonic velocity of the 10% sludge mixture at this temperature is nearly 4% lower than that of the sample without mining additives, likely due to the limited action of the fluxing elements (K, Na, Ca) at this temperature, combined with the low additive proportion. At 1100 °C, the sustainable bricks show increases of approximately 14%, with velocities ranging from about 2600 m/s (10% sludge) to nearly 3000 m/s (50% sludge). This indicates that increasing the additive content in the mixtures promotes effective ceramic densification and the formation of an amorphous glassy phase at higher sludge incorporations [155–157].

Figure 8 clearly illustrates that higher contents of mining residue and higher firing temperatures lead to improved compaction and enhanced mechanical reinforcement in the sustainable bricks, as well as to superior ceramic properties. These improvements are attributed to the action of the mining residue, which is rich in SiO_2–Al_2O_3 and contributes to the formation of solid structures that act as genuine load-bearing networks, together with the presence of crucial fluxing elements and minerals found in the tungsten-mining residues used in this study (Ca, Na, K, Sn, Ba). This enhancement

© 2026 by the author(s). Distributed under a Creative Commons CC BY license.

Preprints.org (www.preprints.org) | NOT PEER-REVIEWED | Posted: 13 April 2026 doi:10.20944/preprints202604.0805.v1

undoubtedly represents a significant advantage in terms of recyclability, sustainability, and the reuse of waste materials [158].

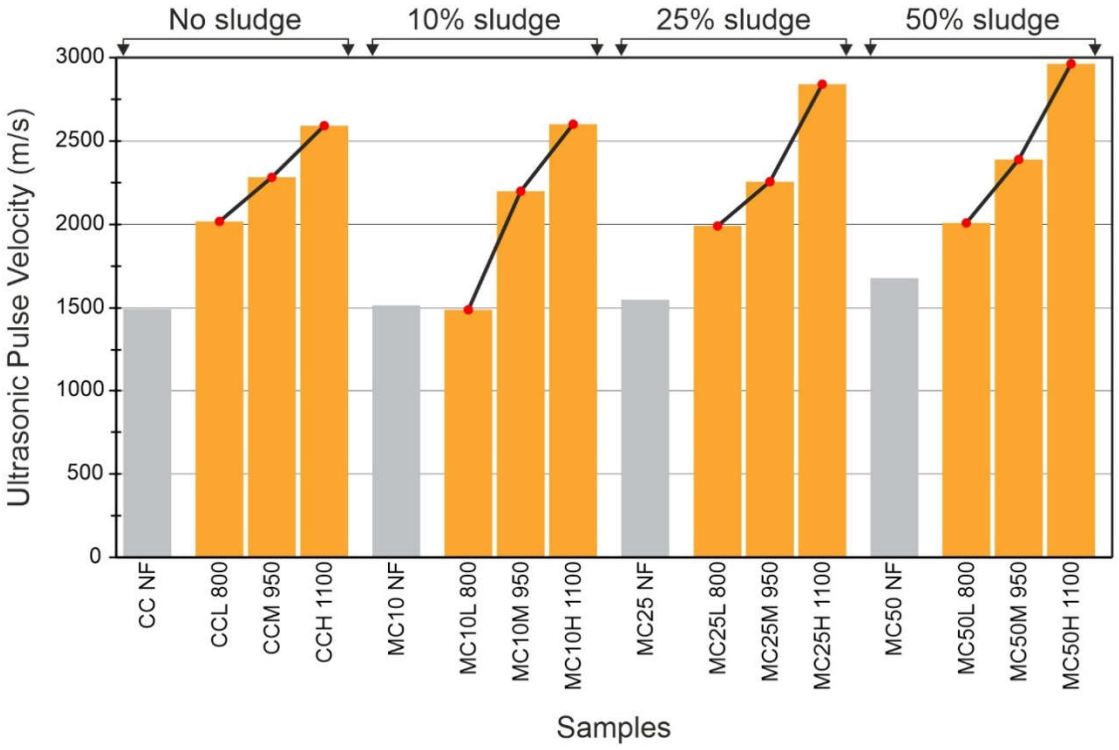

Figure 8. Variability of ultrasonic pulse velocity (m/s) for all samples studied with different proportions of tungsten-mining residue. The unfired samples (NF) are shown in grey, while the remaining samples correspond to sustainable bricks without tungsten-mining additives and to those with different additive proportions. CCL, CCM, and CCH represent the control ceramics without additives fired at 800, 950, and 1100 °C, respectively. MC10-L, MC10-M, and MC10-H correspond to sustainable bricks incorporating 10% additive fired at 800, 950, and 1100 °C, respectively; MC25-L, MC25-M, and MC25-H represent bricks incorporating 25% additive fired at 800, 950, and 1100 °C; and MC50-L, MC50-M, and MC50-H correspond to bricks incorporating 50% additive fired at the same firing temperatures.

3.6. Compressive Strength

The compressive failure strength values for the different ceramic bricks, including the control samples without tungsten mining additives and those incorporating 10%, 25%, and 50% additives, are presented in Table 6 and illustrated in Figure 9. The results exhibit a range between 11.97 and 26.19 MPa, with clear variations as a function of composition and firing temperature across the different types of sustainable bricks.

Table 6. Mean values and standard deviations of the modulus of rupture for the bricks without mining additives (CC), and for the sustainable ceramic bricks incorporating tungsten mining additives at different proportions (10%, 25%, and 50%), with respect to the studied firing temperatures. Mean values and standard deviations are expressed in MPa.

	Sample	$\bar{x}$	σ	Sample	$\bar{x}$	σ	Sample	$\bar{x}$	σ	Sample	$\bar{x}$	σ
800	CCL	11,97	0,1	MC10L	14,23	3,2	MC25L	16,95	3,2	MC50L	16,79	0,9
950	CCM	20,25	4,9	MC10M	17,55	2,4	MC25M	17,70	4,6	MC50M	18,26	1,3
1100	CCH	13,32	0,2	MC10H	20,42	2,5	MC25H	26,19	6,6	MC50H	23,88	3,2

In the control samples (CC), the strength increases markedly between 800 and 950 °C, rising from 11.97 MPa (CCL) to 20.25 MPa (CCM), which represents almost a 70% improvement in

© 2026 by the author(s). Distributed under a Creative Commons CC BY license.

Preprints.org (www.preprints.org) | NOT PEER-REVIEWED | Posted: 13 April 2026 doi:10.20944/preprints202604.0805.v1

mechanical strength. This behaviour is coherent with the expected sintering processes occurring in this temperature range for bricks without additives, where reductions in open porosity and particle rearrangement take place, accompanied by interparticle bonding and the formation of sintering necks. However, after firing at 1100 °C, the strength decreases to 13.32 MPa in sample CCH, representing a reduction of more than 50% in mechanical strength. This decrease may be associated with structural weakening linked to decarbonation processes, which involve the release of significant amounts of CO_2 that can lead to the formation of secondary pores or microcracking. Likewise, the heating rate used may influence the sintering process by promoting too rapid a sintering stage, with accelerated formation of the liquid phase and the development of closed porosity trapped within the glassy matrix. In such conditions, microbubbles may form, ultimately leading to a loss in uniaxial compressive strength [159–162].

In the mixtures containing 10% sludge (MC10), the strength values increase progressively with temperature, from 14.23 MPa at 800 °C to 20.42 MPa at 1100 °C in sample MC10H, representing an improvement of nearly 45% in mechanical strength. This behaviour confirms a progressive densification effect influenced by the presence of waste in small proportions, together with the fluxing action of Na, K, and Ca, particularly at 1100 °C. The enhancement in strength observed in these sustainable 10% bricks can be attributed to several factors. First, the very fine particles present in the mining waste act as sintering nuclei due to their higher specific surface area, which also promotes solid-state diffusion because of the chemical composition of the residue. Likewise, the consolidation of pore necks associated with the sintering process is expected as the temperature increases, generating a reduction in open porosity and improving the internal cohesion of the ceramic matrix. Additionally, the fluxing components present in tungsten mining waste, which despite their heterogeneous nature contribute to lowering the vitrification temperature, favour densification at intermediate temperatures (around 950 °C) and promote the formation of a liquid phase capable of filling pores [163–167].

The ceramics containing 25% additive (MC25) exhibit a similar trend, with strength increases of approximately 55% as a function of temperature. Notably, the value of 26.19 MPa obtained for the sustainable brick MC25H at 1100 °C represents the highest strength among all typologies, indicating that this addition level (25%) optimizes matrix consolidation and enhances mechanical performance. This superior behaviour can be attributed to several factors, including improved densification during sintering due to enhanced particle coalescence, the development of more consolidated sintering necks, reduction in open and interconnected porosity, and a decrease in the viscosity of the liquid phase, which limits the formation of microbubbles. In addition, an improved balance between crystalline and glassy phases is achieved, with a sufficient proportion of the latter to promote adequate cohesion, prevent deformation, microbubble formation, or microcracking, minimize internal heterogeneities and defects, and ensure optimal stabilization of volumetric shrinkage in this typology of sustainable ceramic bricks (MC25H) [168–171].

Finally, the mixtures containing 50% sludge (MC50) also exhibit increasing strength with temperature, reaching a minimum–maximum range from 16.79 MPa at 800 °C to 23.88 MPa at 1100 °C in sample MC50H, which represents an approximate increase of 42% between both temperatures. However, this maximum value for the combination of 50% tungsten mining waste and the highest firing temperature of 1100 °C (23.88 MPa) remains lower in uniaxial compressive strength compared with the sample containing 25% additive fired at 1100 °C. On the other hand, this group of bricks incorporating 50% mining waste clearly outperforms the control samples (without tungsten mining residue), confirming the potential of the waste to enhance the mechanical performance of sustainable ceramic bricks. This slightly anomalous behaviour may be explained first by a certain restriction in the sintering process due to the excess of fluxing components (Na, Ca, and K), which increases the amount of liquid phase but can also lead to an imbalance between the glassy and crystalline phases. Similarly, a rise in closed porosity may occur, with microbubbles formed by trapped gases (CO_2, SO_2 or small amounts of water vapour), which in some cases become a critical factor in structural

© 2026 by the author(s). Distributed under a Creative Commons CC BY license.

Preprints.org (www.preprints.org) | NOT PEER-REVIEWED | Posted: 13 April 2026 doi:10.20944/preprints202604.0805.v1

ceramics. Finally, it is plausible to infer that an excessively glassy matrix may reduce the toughness of the ceramic material, increasing its brittleness [172–175].

In any case, as part of the discussion, all the sustainable ceramic brick samples exceed the minimum mechanical strength threshold, which is 9.81 MPa for solid and vertically perforated bricks and 4.90 MPa for structural hollow bricks, according to the applicable standards [176,177].

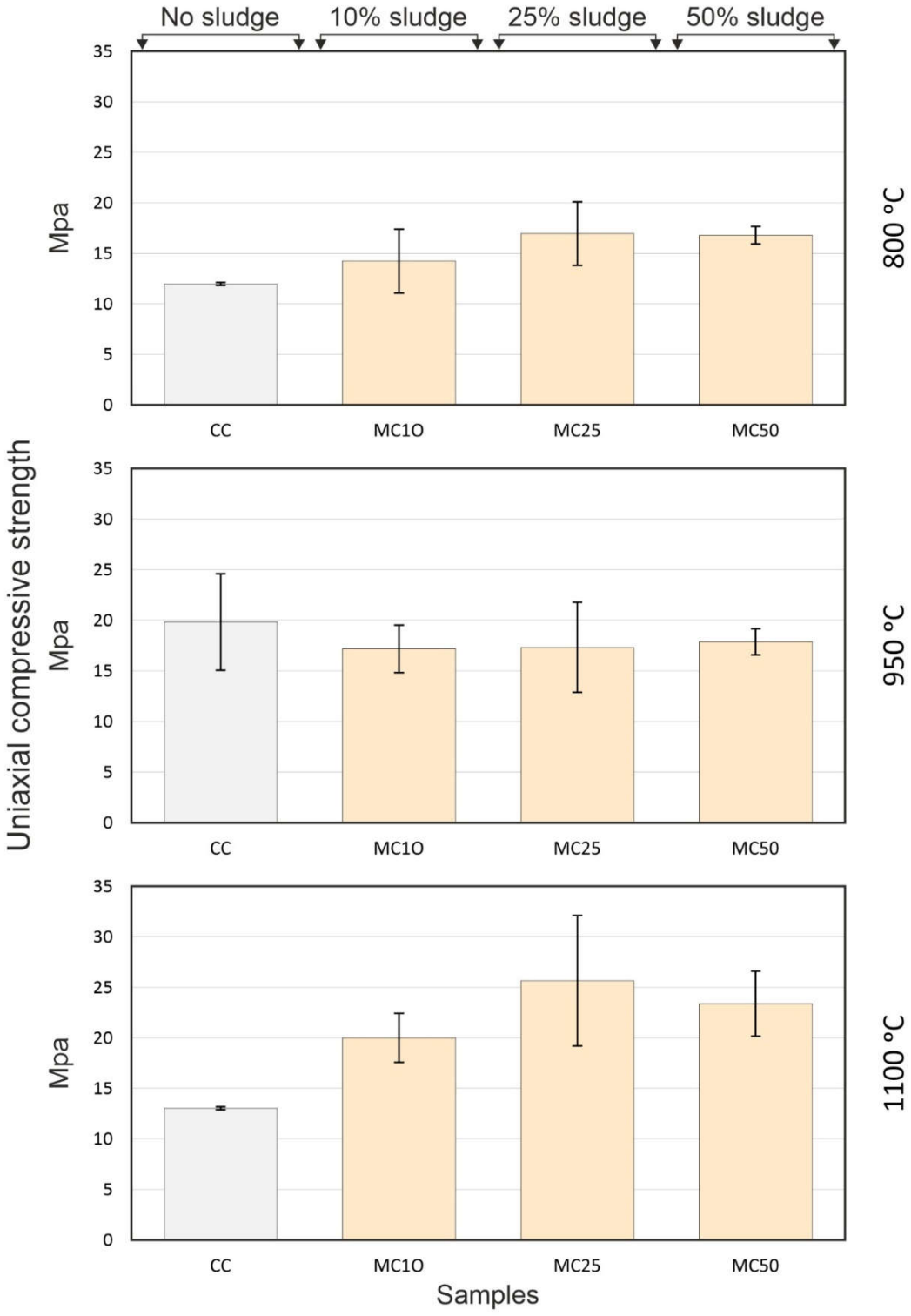

Figure 9. Representation of uniaxial compressive strength values (MPa) for the ceramic samples without tungsten mining waste (CC samples) and for the sustainable bricks incorporating mining waste at proportions of 10%, 25%, and 50% (MC samples), as a function of the different firing temperatures (800, 950, and 1100 °C).

© 2026 by the author(s). Distributed under a Creative Commons CC BY license.

Preprints.org (www.preprints.org) | NOT PEER-REVIEWED | Posted: 13 April 2026 doi:10.20944/preprints202604.0805.v1

3.7. Environmental Scanning Electron Microscope (ESEM)

The ESEM analysis of the ceramic products revealed a heterogeneous texture and elemental composition consistent with the raw materials used, residual natural clays and tungsten mining tailings, combined in the known proportions of 10, 25, and 50%. This significant heterogeneity is characteristic of the production of sustainable bricks and ceramic materials (Figure 10).

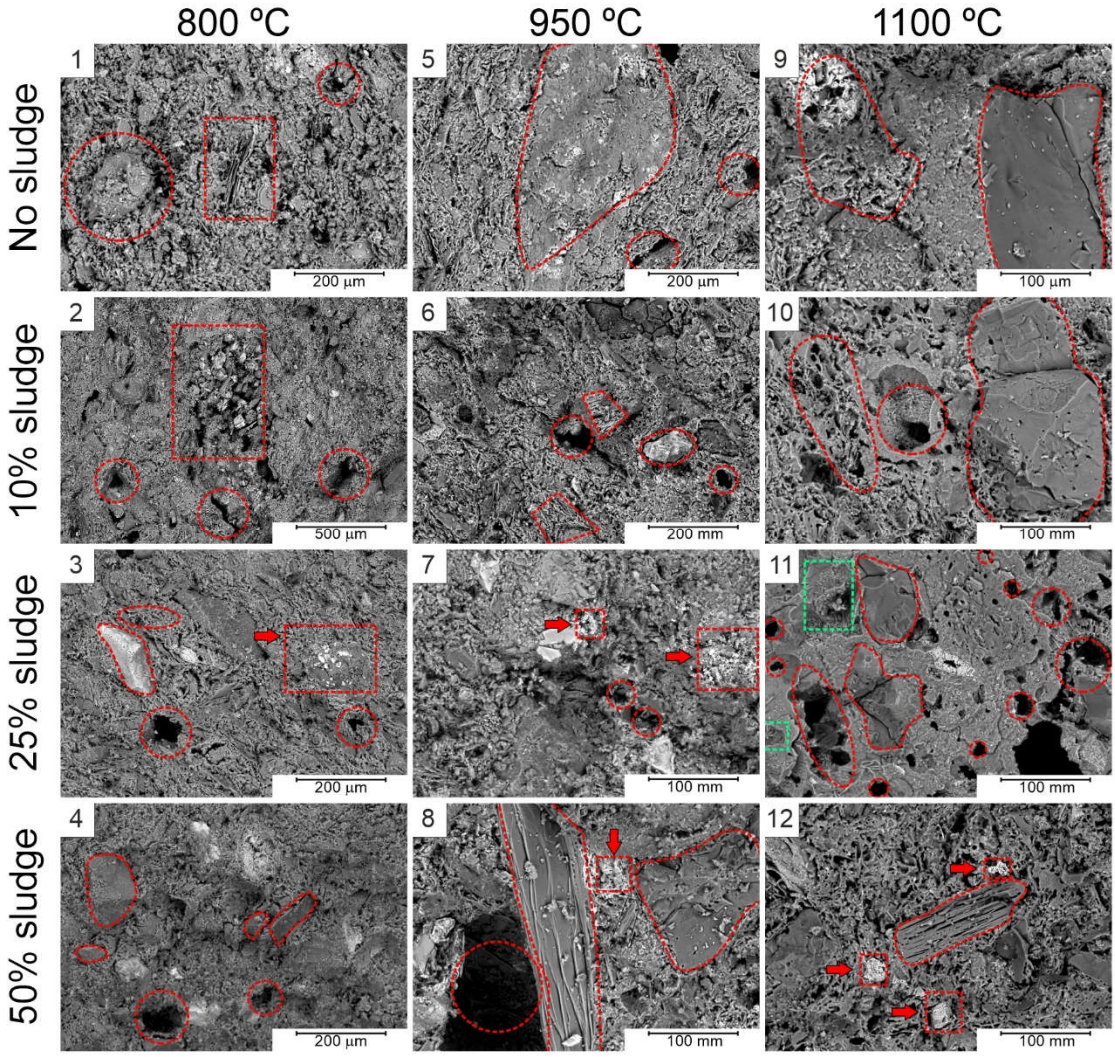

Figure 10. Scanning electron microscopy (SEM) images of the ceramic samples studied at 800, 950, and 1100 °C, without additives (images 1, 5, and 9) and of sustainable ceramic bricks with 10, 25, and 50% additive content (images 2, 3, 4, 6, 7, 8, 10, 11, and 12). The red rectangles with dashed outlines highlight features of the ceramic materials such as grains, pores, or vitrified areas, the red rectangles with dashed outlines and an arrow indicate the presence of unmelted metals derived from mining residues, and the green rectangles identify mullite recrystallizations.

In general, the ceramic matrix is composed mainly of phyllosilicates, which constitute the dominant materials and are particularly rich in calcium (>10%), potassium, sodium, and iron, as confirmed by the XRF and XRD results. These analyses also reveal the presence of other minerals such as muscovite, a potassium and aluminum silicate characterized by its platy habit and fluxing capacity at specific temperatures, as well as visually identifiable kaolinite and illite aggregates. Quartz crystals are also noteworthy due to their size and abundance, being dominant in the mining residues owing to the veins from which tungsten is extracted, and therefore prevailing in the starting sludge materials. Additionally, calcium and magnesium carbonates, calcium sulfates, and iron recrystallizations have been identified. Finally, in the ceramic pastes containing mining sludge,

© 2026 by the author(s). Distributed under a Creative Commons CC BY license.

Preprints.org (www.preprints.org) | NOT PEER-REVIEWED | Posted: 13 April 2026 doi:10.20944/preprints202604.0805.v1

arsenic has been detected along with other metallic elements such as zinc, titanium, barium, tin, and tungsten [178]. In the aforementioned Figure 10, backscattered electron microscopy images of the studied samples are shown, where textural features and various mineral morphologies are identified.

The samples fired at 800 °C exhibit an irregular surface. The dehydrated clay lamellae appear arranged in compact aggregations, with pores of varied morphology and sizes ranging from 10 to 50 μm. In general, both the ceramic materials without residue and those containing tungsten mining residues (sustainable bricks with 10, 25, and 50% additions) display the characteristic texture of underfired ceramics, that is, poor densification and an absence of vitrification, where only the hydroxyl groups have been removed from the clay minerals and part of the CO_2 present in carbonates has volatilized, together with the combustion of organic matter [179]. Mineral grains that behave as temper within this thermal range appear well defined and without signs of thermal alteration. Clusters of unmelted metallic fragments are also observed, highlighted with red dashed rectangles accompanied by an arrow (Figure 10, images 1 to 4).

In the 950 °C range, particle contacts become more evident and a more densified matrix with signs of sintering can be distinguished (Figure 10, images 5 to 8). Dehydroxylation is complete in the clay materials and the pores continue to exhibit irregular morphology, with heterogeneous sizes ranging from 10 to 200 μm. Some mineral grains, such as carbonates and quartz, show slight thermal alterations and small shrinkage cracks. In the mixtures containing 25% sludge, the quartz grains are clearly identifiable and iron recrystallizations, together with associated metals such as zinc, are prominent, marked with red dashed lines and an arrow. Moreover, mica fragments are clearly visible, although they show evidence of partial melting (Figure 10, image 8). Overall, this group of ceramics without additives (Figure 10, image 5) as well as those with 10, 25, and 50% additions (Figure 10, images 6 to 8) display partially densified matrices with contact pores originating from the tungsten mining additives and the clays, together with clusters of partially vitrified materials [180].

At 1100 °C, the compactness and vitrification of the matrix are evident in all sample types, although they are more pronounced in the mixtures containing tungsten mining sludge than in the ceramics without additives, due to the lower flux content in the latter mixtures (Figure 10, images 9 to 12). Visually, all matrices within this thermal range show very good vitrification, and the densification of the sustainable bricks depends on the variability in the content of mining additives. The ceramics with 10, 25, and 50% mining residue exhibit a typical texture of semi complete vitrification, and the pores, which are irregular in size, adopt circular shapes along with the characteristic presence of vacuoles or bubbles formed by gas release and the coalescence of adjacent pores. Some phyllosilicates retain their laminar habit, although large vitrified areas are present between the particles [181]. The quartz grains display substantial thermal alteration with intergranular fractures, and remnants of unmelted metals derived from mining residues are also observed (Figure 10, images 9 to 12). The optimal mixture based on electron microscopy criteria is the one combined with 25% mining residue at 1100 °C, where mullite recrystallizations can be observed within green dashed rectangles (Figure 10, image 11).

Figure 11 presents the elemental maps and their associations for the sustainable brick containing 25% tungsten mining residues fired at 1100 °C (Figure 11, images 1 to 8). The distributions of silica alumina phases that form the ceramic matrix can be observed, together with several of the main fluxing elements derived from the clay and from the mining residues, such as potassium and calcium. In addition, nodules of hematite recrystallizations are visible (Figure 11, image 6), along with vitrified matrix nodules enriched in zinc, which has also acted as a fluxing agent (Figure 11, image 7).

© 2026 by the author(s). Distributed under a Creative Commons CC BY license.

Preprints.org (www.preprints.org) | NOT PEER-REVIEWED | Posted: 13 April 2026 doi:10.20944/preprints202604.0805.v1

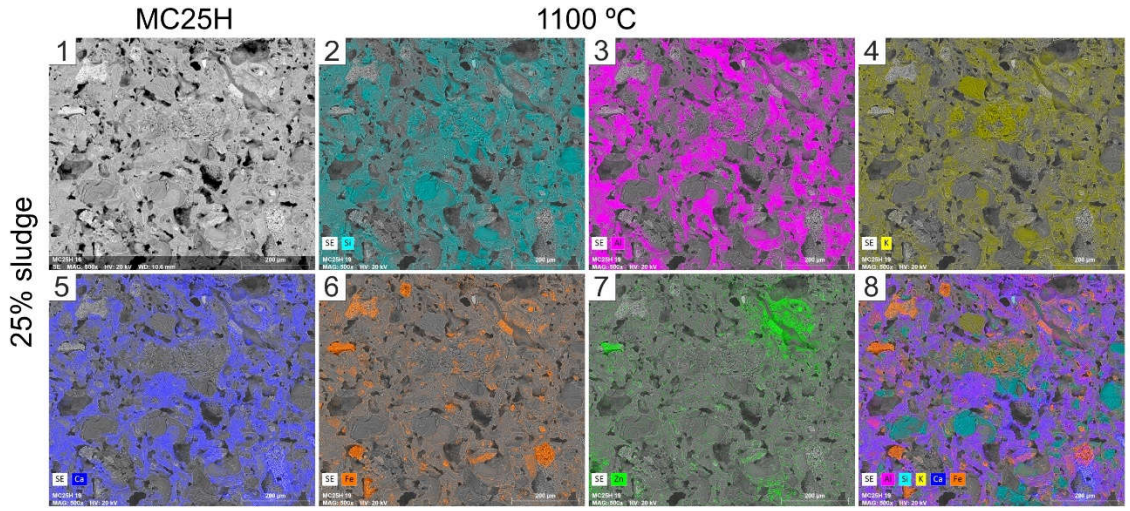

Figure 11. SEM image of the sustainable brick sample containing 25% mining residue fired at 1100 °C (image 1), and elemental distribution images of the brick. Image 2 shows Si, image 3 shows Al, image 4 shows K, image 5 shows Ca, image 6 shows Fe, image 7 shows Zn, and image 8 presents the combined surface distribution of Si, Al, K, and Ca. The scale for all images corresponds to 200 μm.

3.8. Leaching Test

Table 7 reports the concentration of chemical elements leached from the corresponding eluates of the mining sludge samples and the ceramic samples of sustainable bricks, expressed in parts per billion, and Figure 12 illustrates the relative retention of these chemical elements.

Table 7. Concentration, in parts per billion (ppb), of the chemical elements determined in the eluates obtained from the leaching test by ICP–MS, as well as their retention within the ceramic matrix as a function of the mixture composition and the temperature assessed. The elements are listed according to their toxicity level for human health, following [182]. The letter L denotes samples fired at 800 °C, and H those tested at 1100 °C.

	Sludges	MC10L	MC25L	MC50L	MC10H	MC25H	MC50H
As	9769,30	97,60	276,80	1481,20	88,70	202,80	826,80
Cd	77,10	0,04	0,00	1,40	1,10	0,90	4,10
Pb	1,20	0,00	0,20	0,20	0,70	0,70	0,70
Ni	367,60	0,80	0,90	1,20	0,80	2,70	5,80
Co	109,90	0,00	0,07	0,40	0,20	0,06	0,70
Cu	68,53	10,40	0,50	3,00	10,00	10,40	23,60
W	12571,30	69,10	593,00	778,10	81,90	88,20	674,00
Mn	2168,93	0,03	0,30	0,10	1,30	2,10	2,70
Fe	4186,70	6,40	11,10	6,50	11,60	8,50	8,10
Zn	13907,80	0,00	0,00	0,00	16,40	3,30	43,20

According to previous studies [183–185], the concentrations of the most prevalent and environmentally hazardous elements present in the sludge samples were evaluated. These elements were ranked from highest to lowest toxicity to human health and the environment, following the classifications reported by [186–189], namely: As, Cd, Pb, Ni, Cu, Co, Mn, Zn, Fe, and W.

In general, all ceramic materials inhibit the leaching capacity inherent to mining sludges, as all sustainable bricks, both those sintered at very low temperatures (800 °C) and those produced at optimal sintering temperatures (1100 °C), exhibit a strong retention of toxic elements. This represents a key characteristic of these sustainable bricks manufactured from tungsten mining tailings.

It is evident that the sustainable bricks developed for this study retain toxic elements with sufficient effectiveness to safeguard both the environment and human health, and they complete the

© 2026 by the author(s). Distributed under a Creative Commons CC BY license.

Preprints.org (www.preprints.org) | NOT PEER-REVIEWED | Posted: 13 April 2026 doi:10.20944/preprints202604.0805.v1

sustainable-design cycle by enabling the reuse of raw materials, in this case tungsten mining sludges, which would otherwise be difficult to incorporate into conventional recycling streams

The higher amount of leachates observed in the sludges is explained by their lack of encapsulation within a ceramic matrix or any other encapsulating binder, as well as by the fine particle size and the high specific surface area characteristic of these sludges [183,190], factors that confer to these waste materials a high chemical reactivity when exposed to weathering and, in particular, to leaching processes.

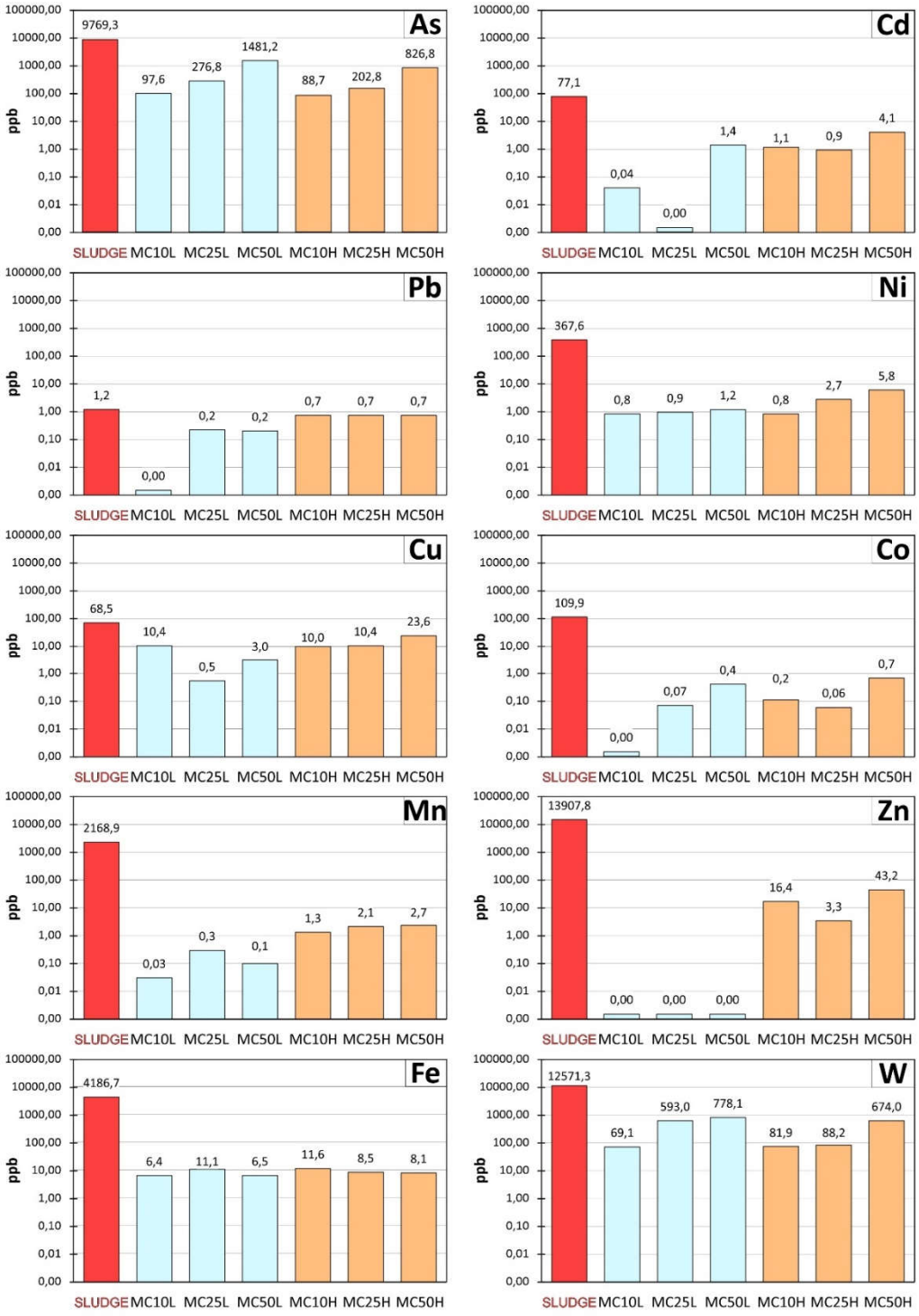

Figure 12. Variability in the reduction of leaching of contaminant elements in ceramic samples of sustainable bricks incorporating tungsten mining tailings at 10, 25, and 50 percent, fired at two temperatures (800 and 1100

© 2026 by the author(s). Distributed under a Creative Commons CC BY license.

Preprints.org (www.preprints.org) | NOT PEER-REVIEWED | Posted: 13 April 2026 doi:10.20944/preprints202604.0805.v1

°C). The reduction in leaching retained by the ceramic matrix, relative to the tungsten mining residues, is expressed in ppb. The graphical order is based on toxicity to human health according to [182].

In detail, for Mn, there is substantial encapsulation within the ceramic matrix of the sustainable bricks, with leachate concentrations approaching zero in the samples fired at 800 °C across all formulated proportions (10, 25, and 50 percent), as well as drastic inhibitions in the bricks fired at 1100 °C, which achieve even higher encapsulation efficiencies, specifically nearly five orders of magnitude. Similarly, Zn exhibits zero leachate values in the samples fired at 800 °C at all concentrations, with inhibitions exceeding 3.6 orders of magnitude, corresponding to more than a 4000-fold reduction of the metallic element. In the case of Cd, which is particularly important due to its toxicity [191], variations in leaching show differences of nearly 3.3 orders of magnitude, with inhibitions greater than 1900-fold. Co exhibits variations that in some cases reach complete inhibition, with reductions exceeding 3.25 orders of magnitude and inhibitions greater than 1800-fold. Fe shows variability above 2.8 orders of magnitude, with inhibitions exceeding 650-fold. Ni displays variations of 2.66 orders of magnitude, W of 2.26, Cu of 2.14, As of 2.04, and Pb of 0.78 orders of magnitude.

A greater degree of leaching is observed for tungsten and arsenic, which may indicate that thermally induced mineral decomposition can lead to the formation of mineral phases with heterogeneous stability, making certain elements more prone to leaching. The results of the test suggest that As, like W, can be more readily mobilized and extracted by the leaching agent in some of the designed mixtures after thermal treatments at 800 and 1100 °C. This behavior is consistent with the pH values, which is of relative significance (Figure 13), since an increase in pH toward more basic eluates compared with those measured in the sludges may be associated with this enhanced mobility.

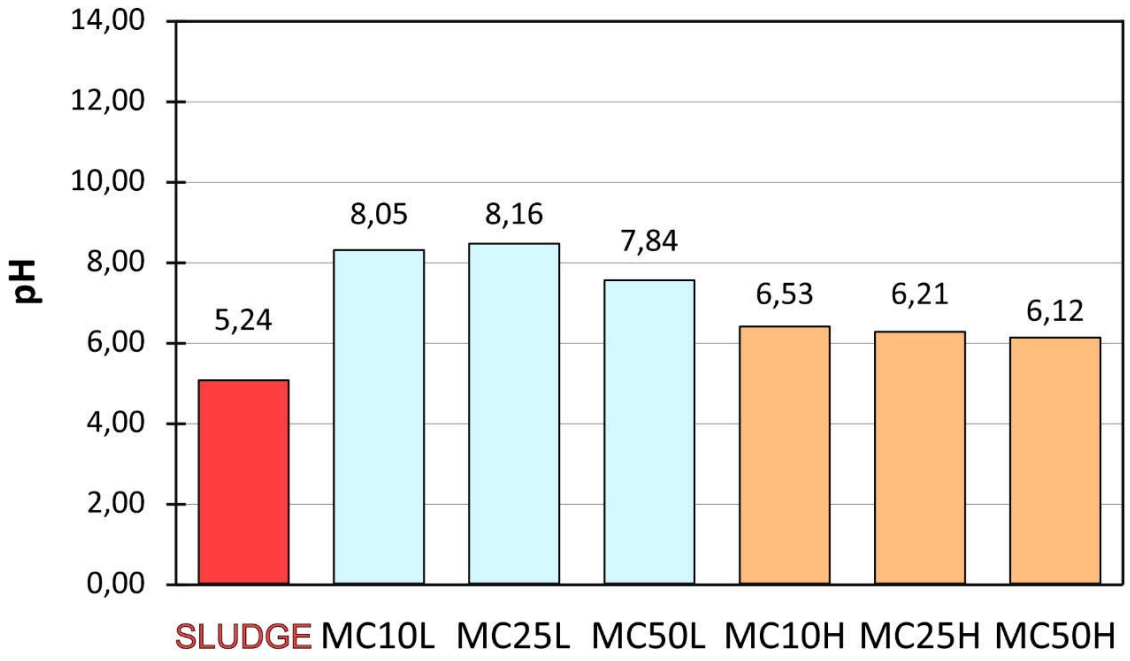

Figure 13. Variability in pH during the leaching test in sludges and in sustainable brick mixtures containing 10, 25, and 50% additives, fired at 800 and 1100 °C.

Similarly, according to [192], the mobility of tungsten in water with neutral pH is classified as intermediate to low. However, the analysis of the eluates indicates a release of W in all ceramic samples, despite the fact that the measured pH values are not excessively acidic or basic, but fall within the range of 6 to 8. In the case of W, this behavior could be related to the thermal treatments applied during firing, which may enhance the mobility of this metal. In this regard, the samples fired at 1100 °C exhibit tungsten concentrations that are very similar to those of the same mixtures fired at 800 °C [184,190,193].

© 2026 by the author(s). Distributed under a Creative Commons CC BY license.

Preprints.org (www.preprints.org) | NOT PEER-REVIEWED | Posted: 13 April 2026 doi:10.20944/preprints202604.0805.v1

3.9. Color

Table 8 presents the chromatic values of the raw materials and of the resulting ceramic products, including both the samples without tungsten mining residues and the sustainable bricks incorporating 10, 25, and 50% tungsten mining additives, fired at 800, 950, and 1100 °C. Figure 14 displays the corresponding chromatic coordinates (a* and b*) in the chromaticity plane and along the lightness axis (L*), whereas Figure 15 shows the total color differences (ΔE) of the ceramic samples of sustainable bricks containing tungsten mining residues, relative to the control ceramics that do not include mining sludge.

All the analyzed materials, including the raw materials and the manufactured ceramic products containing 10, 25, and 50% tungsten mining sludge, and fired at 800, 950, and 1100 °C, are positioned in the yellow (b*+) and red (a*+) tonal quadrant. The lightness values of all samples range between 60% and 49% on the L* scale.

Table 8. Color values of the raw materials and ceramic products according to the CIE Lab 1976 system [194]. λ (dominant wavelength); L* (lightness); a* (red tone +, green tone –); b* (yellow tone +, blue tone –); ΔE (total color difference of the samples containing tungsten mining residues relative to the undoped samples at all firing temperatures).

	SAMPLE	λ		L*		a*		b*		ΔE
		$\bar{x}$	σ	$\bar{x}$	σ	$\bar{x}$	σ	$\bar{x}$	σ	
	CLAY	574,27	0,03	59,09	0,20	2,82	0,06	16,90	0,17	
	SLUDGE	572,29	0,05	53,79	0,19	0,36	0,02	5,98	0,04	
800 °C	CCL	586,18	0,37	53,11	0,31	19,31	0,92	25,44	1,00	0,00
	MC10L	585,15	0,20	58,27	0,81	19,04	0,66	26,63	0,88	5,30
	MC25L	586,90	0,22	55,68	0,32	22,59	0,50	29,33	0,46	5,70
	MC50L	585,20	0,44	53,42	1,62	19,55	0,86	28,28	0,80	2,87
950 °C	CCM	587,32	0,07	54,43	0,56	21,14	0,13	25,95	0,43	0,00
	MC10M	586,63	0,07	56,66	0,53	20,17	0,48	25,48	0,75	2,48
	MC25M	587,53	0,35	51,22	0,69	20,59	0,41	25,01	0,25	3,39
	MC50M	586,97	0,33	53,28	1,41	21,03	0,41	26,71	0,48	1,38
1100 °C	CCH	586,09	0,30	57,54	0,73	19,62	0,47	25,61	0,46	0,00
	MC10H	583,95	0,30	54,96	0,87	16,28	0,22	24,91	0,32	4,28
	MC25H	585,33	0,96	52,54	1,04	14,64	0,63	19,12	0,45	9,59
	MC50H	588,32	0,09	49,15	1,17	19,64	0,32	22,20	0,45	9,06

Regarding the unfired raw materials used in this study, both the clay and the sludge exhibit a predominant yellow tone. In the reconstructed color chart, based on the mean L*, a*, and b* values, they may appear to include greenish hues, although this is not the case quantitatively. The clay is more saturated and contains a higher proportion of yellow relative to red, almost six times higher, which, together with its lightness component, results in a yellowish and slightly pinkish washed-out color.

In contrast, the dominant tone of the additives is also yellow, with a much lower presence of the red component. In the raw state, the additives are almost seventeen times more yellow than red, and together with their very low lightness value, this produces a very pale yellow color, almost greyish. The differences in the yellow component between the clay and the sludge are approximately threefold in favor of the clay, while for the red component, the clay contains nearly eight times more than the additives.

The amount of yellow and red in both the clay and the sludge mainly derives from iron oxide in different mineral phases, chemical valence states, and hydration states, whether Fe_2O_3 (ferric oxide, red-brown hematite), FeO(OH) (ferric hydroxide, yellow-ochre goethite), or FeO (ferrous oxide, dark grey to black). It is noteworthy that the highest chemical proportion of Fe is found in the mining residues, approximately 11%, rather than in the clay, which contains about 6%. It becomes evident

© 2026 by the author(s). Distributed under a Creative Commons CC BY license.

Preprints.org (www.preprints.org) | NOT PEER-REVIEWED | Posted: 13 April 2026 doi:10.20944/preprints202604.0805.v1

that, due to the thermal transformation of these oxides and their incorporation into the ceramic materials, both with and without additives, the iron oxides present in the raw materials undergo oxidation during firing. This process leads them, at varying intensities, to shift toward red hues at the expense of yellow hues, in accordance with the characteristics of the firing process [195–197].

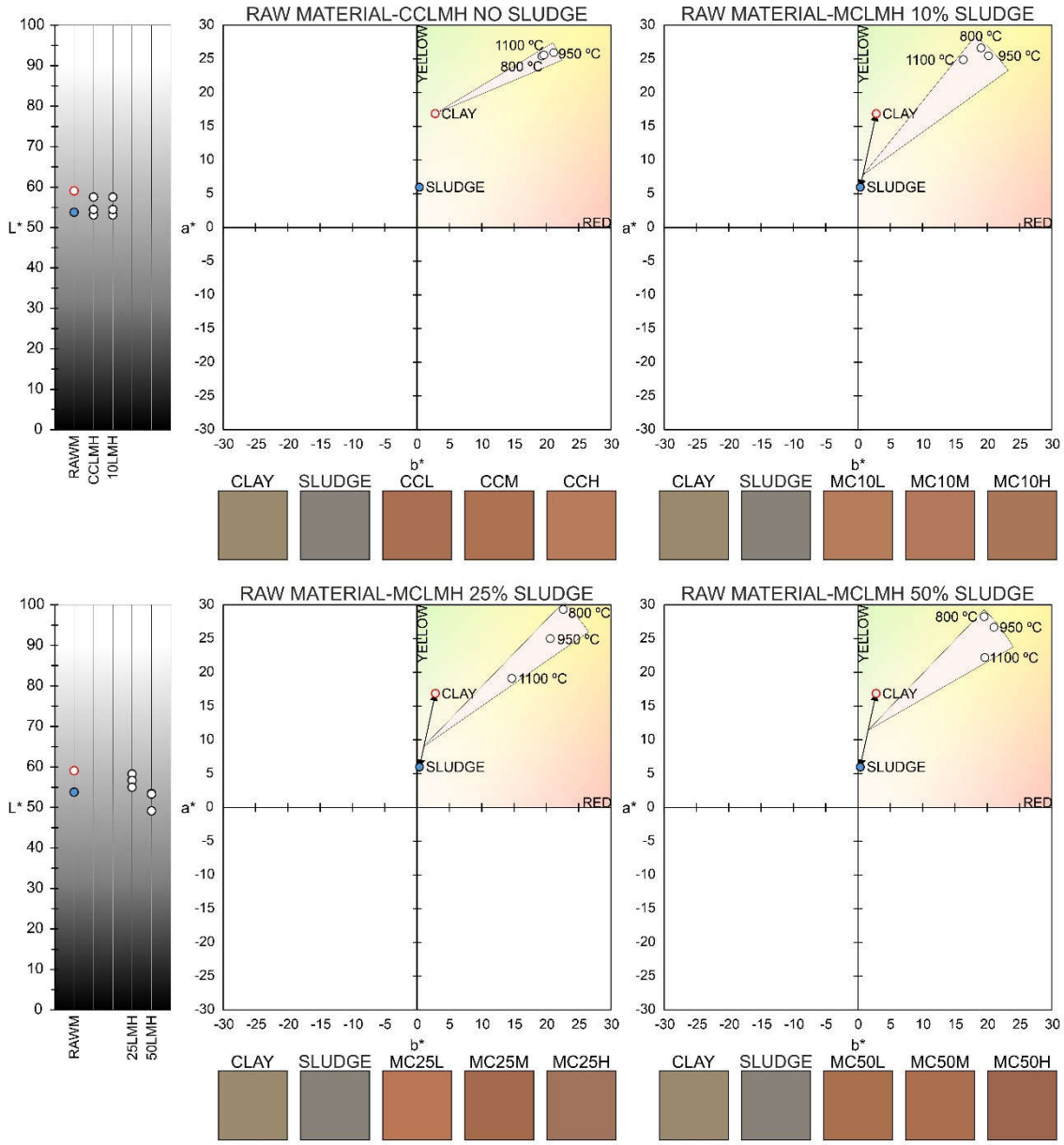

Figure 14. Colorimetry of the unfired raw materials and of the ceramic products without tungsten mining additives and of the sustainable bricks. On the left, L* values are shown for the raw materials and for the control ceramics fired at 800, 950, and 1100 °C, without mining residues. The chromaticity planes a* and b* are presented for all cases, including the raw materials (clay and sludge), together with the sustainable bricks doped with mining residues. At the bottom of each graph, the color charts of the unfired raw materials and of all the ceramic materials produced, both without mining sludge and with 10, 25, and 50% sludge, at all studied temperatures, are displayed.

With respect to all the ceramic samples analyzed, all ceramics, both with and without additives, are located in the yellow–red quadrant in the a*–b* chromaticity plane. Regarding lightness values, all ceramic materials fall between 58 and 49 percent as maximum and minimum, respectively, which suggests an appearance close to grey. In general, all ceramic materials at all studied temperatures

© 2026 by the author(s). Distributed under a Creative Commons CC BY license.

Preprints.org (www.preprints.org) | NOT PEER-REVIEWED | Posted: 13 April 2026 doi:10.20944/preprints202604.0805.v1

shift toward more orange hues compared to their unfired raw materials, whether they contain no additives, as in the case of the control ceramics, or are doped with mining residues, as in the case of the sustainable bricks at 10, 25, and 50 percent. Overall, the most saturated orange shifts occur at the highest firing temperature of 1100 °C.

Specifically, in the case of ceramics that do not contain mining residues, the chromatic variation from the clay raw material to the ceramic products at all firing temperatures results in a 100 percent increase in color saturation. Chromatically, this also represents an increase in the red hue relative to the yellow hue compared to the unfired state, although the red and yellow components do not reach an equal balance. The resulting color in the non-doped ceramics is an orange hue with a slight predominance of yellow. The lightness L* of all ceramics without additives decreases by almost 12 percent compared to the raw materials, and interestingly, the samples fired at the highest temperatures (950–1100 °C) display higher lightness values.

The effect of adding 10 percent mining residues, relative to the amount of clay in the recyclable ceramic products obtained (sustainable bricks), is analogous to that observed in the non-doped ceramics. The samples shift from yellow hues toward orange hues, although with a predominance of yellow over red. The increase in saturation, from the initial saturation of the raw mixture to the fired state, exceeds 300 percent. The lightness values observed at this proportion, compared to the non-doped ceramics, show higher lightness at lower temperatures, 800–950 °C, with values similar to those of the ceramics without additives.

For the ceramic mixtures with 25 percent mining residues, the effect is more pronounced, such that the samples appear more orange, particularly due to the influence of lightness L*, together with the higher additive content. In general, all samples are more luminous than the ceramics without additives. In the chromaticity plane, the ceramic samples show an increase in saturation of up to 300 percent compared with their unfired mixtures, except for the mixture fired at the highest temperature, 1100 °C, which exhibits lower saturation than the others, although still showing an increase above 140 percent. Their hues shift toward red from the original yellow hue, although the yellow component remains slightly higher. As a result, these samples display a highly saturated orange appearance.

Ceramic mixtures containing 50 percent mining residues experience increases in saturation above 200 percent, and, as occurs with the mixtures at other temperatures, they shift more intensely toward red hues. This effect is particularly evident in the sample with 50 percent residues fired at 1100 °C, which becomes the most orange of all the samples analyzed. This behavior is a consequence of the oxidation of the iron-bearing components present in the residues at that temperature, largely due to the transformation from goethite to hematite [198–203]. The lightness values, however, are lower than those of the non-doped ceramics, with an approximate 10 percent decrease in the L* value.

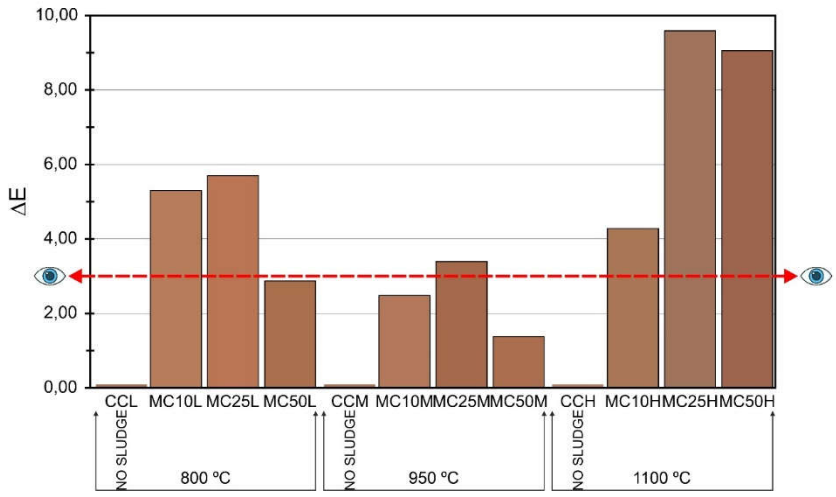

© 2026 by the author(s). Distributed under a Creative Commons CC BY license.

Preprints.org (www.preprints.org) | NOT PEER-REVIEWED | Posted: 13 April 2026 doi:10.20944/preprints202604.0805.v1

Figure 15. Total color differences (ΔE) of all ceramic bricks incorporating tungsten mining residues (10, 25, and 50%) relative to the control ceramics without residues, at firing temperatures of 800, 950, and 1100 °C. The red dashed line denotes the threshold of color differences perceptible to the human eye.

Finally, regarding the total color differences, ΔE*ab 1976 [194,204], the results show that all ceramic samples containing mining residues exhibit significant variations in the colorimetric parameters L*, a*, and b*, with greater or lesser magnitude. The observed changes range from slightly above 1 unit to nearly 10 units [205–208]. The largest differences generally occur in the ceramics fired at the highest temperature, 1100 °C, particularly in those doped with 25 and 50 percent residues, while notably smaller differences appear in the samples fired at intermediate temperature, 950 °C, compared with those fired at the lowest temperature, 800 °C. Almost all ceramic samples doped with mining residues present variations perceptible to the human eye according to [209], except for the samples with 50 percent tungsten mining residues fired at 800 °C, and those with 10 and 50 percent residues fired at 950 °C.

All the chromatic changes observed in these ceramic bricks produced from the recycling of clays and tungsten mining sludge are of fundamental importance for sustainable construction, architectural rehabilitation, and the restoration and conservation of architectural heritage. In particular, the ability to control the final color of sustainable ceramic products through the greater or lesser addition of mining residues and the adjustment of firing temperature is especially valuable [210–213].

4. Discussion

The chemical composition of the raw materials shows that both the clay and the mining sludges consist predominantly of SiO_2 and Al_2O_3, a feature that ensures suitable ceramic behaviour. The fluxing oxides (CaO, K_2O, Na_2O, MgO, Fe_2O_3) promote a decrease in the vitrification temperature and enhance matrix densification. Although the mining sludges contain relevant concentrations of potentially hazardous elements, particularly As and F, their incorporation into ceramic mixtures enables their immobilization within appropriate firing temperature ranges. Overall, from a compositional standpoint, the chemical complementarity between clay and mining sludges supports their suitability for producing sustainable bricks across wide firing intervals [214–216].

The mineralogy of the clays and mining sludges includes phases suitable for ceramic development, notably phyllosilicates (illite, kaolinite, muscovite, paragonite), quartz, and minor proportions of carbonates, which control the main thermal transformations. From 950 °C up to 1100 °C, anorthite and diopside form [217,218], promoted by the Ca and Mg contributions derived from tungsten mining residues, indicating good ceramic reactivity, enhanced densification, and reduced porosity. The absence of mullite at low residue additions may be related to a deficit of aluminosilicates and fluxing phases in the mixtures, affecting "ceramic maturity." Overall, the mineralogical assessment demonstrates that the controlled incorporation of residues, particularly at 25–50%, promotes stable and technologically favourable phases for sustainable brick production, improving densification, thermal stability, and mechanical performance.

Water absorption depends on both the firing temperature and the tungsten-residue content. Bricks containing 50% residue exhibit the lowest absorption values (16.16–13.73%), with only a 4% variation across temperatures, revealing a well-sintered microstructure at 1100 °C dominated by nanopores. This more compact structure clearly reduces water uptake compared with the other formulations and suggests that higher residue contents generate more densified and stable matrices, resulting in improved durability [219,220].

Mercury intrusion porosimetry confirms that both total porosity and pore-size distribution depend on the firing temperature and on the tungsten-residue content. Increasing temperature reduces the porosity accessible to water and gases (from the perspective of hydraulic testing), particularly in formulations containing 50% additive, where a higher degree of matrix densification is observed due to the fluxing action of the tungsten mining residue. The pore-size distribution is

© 2026 by the author(s). Distributed under a Creative Commons CC BY license.

Preprints.org (www.preprints.org) | NOT PEER-REVIEWED | Posted: 13 April 2026 doi:10.20944/preprints202604.0805.v1

essentially unimodal and dominated by macropores, although its evolution varies among mixtures: in ceramics without residue, macropores decrease with temperature, whereas in residue-bearing formulations they increase due to the formation of vacuoles associated with gas release. Mesopores show high variability, and air voids or cracks are scarce, being more closely related to shrinkage-induced stresses than to residue incorporation. Overall, the mining sludges act as microstructural modifiers, adjusting porosity and promoting densification in sustainable ceramic materials during firing [220,221].

Ultrasonic testing shows that both the firing temperature and the tungsten-residue content have a clear influence on the ultrasonic pulse velocity (Vp). Unfired samples exhibit low Vp values, with slight increases attributed to the mechanical effect of the sludge. After firing, the control ceramics progressively increase their Vp as a result of densification and glass-phase formation. In the sustainable bricks, the simultaneous increase in temperature and residue content further enhances Vp, particularly at 1100 °C, where the formulations containing 50% residue display the highest compaction levels. This behaviour confirms the fluxing and structural role of the residue, which promotes denser microstructures and improved mechanical performance [222–224].

Compressive strength shows a clear dependence on both firing temperature and tungsten-residue content. Ceramics without additives increase their strength at 800 and 950 °C but exhibit a decrease at 1100 °C, likely due to over-vitrification and microcracking associated with rapid firing. In contrast, the sustainable bricks display a continuous increase in strength with temperature, highlighting the densifying effect of the sludge through enhanced glass-phase formation and effective sintering. The maximum value is obtained in MC25H (26.19 MPa), indicating that a 25% residue content provides an optimal balance between vitrification, stability, and cohesion. Although the mixtures with 50% residue do not surpass this value, they maintain strengths higher than those of the residue-free ceramics. Moreover, all formulations comfortably meet regulatory requirements (>9.81 MPa for solid bricks and >4.90 MPa for hollow units), confirming the potential of mining residue to improve the mechanical performance of sustainable ceramic bricks [225–227].

Electron microscopy images highlight a marked compositional heterogeneity consistent with the clay-based raw materials and the tungsten residues. At 800 °C, underfired textures predominate, characterized by dehydroxylated phyllosilicates, minimally altered grains, and irregular pores, with no evidence of vitrification. At 950 °C, a partially densified matrix is observed, with narrower interparticle contacts and incipient thermal alterations in quartz and carbonates, together with metallic aggregates derived from the residue (Fe, Zn). At 1100 °C, vitrification becomes dominant, especially in the residue-bearing mixtures, where vacuoles resulting from gas release and mullite recrystallization appear, indicating advanced sintering and greater “ceramic maturity.” Overall, the observations confirm that the residue acts as an effective flux, accelerating glass-phase formation and modifying microstructural evolution, particularly at 25–50% additions and at high firing temperatures [228].

Leaching tests demonstrate that the incorporation of mining sludges into ceramic matrices significantly reduces the mobility of heavy metals compared with the untreated residue, at both 800 °C and 1100 °C. The pronounced decrease in As, Cd, Zn, Mn, Co, and Ni, with reductions ranging from two to more than four orders of magnitude, confirms highly effective encapsulation associated with vitrification and pore closure within the ceramic matrix. Although tungsten and arsenic exhibit higher leaching values than the rest, their concentrations remain far below those of the non-encapsulated residue, likely due to the formation of phases with variable stability during firing and to slight variations in eluate pH. Overall, the results indicate that these sustainable bricks immobilize toxic elements with high efficiency, supporting their environmental suitability and their capacity to stabilize mining wastes in durable ceramic products [229].

CIELab analysis shows that all ceramic formulations fall within the yellow-red quadrant, controlled by the iron content and its thermal transformations. Firing induces a progressive shift toward more orange hues, with clear increases in a* and decreases in L*, an effect that is more pronounced at 1100 °C and in mixtures with higher sludge contents, where oxidation during firing

© 2026 by the author(s). Distributed under a Creative Commons CC BY license.

Preprints.org (www.preprints.org) | NOT PEER-REVIEWED | Posted: 13 April 2026 doi:10.20944/preprints202604.0805.v1

and vitrification enhance color saturation with the appearance of hematite. Additions of 25 to 50 percent reinforce this behaviour due to their higher iron contribution and the initial reduction in luminosity, resulting in redder, more saturated, and darker materials. The ΔE variations are, in most cases, perceptible to the human eye when compared with the control ceramics, especially at elevated temperatures. Overall, the proportion of residue and the firing temperature allow the final color to be modulated in a reproducible manner, which adds value for architectural and conservation applications where chromatic response is a highly relevant parameter [230,231].

5. Conclusions

As a general observation, both the firing temperature and the proportion of tungsten mining sludge govern the overall ceramic behaviour of the sustainable bricks developed in this study, since they determine fundamental factors such as mineralogy, densification variations, pore structure, and mechanical performance, while also enhancing environmental sustainability and color development. These two variables, particularly at waste incorporation levels of 25–50% and under high-temperature firing conditions, promote the formation of stable compounds with optimal sintering, thereby strengthening the newly produced materials and ensuring the immobilization of toxic elements, resulting in improved technical, aesthetic, and environmental properties of the sustainable ceramic bricks generated in this work. Accordingly, with regard to the technical ceramic performance, the following specific conclusions can be drawn:

1. There is a high chemical compatibility between the raw materials and a strong degree of sustainability in the ceramic transformation process, since both the clays and the mining residues exhibit high SiO_2 and Al_2O_3 contents, balanced by fluxing oxides. This indicates that an appropriate stoichiometric balance is achieved to enable an efficient ceramic reaction.

2. The formation of stable mineral phases is promoted by the composition of the raw materials, since anorthite and diopside develop between 950 and 1100 °C when incorporating 25–50% of mining residue, thereby enhancing the densification of the ceramic matrix, even though mullite recrystallization does not occur at low residue contents.

3. Porosity and water absorption are directly associated with microstructural densification, as evidenced by porosimetry, water absorption tests, and ESEM analyses. Mixtures containing 50% sludge develop highly dense matrices with nanopores at 1100 °C, which results in very low water absorption. Vacuoles appear as a consequence of gas release, attributable to the effectiveness of the residue acting as an efficient flux.

4. The sustainable bricks exhibit good mechanical properties and effective structural consolidation, as demonstrated by the increases in ultrasonic pulse velocity and compressive strength, both of which reflect progressive densification. The control ceramics improve up to 950 °C but weaken at 1100 °C due to the appearance of microcracks caused by internal shrinkage, whereas the sustainable bricks show exponential improvement, reaching their optimal performance at a 25% additive content. In all cases, the formulations far exceed the regulatory requirements for mechanical performance, confirming their suitability for sustainable construction applications.

5. Finally, it can be stated that the sustainable bricks exhibit very high environmental stability, since the excellent vitrification and pore closure reduce the mobility of heavy metals by two to four orders of magnitude, ensuring the viability of the sustainable ceramic bricks. Additionally, through appropriate adjustment of additive proportions and firing temperature, it is possible to induce controlled chromatic modulation based on ΔE monitoring and its alignment with human perceptibility thresholds.

Author Contributions: Conceptualization, J.A.D-S, M.P.S-P, A.M-R and L.C-L; methodology, J.A.D-S, M.P.S-P, A.M-R and L.C-L; validation, J.A.D-S, M.P.S-P, A.M-R and L.C-L; formal analysis, J.A.D-S, M.P.S-P, A.M-R and L.C-L; investigation, J.A.D-S, M.P.S-P, A.M-R and L.C-L; resources, J.A.D-S, M.P.S-P, A.M-R and L.C-L; data curation, J.A.D-S, M.P.S-P, A.M-R and L.C-L; writing—original draft preparation, J.A.D-S, M.P.S-P, A.M-R and L.C-L; writing—review and editing, J.A.D-S, M.P.S-P, A.M-R and L.C-L; visualization, J.A.D-S, M.P.S-P, A.M-R

© 2026 by the author(s). Distributed under a Creative Commons CC BY license.

Preprints.org (www.preprints.org) | NOT PEER-REVIEWED | Posted: 13 April 2026 doi:10.20944/preprints202604.0805.v1

and L.C-L; supervision, J.A.D-S, M.P.S-P, A.M-R and L.C-L; project administration, J.A.D-S, M.P.S-P, A.M-R and L.C-L; funding acquisition, J.A.D-S, M.P.S-P, A.M-R and L.C-L. All authors have read and agreed to the published version of the manuscript.

Funding: This research was funded by the Research Project PPJIB2022-17, "Development of High-Performance Bricks Incorporating Organic and Inorganic Waste Additives", from the Plan Propio, University of Granada 2022 Grants. It was also supported by the ERA-MIN3/0002/2023 project (https://doi.org/10.54499/ERAMIN3/0002/2023), funded by the ERA-MIN3/0002/2023 project (https://doi.org/10.54499/ERAMIN3/0002/2023) funded by ERA-MIN3, co-funded by the Horizon 2020 programme of the European Union and the action "PCI2024-153488 Project", funded by MICIU/AEI /10.13039/501100011033 and by FEDER, EU, and by the REMINE Project from the Horizon 2020 Marie Skłodowska-Curie Actions Programme. This research was carried out under the auspices of the Research Groups HUM-629 and RNM-0179 of the Junta de Andalucía.

Data Availability Statement: Data are contained within the article.

Acknowledgments: We would like to thank Cerámica Castillo Siles (https://ceramicacastillosiles.es/) for providing the clay-based raw material residues from Víznar, Granada, Spain, and Beralt Tin and Wolfram, Panasqueira Mine (https://almonty.com/project/panasqueira-mine/), through the Universidade da Beira Interior (UBI), for supplying the tungsten mining residues from Covilhã, Portugal. We also gratefully acknowledge the support of C-MADE (Centre of Materials and Civil Engineering for Sustainability) and C-MAST (Centre for Mechanical and Aerospace Science and Technologies), both from the Universidade da Beira Interior, as well as the CIC (Scientific Instrumentation Centre of the University of Granada).

Conflicts of Interest: The authors declare no conflicts of interest.

Abbreviations

The following abbreviations are used in this manuscript:

CCL	Control ceramic without tungsten-mining additive fired at 800 °C
CCM	Control ceramic without tungsten-mining additive fired at 950 °C
CCH	Control ceramic without tungsten-mining additive fired at 1100 °C
MC10L	Sustainable brick with 10% tungsten-mining residue fired at 800 °C
MC10M	Sustainable brick with 10% tungsten-mining residue fired at 950 °C
MC10H	Sustainable brick with 10% tungsten-mining residue fired at 1100 °C
MC25L	Sustainable brick with 25% tungsten-mining residue fired at 800 °C
MC25M	Sustainable brick with 25% tungsten-mining residue fired at 950 °C
MC25H	Sustainable brick with 25% tungsten-mining residue fired at 1100 °C
MC50L	Sustainable brick with 50% tungsten-mining residue fired at 800 °C
MC50M	Sustainable brick with 50% tungsten-mining residue fired at 950 °C
MC50H	Sustainable brick with 50% tungsten-mining residue fired at 1100 °C
Al	Absorption coefficient
Ac	Volumetric absorption
ID	Drying index
M_s	Saturated mass as a function of time
M_0	Dry mass
ΔM	Water mass loss
NF	Unfired sample

© 2026 by the author(s). Distributed under a Creative Commons CC BY license.

Preprints.org (www.preprints.org) | NOT PEER-REVIEWED | Posted: 13 April 2026 doi:10.20944/preprints202604.0805.v1

References

1. Statista Research Department. Evolución anual de la producción mundial de minerales de 2005 a 2021. Available online: https://es.statista.com/estadisticas/729104/produccionminera-mundial/ (accessed on 6 April 2024).
2. Adiansyah, J.S.; Rosano, M.; Vink, S.; Keir, G. A framework for a sustainable approach to mine tailings management: Disposal strategies. *J. Clean. Prod.* **2015**, *108*, 1050–1062. https://doi.org/10.1016/j.jclepro.2015.07.139
3. Romero, M.; Padilla, I.; Contreras, M.; López-Delgado, A. Mullite-based ceramics from mining waste: A review. *Minerals* **2021**, *11*, 332. https://doi.org/10.3390/min11030332
4. Araujo, F.S.M.; Taborda-Llano, I.; Nunes, E.B.; Santos, R.M. Recycling and reuse of mine tailings: A review of advancements and their implications. *Geosciences* **2022**, *12*, 319. https://doi.org/10.3390/geosciences12090319
5. Amrani, M.; Taha, Y.; Kchikach, A.; Benzaazoua, M.; Hakkou, R. Valorization of phosphate mine waste rocks as materials for road construction. *Minerals* **2019**, *9*, 237. https://doi.org/10.3390/min9040237
6. Amrani, M.; Taha, Y.; Elghali, A.; Benzaazoua, M.; Kchikach, A.; Hakkou, R. An experimental investigation on collapsible behavior of dry compacted phosphate mine waste rock in road embankment. *Transp. Geotech.* **2021**, *26*, 100439. https://doi.org/10.1016/j.trgeo.2020.100439
7. Segui, P.; Safhi, A.E.M.; Amrani, M.; Benzaazoua, M. Mining wastes as road construction material: A review. *Minerals* **2023**, *13*, 90. https://doi.org/10.3390/min13010090
8. Kinnunen, P.; Obenaus-Emler, R.; Raatikainen, J.; Guignot, S.; Guimera, J.; Ciroth, A.; Heiskanen, K. Review of closed water loops with ore sorting and tailings valorisation for a more sustainable mining industry. *J. Clean. Prod.* **2021**, *278*, 123237. https://doi.org/10.1016/j.jclepro.2020.123237
9. Hefni, M.; Ahmed, H.A.M.; Omar, E.S.; Ali, M.A. The potential re-use of Saudi mine tailings in mine backfill: A path towards sustainable mining in Saudi Arabia. *Sustainability* **2021**, *13*, 6204. https://doi.org/10.3390/su13116204
10. Bazaluk, O.; Petlovanyi, M.; Lozynskyi, V.; Zubko, S.; Sai, K.; Saik, P. Sustainable underground iron ore mining in Ukraine with backfilling worked-out area. *Sustainability* **2021**, *13*, 834. https://doi.org/10.3390/su13020834
11. Ostrowski, K.; Stefaniuk, D.; Sadowski, Ł.; Krzywiński, K.; Gicala, M.; Różańska, M. Potential use of granite waste sourced from rock processing as coarse aggregate in high-performance self-compacting concrete. *Constr. Build. Mater.* **2020**, *238*, 117794. https://doi.org/10.1016/j.conbuildmat.2019.117794
12. Durán, J.A.; García, A. Piedra artificial porosa a partir de residuos de rocas ornamentales adaptable a obras de construcción y restauración patrimonial. *Bol. Geol. Minero* **2017**, *128*, 437–450. https://doi.org/10.21701/bolgeomin.128.2.011
13. Xu, X.; Song, J.; Li, Y.; Wu, J.; Liu, X.; Zhang, C. Microstructure and properties of ceramic tiles from solid wastes of Bayer red muds. *Constr. Build. Mater.* **2019**, *212*, 266–274. https://doi.org/10.1016/j.conbuildmat.2019.03.280
14. Fernandes, J.V.; Guedes, D.G.; Costa, F.P.; Rodrigues, A.M.; Neves, G.D.A.; Menezes, R.R.; Santana, L.N.L. Sustainable ceramic materials manufactured from ceramic formulations containing quartzite and scheelite tailings. *Sustainability* **2020**, *12*, 9417. https://doi.org/10.3390/su12229417
15. Almeida, E.P.; Carreiro, M.E.A.; Rodrigues, A.M.; Ferreira, H.S.; Santana, L.N.L.; Menezes, R.R.; Neves, G.A. A new eco-friendly mass formulation based on industrial mining residues for ceramic tiles. *Ceram. Int.* **2021**, *47*, 11340–11348. https://doi.org/10.1016/j.ceramint.2020.12.260
16. Simão, F.V.; Chambart, H.; Vandemeulebroeke, L.; Cappuyns, V. Incorporation of sulphidic mining waste in ceramic roof tiles and blocks. *J. Geochem. Explor.* **2021**, *225*, 106741. https://doi.org/10.1016/j.gexplo.2021.106741
17. Lemougna, P.N.; Yliniemi, J.; Nguyen, H.; Adesanya, E.; Tanskanen, P.; Kinnunen, P.; Rönning, J.; Illikainen, M. Utilisation of glass wool waste and mine tailings in high performance building ceramics. *J. Build. Eng.* **2020**, *31*, 101383. https://doi.org/10.1016/j.jobe.2020.101383

© 2026 by the author(s). Distributed under a Creative Commons CC BY license.

Preprints.org (www.preprints.org) | NOT PEER-REVIEWED | Posted: 13 April 2026 doi:10.20944/preprints202604.0805.v1

18. Arancibia, J.R.H.; Alfonso, M.P.; García-Vallès, M.; Martínez, S.; Canet, C.; Romero, F.M. Obtención de vidrio a partir de residuos de la minería del estaño en Bolivia. *Bol. Soc. Esp. Ceram. Vidrio* **2013**, *52*, 143–150. https://doi.org/10.3989/cyv.192013
19. Alfonso, P.; Tomasa, O.; Garcia-Valles, M.; Tarragó, M.; Martínez, S.; Esteves, H. Potential of tungsten tailings as glass raw materials. *Mater. Lett.* **2018**, *228*, 456–458. https://doi.org/10.1016/j.matlet.2018.06.098
20. Huang, B.; Feng, Q.; An, D.; Zhang, J. Use of mine tailings as precast construction materials through alkali activation. *Min. Metall. Explor.* **2020**, *37*, 251–265. https://doi.org/10.1007/s42461-019-00149-w
21. Qaidi, S.M.; Tayeh, B.A.; Zeyad, A.M.; Azevedo, A.R.; Ahmed, H.U.; Emad, W. Recycling of mine tailings for geopolymers production: A systematic review. *Case Stud. Constr. Mater.* **2022**, *16*, e00933. https://doi.org/10.1016/j.cscm.2022.e00933
22. Kiventerä, J.; Perumal, P.; Yliniemi, J.; Illikainen, M. Mine tailings as raw material in alkali activation: A review. *Int. J. Miner. Metall. Mater.* **2020**, *27*, 1009–1020. https://doi.org/10.1007/s12613-020-2129-6
23. European Commission. A new circular economy action plan for a cleaner and more competitive Europe. *COM(2020)98* **2020**. Available online: https://eur-lex.europa.eu/legal-content/EN/TXT/?uri=celex:52020DC0098
24. European Commission. Interpretative communication on waste and byproducts. **2026**. Available online: http://europa.eu.int/eur-lex/lex/LexUriServ/LexUriServ.do?uri=CELEX:52007DC0059:ES:HTML
25. Makhathini, T.P.; Bwapwa, J.K.; Mtsweni, S. Various options for mining and metallurgical waste in the circular economy: A review. *Sustainability* **2023**, *15*, 2518. https://doi.org/10.3390/su15032518
26. Cobîrzan, N.; Muntean, R.; Thalmaier, G.; Felseghi, R.A. Recycling of mining waste in masonry unit production. *Materials* **2022**, *15*, 594. https://doi.org/10.3390/ma15020594
27. Ally, A.N.; Blanche, M.M.; Nana, U.J.P.; Grâce, M.M.; François, N.; Pettang, C. Recovery of mining wastes in building materials: A review. *Open J. Civ. Eng.* **2021**, *11*, 379–397. https://doi.org/10.4236/ojce.2021.114022
28. Phonphuak, N.; Saengthong, C.; Srisuwan, A. Physical and mechanical properties of fired clay bricks with rice husk waste addition. *Mater. Today Proc.* **2019**, *17*, 1668–1674. https://doi.org/10.1016/j.matpr.2019.06.197
29. Lawanwadeekul, S.; Otsuru, T.; Tomiku, R.; Nishiguchi, H. Thermal-acoustic clay brick production with added charcoal. *Constr. Build. Mater.* **2020**, *255*, 119376. https://doi.org/10.1016/j.conbuildmat.2020.119376
30. Cultrone, G.; Aurrekoetxea, I.; Casado, C.; Arizzi, A. Sawdust recycling in lightweight bricks. *Constr. Build. Mater.* **2020**, *235*, 117436. https://doi.org/10.1016/j.conbuildmat.2019.117436
31. Silva, V.J.D.; Taveira, S.K.; Silva, K.R.; Neves, G.A.; Lira, H.L.; Santana, L.N. Refractory ceramics of clay and alumina waste. *Mater. Res.* **2021**, *24*, e20200485. https://doi.org/10.1590/1980-5373-MR-2020-0485
32. Shaqour, E.N.; Abo Alela, A.H.; Rsheed, A.A. Improved compressive strength of fired bricks by recycling blacksmith workshop wastes. *J. Eng. Appl. Sci.* **2021**, *68*, 1–14. https://doi.org/10.1186/s44147-021-00002-2
33. Priyadarshini, M.; Giri, J.P.; Patnaik, M. Variability in compressive strength of non-conventional bricks containing agro and industrial waste. *Case Stud. Constr. Mater.* **2021**, *14*, e00506. https://doi.org/10.1016/j.cscm.2021.e00506
34. Luo, L.; Li, K.; Fu, W.; Liu, C.; Yang, S. Composite sintered bricks from shale, sewage sludge, coal gangue powder and iron ore tailings. *Constr. Build. Mater.* **2020**, *232*, 117250. https://doi.org/10.1016/j.conbuildmat.2019.117250
35. Marrocchino, E.; Zanelli, C.; Guarini, G.; Dondi, M. Recycling mining and construction wastes as temper in clay bricks. *Appl. Clay Sci.* **2021**, *209*, 106152. https://doi.org/10.1016/j.clay.2021.106152
36. Simão, F.V.; Chambart, H.; Vandemeulebroeke, L.; Nielsen, P.; Adrianto, L.R.; Pfister, S.; Cappuyns, V. Mine waste as resource for facing bricks. *J. Clean. Prod.* **2022**, *368*, 133118. https://doi.org/10.1016/j.jclepro.2022.133118
37. Guo, Y.; Wang, C.; Li, S.; He, Y.; Liu, H. Permeable ceramic bricks with tungsten tailings by two-stage calcination. *Constr. Build. Mater.* **2024**, *411*, 134382. https://doi.org/10.1016/j.conbuildmat.2023.134382
38. Demir, I. Effect of organic residues addition on clay brick properties. *Waste Manag.* **2008**, *28*, 622–627. https://doi.org/10.1016/j.wasman.2007.03.019
39. Suvorova, O.; Kumarova, V.; Nekipelov, D.; Selivanova, E.; Makarov, D.; Masloboev, V. Construction ceramics from ore dressing waste in Murmansk region. *Constr. Build. Mater.* **2017**, *153*, 783–789. https://doi.org/10.1016/j.conbuildmat.2017.07.137

© 2026 by the author(s). Distributed under a Creative Commons CC BY license.

Preprints.org (www.preprints.org) | NOT PEER-REVIEWED | Posted: 13 April 2026 doi:10.20944/preprints202604.0805.v1

40. Castro-Gomes, J.P.; Silva, A.P.; Cano, R.P.; Durán Suarez, J.; Albuquerque, A. Reuse of tungsten mining waste-rock in value-added products. *J. Clean. Prod.* **2012**, *25*, 34–41. https://doi.org/10.1016/j.jclepro.2011.11.064
41. Montoya Herrera, J. Nuevos materiales cerámicos a partir de reutilización de residuos pétreos de minería. Digibug, 2014. https://doi.org/9788491250197
42. Sangiorgi, C.; Lantieri, C.; Tataranni, P.; Castro-Gomes, J.; Gabriel, M. Reuse of mining waste into alkali-activated materials. *CRC Press EBooks* **2016**, 1735–1744. https://doi.org/10.1201/9781315643274-190
43. Sedira, N.; Castro-Gomes, J.; Magrinho, M. Red clay brick and tungsten mining waste-based alkali-activated binder. *Constr. Build. Mater.* **2018**, *190*, 1034–1048. https://doi.org/10.1016/j.conbuildmat.2018.09.153
44. Beghoura, I.; Castro-Gomes, J. Density-based mining waste alkali-activated foamed materials with expanded cork. *CivilEng* **2021**, *2*, 523–540. https://doi.org/10.3390/civileng2020029
45. Grünhäuser Soares, E.; Castro-Gomes, J.; Sitarz, M.; Zdeb, T.; Hager, I.; Hassan, K.; Saif Al-Kuwari, M. Co-utilisation of carbonated reactive magnesia cement and industrial wastes. *Constr. Build. Mater.* **2022**, *323*, 126488. https://doi.org/10.1016/j.conbuildmat.2022.126488
46. González, M.V. Síntesis y desarrollo de materiales cerámicos con desechos. **2019**. Available online: http://riaa.uaem.mx/handle/20.500.12055/925
47. Suárez-Macías, J.; Terrones-Saeta, J.M.; Iglesias-Godino, F.J.; Corpas-Iglesias, F.A. Retention of contaminant elements from lead mine tailings in ceramics. *Minerals* **2020**, *10*, 576. https://doi.org/10.3390/min10060576
48. Crespo-López, L.; Martínez-Ramirez, A.; Sebastián, E.; Cultrone, G. Pomace as additive for lightweight eco-bricks. *Appl. Clay Sci.* **2023**, *243*, 107084. https://doi.org/10.1016/j.clay.2023.107084
49. Ruiz, A.M.; Ferhat, G.; Alfaro, P.; Sanz de Galdeano, C.; de Lacy, M.C.; Rodríguez-Caderot, G.; Gil, A.J. Geodetic measurements of crustal deformation on NW–SE faults of the Betic Cordillera, southern Spain, 1999–2001. *J. Geodyn.* **2003**, *35*, 259–272. https://doi.org/10.1016/S0264-3707(02)00134-5
50. Moschella, M.; Ciaccio, M.G.; Latorre, D. Minor earthquake sequences in the Amatrice–Norcia epicentral area (Central Italy). *Tectonophysics* **2021**, *809*, 228858. https://doi.org/10.1016/j.tecto.2021.228858
51. Breiter, K.; Ďurišová, J.; Korbelová, Z.; Vašinová Galiová, M.; Hložková, M. Granite pluton at the Panasqueira tungsten deposit, Portugal: Genetic implications as revealed from new geochemical data. *Minerals* **2023**, *13*, 163. https://doi.org/10.3390/min13020163
52. Losantos, E.; Borrajo, I.; Losada, I.; Boixet, L.; Castelo Branco, J.M.; Tornos, F. Sn and W mineralisation in the Iberian Peninsula. *Ore Geol. Rev.* **2025**, *179*, 106542. https://doi.org/10.1016/j.oregeorev.2025.106542
53. Sangiorgi, C.; Lantieri, C.; Tataranni, P.; Castro-Gomes, J.; Gabriel, M. Reuse of mining waste into innovative alkali-activated-based materials for road pavement applications. *CRC Press EBooks* **2016**, 1735–1744. https://doi.org/10.1201/9781315643274-190
54. Gonçalves, A. Mining operation and environmental impacts: the case of Panasqueira Mines. *Imprensa da Universidade de Coimbra EBooks* **2016**, 53–66. https://doi.org/10.14195/978-989-26-1237-9_2
55. Pires, M. Minas da Panasqueira: atividade mineira, impactos ambientais e comunidades locais. **2025**. Available online: http://hdl.handle.net/10400.2/16071
56. Mateus, A.; Figueiras, J.; Martins, I.; Rodrigues, P.; Pinto, F. Relative abundance and compositional variation of silicates, oxides and phosphates in the W–Sn-rich lodes of the Panasqueira Mine (Portugal): Implications for the ore-forming process. *Minerals* **2020**, *10*, 551. https://doi.org/10.3390/min10060551
57. Snee, L.W.; Sutter, J.F.; Kelly, W.C. Thermochronology of economic mineral deposits: Dating stages of mineralization at Panasqueira, Portugal, by high-precision $^{40}Ar/^{39}Ar$ age spectrum techniques on muscovite. *Econ. Geol.* **1988**, *83*, 335–354. https://doi.org/10.2113/gsecongeo.83.2.335
58. Candeias, C.; Melo, R.; Ávila, P.F.; Ferreira da Silva, E.; Salgueiro, A.R.; Teixeira, J.P. Heavy metal pollution in mine soil–plant system in S. Francisco de Assis, Panasqueira mine (Portugal). *Appl. Geochem.* **2014**, *44*, 12–26. https://doi.org/10.1016/j.apgeochem.2013.07.009
59. Carocci, E.; Marignac, C.; Cathelineau, M.; Truche, L.; Lecomte, A.; Pinto, F. Rutile from Panasqueira (Central Portugal): An excellent pathfinder for wolframite deposition. *Minerals* **2018**, *9*, 9. https://doi.org/10.3390/min9010009

© 2026 by the author(s). Distributed under a Creative Commons CC BY license.

Preprints.org (www.preprints.org) | NOT PEER-REVIEWED | Posted: 13 April 2026 doi:10.20944/preprints202604.0805.v1

60. UNE-EN 13755. Natural stone test methods. Determination of water absorption at atmospheric pressure. AENOR, Madrid, **2008**. Available online: https://www.une.org/encuentra-tu-norma/busca-tu-norma/norma?c=N0042047
61. NORMAL 29/88. Misura dell'indice di asciugamento (drying index). CNR-ICR, Roma, **1988**.
62. ASTM International. D4404-18: Standard test method for determination of pore volume and pore volume distribution of soil and rock by mercury intrusion porosimetry. West Conshohocken, PA, **2018**. https://doi.org/10.1520/D4404-18
63. ASTM International. ASTM D2845-08: Standard test method for laboratory determination of pulse velocities and ultrasonic elastic constants of rock (withdrawn 2017). West Conshohocken, PA, **2008**. https://store.astm.org/d2845-08.html
64. UNE-EN 1926:2007. Natural stone test methods—Determination of uniaxial compressive strength. AENOR, Madrid, **2019**. https://tienda.aenor.com/norma-une-en-1926-2007-n0038620
65. ASTM International. ASTM C170/C170M-24a: Standard test method for compressive strength of dimension stone. West Conshohocken, PA, **2024**. https://doi.org/10.1520/C0170_C0170M-24A
66. UNE-EN 772-5:2016. Methods of test for masonry units—Part 5: Determination of the active soluble salts content of clay masonry units. AENOR, Madrid, **2016**. https://tienda.aenor.com/norma-une-en-772-5-2016-n0057297
67. Suárez-Macías, J.; Terrones-Saeta, J.M.; Iglesias-Godino, F.J.; Corpas-Iglesias, F.A. Retention of contaminant elements from tailings from lead mine washing plants in ceramics for bricks. *Minerals* **2020**, *10*, 576. https://doi.org/10.3390/min10060576
68. Agua, F.; Quijada, F.; Pinilla, A.; García, M.; Villegas, M.A. *Manual de sensores de pH ambiental para la conservación preventiva del Patrimonio Cultural*. **2025**. Available online: https://www.calameo.com/books/003341477d685f6ca88ab
69. AENOR. UNE-EN 15886:2010. Cultural Heritage—Conservation of cultural property—Test methods—Measurement of surface colour. Madrid, **2011**. https://www.une.org/encuentra-tu-norma/busca-tu-norma/norma?c=N0046629
70. Zheng, C.; Li, D.; Guo, M.; Zhang, J.; Xie, J.; Han, J. The Microstructure, Crystallization Behavior, and Mechanical Performance Evolutions of Li_2O–Al_2O_3–SiO_2 Glass and Glass–Ceramics with Different Alkaline Earth Oxide Modifications. *Materials* **2025**, 18, 1383. https://doi.org/10.3390/ma18061383
71. Pei, Z.; Huang, H.; Guo, X.; Zhang, J.; Chen, M. Preparation and Properties of MgO–Al_2O_3–SiO_2 Glass–Ceramics with Controllable Crystalline Phases. *Crystals* **2023**, 13, 1261. https://doi.org/10.3390/cryst13081261
72. Xie, J.; Li, N.; Shang, P.; He, Z.; Zhao, L.; He, F. The Effect of the Variation in Al_2O_3 and SrO Content on the Structure, Sintering Behavior, and Properties of SrO, BaO, ZnO, MgO–B_2O_3–Al_2O_3–SiO_2 Glass-Ceramics for Use in Al_2O_3 Ceramic LTCC Applications. *Materials* **2025**, 18, 4510. https://doi.org/10.3390/ma18194510
73. Amorós, J.L.; Blasco, E.; Moreno, A.; Marín, N.; Feliu, C. Sinter-Crystallisation Kinetics of a SiO_2–Al_2O_3–CaO–MgO–SrO Glass-Ceramic Glaze. *Journal of Non-Crystalline Solids* **2020**, 532, 119900. https://doi.org/10.1016/j.jnoncrysol.2020.119900
74. Zhang, F.; Xiong, D.; Xie, J.; Zhang, J.; Han, J.; Chen, D.; Wen, Z.; Fan, Z.; Chen, L.; Sun, T. Effect of Fe_2O_3 on the Structure, Physical Properties and Crystallization of CaO–Al_2O_3–SiO_2 Glass. *Journal of Wuhan University of Technology–Materials Science Edition* **2024**, 39, 954–961. https://doi.org/10.1007/s11595-024-2958-7
75. Tulyaganov, D.U.; Dimitriadis, K.; Agathopoulos, S.; Fernandes, H.R. Glasses and Glass-Ceramics in the CaO–MgO–SiO_2 System: Diopside-Containing Compositions—A Brief Review. *Journal of Non-Crystalline Solids* **2023**, 612, 122351. https://doi.org/10.1016/j.jnoncrysol.2023.122351
76. Lin, Y.; Kim, S.H.; Smith, N.J.; Mauro, J.C. Mixed Modifier Effect in Na_2O·K_2O·CaO Aluminosilicate Glasses: Pairwise and Ternary Interactions. *Journal of the American Ceramic Society* **2023**, 106, 7473–7487. https://doi.org/10.1111/jace.19369
77. Luo, Z.; Zhang, Q.; Guo, J.; Liu, X.; Zhang, M.; Wan, X.; Ye, J.; Liu, L. Effect of Na_2O, MgO, CaO, and Fe_2O_3 on Characteristics of Ceramsite Prepared from Lead–Zinc Tailings and Coal Gangue. *Materials* **2025**, 18, 4928. https://doi.org/10.3390/ma18214928

© 2026 by the author(s). Distributed under a Creative Commons CC BY license.

Preprints.org (www.preprints.org) | NOT PEER-REVIEWED | Posted: 13 April 2026 doi:10.20944/preprints202604.0805.v1

78. Baino, F.; Gianchandani, P.K. Porous Glass for Thermal Insulation in Buildings with a Focus on Sustainable Materials and Technologies: Overview and Challenges. *Ceramics* **2025**, 8, 28. https://doi.org/10.3390/ceramics8010028
79. Wichiensan, N.; Wattanutchariya, W. Sustainable Ceramic Glaze Development from Coal Power Plant Water Treatment Sludge: A Customer-Oriented Approach Using Delphi Method, QFD, and Mixture Design. *Sustainability* **2024**, 16, 8295. https://doi.org/10.3390/su16198295
80. Pasiut, K.; Partyka, J.; Kozień, D.; Kronberg, T. Impact of Barium Oxide on the Structure and Surface Properties of Glass-Crystalline Glazes. *Ceramics International* **2024**, 50, 47980–47990. https://doi.org/10.1016/j.ceramint.2024.09.145
81. Partyka, J.; Pasiut, K.; Kozień, D. The Effect of SrO Addition on the Recrystallization of $ZrSiO_4$ in Raw Glass–Ceramic Glazes from the SiO_2–Al_2O_3–CaO–MgO–K_2O–ZrO_2 System. *Crystals* **2023**, 13, 1435. https://doi.org/10.3390/cryst13101435
82. Carreiro, M.E.A.; da Silva, V.J.; Rodrigues, A.M.; Barbosa, E.P.A.; da Costa, F.P.; Menezes, R.R.; Neves, G.A.; Santana, L.N.L. Firing Parameters Effect on the Physical and Mechanical Properties of Scheelite Tailings-Containing Ceramic Masses. *Sustainability* **2021**, 14, 333. https://doi.org/10.3390/su14010333
83. Wen, L.; Lin, L.; Fan, Y.; Luo, Y.; Ma, S.; Zhou, Y.; Yang, C.; Shih, K.; Li, X. Valorization of Thermally Hydrolyzed Sludge with Clay for Sintering of Ceramic Tiles. *Science of the Total Environment* **2023**, 877, 162871. https://doi.org/10.1016/j.scitotenv.2023.162871
84. Ospanov, K.; Andraka, D.; Kuldeeva, E.; Munussov, I. Utilization of Sewage Sludge in the Sustainable Manufacturing of Ceramic Bricks. *Sustainability* **2025**, 17, 6431. https://doi.org/10.3390/su17146431
85. Defanti, T.J.S.R.B.; Fernandes, R.T.F.; Holanda, J.N.F. Effect of the Firing Temperature on the Technical Properties of Clay Ceramics Added with Blast Furnace Sludge Waste. *Cerâmica* **2025**, 71(Suppl. 1). https://doi.org/10.1590/byys6179
86. Choo, Mohd Salleh; Kok; Matori. A Review on Synthesis of Mullite Ceramics from Industrial Wastes. *Recycling* **2019**, *4*(3), 39. https://doi.org/10.3390/recycling4030039
87. Roy, R.; Das, D.; Rout, P.K. A Review of Advanced Mullite Ceramics. *Engineered Science* **2022**. https://doi.org/10.30919/es8d582
88. Fuertes, V.; Julián Jiménez Reinosa; Fernández, J.F.; Enríquez, E. Engineered Feldspar-Based Ceramics: A Review of Their Potential in Ceramic Industry. *Journal of the European Ceramic Society* **2022**, *42*(2), 307–326. https://doi.org/10.1016/j.jeurceramsoc.2021.10.017
89. Li, X.; Yu, W.; Zhao, B. Effect of Sintering Temperature of Potassium Feldspar–Limestone/Dolomite on Composition and Microstructure of Silicate Fertilizers. *International Journal of Ceramic Engineering & Science* **2019**, *1*(4), 185–193. https://doi.org/10.1002/ces2.10022
90. Gareev, K.G. Diversity of Iron Oxides: Mechanisms of Formation, Physical Properties and Applications. *Magnetochemistry* **2023**, *9*(5), 119. https://doi.org/10.3390/magnetochemistry9050119
91. Pérez-Monserrat, E.; Cultrone, G.; Rincón, J.Ma.; Perla, A.; Fort González, R. Multidisciplinary Study of Glazed Ceramics from Chamberí Metro Station (Madrid, Spain): A Knowledge Base with Technological and Heritage Value. *Applied Clay Science* **2019**, *175*, 102–114. https://doi.org/10.1016/j.clay.2019.03.032
92. Senze, F.; Höhn, S.; Matthey, B.; Schulte-Fischedick, J.; Herrmann, M. Investigation of the Quartz Distribution in Electro-Porcelain Materials. *Ceramics* **2023**, *6*(2), 1277–1290. https://doi.org/10.3390/ceramics6020078
93. Rodríguez, E.A.; Díaz-Tato, L.; López-Perales, J.F.; González-Carranza, Y. Effect of Binary Raw Materials Replacement (Quartz and Feldspar) for Porcelain Chamotte on the Electro-Technical Siliceous Porcelain Properties. *Frontiers in Materials* **2023**, *10*. https://doi.org/10.3389/fmats.2023.1322898
94. Warr, L.N. IMA–CNMNC Approved Mineral Symbols. *Mineralogical Magazine* **2021**, 1–30. https://doi.org/10.1180/mgm.2021.43
95. Whitney, D.L.; Evans, B.W. Abbreviations for Names of Rock-Forming Minerals. *American Mineralogist* **2009**, *95*(1), 185–187. https://doi.org/10.2138/am.2010.3371
96. Toya, T.; Tamura, Y.; Kameshima, Y.; Okada, K. Preparation and Properties of CaO–MgO–Al_2O_3–SiO_2 Glass-Ceramics from Kaolin Clay Refining Waste (Kira) and Dolomite. *Ceramics International* **2004**, *30*(6), 983–989. https://doi.org/10.1016/j.ceramint.2003.11.005

© 2026 by the author(s). Distributed under a Creative Commons CC BY license.

Preprints.org (www.preprints.org) | NOT PEER-REVIEWED | Posted: 13 April 2026 doi:10.20944/preprints202604.0805.v1

97. Cheng, X.; Ke, S.; Wang, Q.; Wang, H.; Shui, A.; Liu, P. Fabrication and Characterization of Anorthite-Based Ceramic Using Mineral Raw Materials. *Ceramics International* **2012**, *38*(4), 3227–3235. https://doi.org/10.1016/j.ceramint.2011.12.028
98. Kuzmickas, L.; Andrade, D.; Szabó, G.A.J.; Motta, M.; Jr, M.C. Influence of Diopside:Feldspar Ratio in Ceramic Reactions Assessed by Quantitative Phase Analysis (X-ray Diffraction – Rietveld Method). *Cerâmica* **2013**, *59*(350), 345–350. https://doi.org/10.1590/s0366-69132013000200022
99. Wang, Y.; Wang, Y.; Zhang, Y.; Chai, Y.; Zhao, F.; Luo, G. Effect of Cr_2O_3 on Crystallization of Diopside Glass–Ceramics. *Crystals* **2022**, *12*(12), 1714. https://doi.org/10.3390/cryst12121714
100. Feng, J.; Wu, D.; Long, M.; Lei, K.; Sun, Y.; Zhao, X. Diopside Glass-Ceramics Fabricated by Sintering Powder Mixtures of Waste Glass and Kaolin. *Ceramics International* **2022**, *48*(18), 27088–27096. https://doi.org/10.1016/j.ceramint.2022.06.020
101. Lamara, S.; Redaoui, D.; Sahnoune, F.; Heraiz, M.; Saheb, N. Formation of Anorthite-Containing Cordierite Materials through Reaction Sintering Kaolin, MgO and CaO Precursors. *Science of Sintering* **2025**, *52*(2), 135–147. https://doiserbia.nb.rs/Article.aspx?id=0350-820X2002135L
102. Gong, W.; Luo, Z.; Liu, Y. Crystallization Kinetic and Dielectric Properties of CaO–MgO–Al_2O_3–SiO_2 Glass/Al_2O_3 Composites. *International Journal of Materials Research* **2022**, *113*(5), 520–528. https://doi.org/10.1515/ijmr-2021-8453
103. Chen, T.; Peng, T.; Sun, H.; Li, X. Effect of SiO_2/Al_2O_3 Ratio on Sintering Behavior, Crystallization Behavior and Properties of Diopside-Anorthite Glass-Ceramics. *Journal of Asian Ceramic Societies* **2023**, *11*(3), 316–329. https://doi.org/10.1080/21870764.2023.2210401
104. Skripnikova, N.; Semenovykh, M.; Shekhovtsov, V. Anorthite-Based Building Ceramics. *DOAJ* **2023**. https://doi.org/10.34910/mce.117.6
105. Omerašević, M.; Pavkov, V.; Rosić, M.; Egerić, M.; Nenadović, S.; Bučevac, D.; Potkonjak, N. Fabrication of Porous Anorthite Ceramic Insulation Using Solid Wastes. *Materials* **2024**, *17*(7), 1478. https://doi.org/10.3390/ma17071478
106. Lin, S.-M.; Yu, Y.-L.; Zhong, M.-F.; Yang, H.; Liu, Y.; Li, H.; Zhang, C.-Y.; Zhang, Z.-J. Preparation of Anorthite/Mullite In Situ and Phase Transformation in Porcelain. *Materials* **2023**, *16*(4), 1616. https://doi.org/10.3390/ma16041616
107. Romero, M.; Padilla, I.; Contreras, M.; López-Delgado, A. Mullite-Based Ceramics from Mining Waste: A Review. *Minerals* **2021**, *11*(3), 332. https://doi.org/10.3390/min11030332
108. Zhao, W.; Huang, X.; Yan, B.; Hu, S.; Guo, H.; Chen, D. Recycling of Blast Furnace Slag and Fluorite Tailings into Diopside-Based Glass-Ceramics with Various Nucleating Agents. *Sustainability* **2021**, *13*(20), 11144. https://doi.org/10.3390/su132011144
109. Skripnikova, N.K.; Volokitin, O.G.; Semenovykh, M.A.; Ushkov, V.A.; Bruyako, M.G.; Zorin, D.A. Anorthite-Containing Ceramics Based on Secondary Materials. *Russian Physics Journal* **2023**, *66*(2), 213–218. https://doi.org/10.1007/s11182-023-02930-3
110. Meng, J.; Zhang, T.; Srinivasakannan, C.; Wei, X.; Duan, X.; Yang, Z.; Liu, F.; Liang, J. Phase Evolution, Microstructure and Properties of Glass-Ceramics Derived from Municipal Solid Waste Incineration Bottom Ash and Molybdenum Tailings. *Ceramics International* **2024**, *50*(22), 45353–45361. https://doi.org/10.1016/j.ceramint.2024.08.375
111. Chen, D.; Zhang, Y.; Xu, Y.; Nie, Q.; Yang, Z.; Sheng, W.; Qian, G. Municipal Solid Waste Incineration Residues Recycled for Typical Construction Materials—A Review. *RSC Advances* **2022**, *12*(10), 6279–6291. https://doi.org/10.1039/d1ra08050d
112. Eminov, Al.A.; Tairov, S.S.; Sabirov, B.T.; Eminov, A.M. Ceramic Body Based on Kaolin–Alumina-Containing Waste–Dolomite System. *Glass and Ceramics* **2024**, *81*(1–2), 62–67. https://doi.org/10.1007/s10717-024-00660-7
113. EL-Rafei, A.M.; Mansour, T.S. Physico-Mechanical and Microstructure Characteristics of Porous Mullite Ceramics. *Silicon* **2023**, *15*(16), 7157–7170. https://doi.org/10.1007/s12633-023-02527-y
114. Ibekwe, I.G.; Aramide, F.O. Development of Mullite–Carbon Refractory Ceramic Composite from Locally Sourced Materials. *International Journal of Engineering Technologies and Management Research* **2023**, *10*(10). https://doi.org/10.29121/ijetmr.v10.i10.2023.1366

© 2026 by the author(s). Distributed under a Creative Commons CC BY license.

Preprints.org (www.preprints.org) | NOT PEER-REVIEWED | Posted: 13 April 2026 doi:10.20944/preprints202604.0805.v1

115. EL-Rafei, A.; Sami, T. Recycling of Waste of Alum Industry in Manufacturing of Porous Mullite: Microstructure and Physico-Mechanical Properties. *Egyptian Journal of Chemistry* **2024**, *0*(0). https://doi.org/10.21608/ejchem.2024.326070.10580
116. López, P.V.; Hernández, M.F.; Richard, D.; Conconi, M.S.; Rendtorff, N.M. Porous Acicular Mullite Ceramics Produced from Well and Poorly Crystallized Kaolinite. *Applied Clay Science* **2023**, *238*, 106937. https://doi.org/10.1016/j.clay.2023.106937
117. Zhang, Y.; Liu, H.; Chen, X. Effect of mineral additives on water absorption and microstructural evolution of clay-based ceramics. *Ceram. Int.* **2023**, *49*(2), 2451–2462. https://doi.org/10.1016/j.ceramint.2022.09.118
118. García-Ten, J.; Saburit, A.; Monzó, M. Water absorption and pore structure modification in ceramic bodies incorporating industrial waste additives. *J. Eur. Ceram. Soc.* **2024**, *44*(5), 2103–2115. https://doi.org/10.1016/j.jeurceramsoc.2023.11.004
119. Kumar, R.; Singh, P.; Patel, S. Influence of silica-rich and organic additives on porosity, water uptake, and thermal behavior of structural ceramics. *Appl. Clay Sci.* **2022**, *228*, 106679. https://doi.org/10.1016/j.clay.2022.106679
120. Niú, M.; Ge, X.; Dai, Y.; Jin, X.; Sun, W.; Hu, X. Effects of sintering parameters on the preparation and properties of foamed ceramics from cyanide tailings. *J. Asian Ceram. Soc.* **2024**, *12*(2), 151–163. https://doi.org/10.1080/21870764.2024.2325747
121. Yang, B.; Lu, S.; Li, C.; Fang, C.; Wan, Y.; Lin, Y. Reducing water absorption and improving flexural strength of aluminosilicate ceramics by MnO_2 doping. *Materials* **2024**, *17*(11), 2557. https://doi.org/10.3390/ma17112557
122. Duarte, T.P.; Alves, J.L.; Pereira, P. Study of the influence of sintering temperature on water absorption in the manufacture of porcelain cups. In *Materials Design and Applications II*; Springer: Cham, Switzerland, **2018**; pp. 129–147. https://doi.org/10.1007/978-3-030-02257-0_11
123. Sáez-Pérez, M.P.; Durán-Suárez, J.A.; Martínez-Ramírez, A. New ceramic materials with mining additives: A strategy towards a circular economy in the construction industry. In *Proceedings of CIRMARE 2025*; Springer: Cham, Switzerland, **2025**; pp. 335–346.
124. Rajpoot, S.; Kang, E.S.; Kim, Y.-W. Processing and properties of water absorbing zeolite-based porous ceramics. *J. Korean Ceram. Soc.* **2022**, *59*, 94–103. https://doi.org/10.1007/s43207-021-00160-2
125. Ding, D.; Guan, Y.; Xiao, G.; Mao, Z.; Shi, X.; Gao, K.; Chong, X.; Luo, J.; Lei, C. Effects of sintering temperature on microstructure and mechanical properties of pressureless sintering alumina ceramics with Al_2O_3–SiO_2–CaO sintering aids. *Refract. Ind. Ceram.* **2023**, *64*, 136–146. https://doi.org/10.1007/s11148-023-00816
126. Jalaluddin, M.L.; Azlan, U.A.; Abd Rashid, M.W.; Tamin, N. Effect of sintering temperatures on the physical, structural properties and microstructure of mullite-based ceramics. *AIMS Mater. Sci.* **2024**, *11*(2), 243–255. https://doi.org/10.3934/matersci.2024014
127. Colomer, M.T. Design, synthesis and applications of macroporous, mesoporous, and microporous materials. *Int. J. Mol. Sci.* **2024**, *25*(13), 7127. https://doi.org/10.3390/ijms25137127
128. Liu, D.; Zhang, H.; Chen, G.; You, X.; Jia, J. Effects of pore microstructures on thermal and mechanical properties of porous TiC fabricated by hot press sintering. *J. Porous Mater.* **2024**, *31*, 1351–1361. https://doi.org/10.1007/s10934-024-01600-0
129. Kuanyshbay, A.; Niyetbay, S.; Tashmukhanbetova, I.; Sadyrov, R.; Amangeldi, N.; Mustafa, L.; Nurakhova, A.; Rustemov, I.; Yesbolat, A. Optimized development of high-porosity structural and thermal insulation foam ceramics based on local natural and technogenic raw materials. *Ceramics* **2025**, *8*(2), 35. https://doi.org/10.3390/ceramics8020035
130. Zuo, Z.; Mu, M.; Liu, X.; Jiang, C. The effect of flux on a waste-derived foamed ceramic: Analysis of microstructure and properties. *Crystals* **2024**, *14*(8), 682. https://doi.org/10.3390/cryst14080682
131. Eminov, A.M.; Boyzhanov, I.R.; Allamov, R.G. Gurlan hydromicaceous clay—Low temperature flux in ceramic production. *Glass Ceram.* **2023**, *79*, 518–521. https://doi.org/10.1007/s10717-023-00543-3
132. Defanti, T.J.S.R.B.; Faria Jr, R.T.; Holanda, J.N.F. Effect of the firing temperature on the technical properties of clay ceramic added with blast furnace sludge waste. *Cerâmica* **2025**, *71*(Suppl. 1), eBYYS6179. https://doi.org/10.1590/BYYS6179

© 2026 by the author(s). Distributed under a Creative Commons CC BY license.

Preprints.org (www.preprints.org) | NOT PEER-REVIEWED | Posted: 13 April 2026 doi:10.20944/preprints202604.0805.v1

133. Abouloifa, W.; Ettaki, M.; Mounir, S.H. Impact of firing temperature on energy efficiency, durability, and performance in clay brick manufacturing with diverse clay types. In *Technical and Technological Solutions Towards a Sustainable Society and Circular Economy*; Springer: Cham, Switzerland, **2024**; pp. 105–116. https://doi.org/10.1007/978-3-031-56292-1_8
134. Rakcho, Y.; Mouiya, M.; Abouliatim, Y.; Bouazizi, A.; Sehaqui, H.; Mansouri, S.; Benhammou, A.; Hannache, H.; Alami, J.; Abourriche, A. Effect of firing temperature on porous ceramic properties fabricated by Moroccan red clay and oil shale. *Mater. Today Proc.* **2024**. https://doi.org/10.1016/j.matpr.2024.01.022
135. Luo, Z.; Zhang, Q.; Guo, J.; Liu, X.; Zhang, M.; Wan, X.; Ye, J.; Liu, L. Effect of Na_2O, MgO, CaO, and Fe_2O_3 on characteristics of ceramsite prepared from lead–zinc tailings and coal gangue. *Materials* **2025**, *18*(21), 4928. https://doi.org/10.3390/ma18214928
136. Bohara, N.B.; Ghale, D.B.; Chapagain, Y.P.; Duwal, N.; Bhattarai, J. Effect of firing temperature on physico mechanical properties of contemporary clay brick productions in Lalitpur, Nepal. *Bangladesh J. Sci. Ind. Res.* **2020**, *55*(1), 43–52. https://doi.org/10.3329/bjsir.v55i1.46731
137. Paiva, H.; Simões, F.; Maljaee, H.; Yliniemi, J.; Illikainen, M.; Ferreira, V.M. Production of ceramic construction materials as an environmental management solution for sulfidic mine tailings. *SN Appl. Sci.* **2021**, *3*, 751. https://doi.org/10.1007/s42452-021-04735-w
138. Oke, J.A.; Abuel-Naga, H. Durability Assessment of Eco-Friendly Bricks Containing Lime Kiln Dust and Tire Rubber Waste Using Mercury Intrusion Porosimetry. *Applied Sciences* **2024**, *14*, 5131. https://doi.org/10.3390/app14125131
139. Cardoso, R.; Silva, R.V.; Brito, J. de; Dhir, R. Use of recycled aggregates from construction and demolition waste in geotechnical applications: A literature review. *Waste Management* **2016**, *49*, 131–145. https://doi.org/10.1016/j.wasman.2015.12.021
140. Cobîrzan, N.; Thalmaier, G.; Balog, A.-A.; Constantinescu, H.; Timiş, I.; Streza, M. Thermophysical properties of fired clay bricks with waste ceramics and paper pulp as pore-forming agent. *Journal of Thermal Analysis and Calorimetry* **2018**, *134*, 843–851. https://doi.org/10.1007/s10973-018-7092-3
141. Johari, I.; Said, S.; Hisham, B.; Bakar, A.; Ahmad, Z.A. Effect of the change of firing temperature on microstructure and physical properties of clay bricks from Beruas (Malaysia). *Science of Sintering* **2010**, *42*, 245–254. https://doi.org/10.2298/sos1002245j
142. Terrones-Saeta, J.M.; Suárez-Macías, J.; Bernardo-Sánchez, A.; Álvarez de Prado, L.; Menéndez Fernández, M.; Corpas-Iglesias, F.A. Treatment of Soil Contaminated by Mining Activities to Prevent Contamination by Encapsulation in Ceramic Construction Materials. *Materials* **2021**, *14*, 6740. https://doi.org/10.3390/ma14226740
143. Xiao, H.; Guo, Z.; Huo, Y.; Zhang, X.; Li, Y. Characterization and solidification of heavy metals in sintered solid-waste ceramics made from zinc-extraction kiln slag. *Environmental Science and Pollution Research* **2024**, *31*, 66235–66247. https://doi.org/10.1007/s11356-024-35686-5
144. Ayoub Imgirne; Arkame, Y.; Harrati, A.; Moustapha, A.; Tamri, T.; Hassani, F.O.; El Haddar, A.; Ait Hmeid, H.; Sdiri, A.; Sadik, C. Potential use of mint waste and bentonite clay in sustainable porous ceramic manufacturing. *Euro-Mediterranean Journal for Environmental Integration* **2025**. https://doi.org/10.1007/s41207-024-00716-8
145. Fu, S.; Liu, R.; Wei, J.; Lv, W.; Zhang, C.; Ouyang, Z. Effect of holding time on the properties of porous ceramics with high-volume polished slag and its pore structure characteristics. *Frontiers in Materials* **2023**, *10*, 1147120. https://doi.org/10.3389/fmats.2023.1147120
146. Fu, H. Characterisation of coal gangue and fabrication of porous ceramic materials. *Ceramics-Silikáty* **2024**, *68*, 80–87. https://doi.org/10.13168/cs.2024.0007
147. Zuo, Z.; Mu, M.; Liu, X.; Jiang, C. The Effect of Flux on a Waste-Derived Foamed Ceramic: Analysis of Microstructure and Properties. *Crystals* **2024**, *14*, 682. https://doi.org/10.3390/cryst14080682
148. Jiang, Q.; Chen, M.; Guo, W.; Hu, X.; Zhou, W.; Zhao, F.; Xie, L.; Yang, H. Investigating the Effect of the Particle Size of Potter's Clay on the Pore Structure of Pottery. *JOM* **2025**, *77*, 6454–6466. https://doi.org/10.1007/s11837-025-07540-7

© 2026 by the author(s). Distributed under a Creative Commons CC BY license.

Preprints.org (www.preprints.org) | NOT PEER-REVIEWED | Posted: 13 April 2026 doi:10.20944/preprints202604.0805.v1

149. Umut Önen; Boyraz, T. Correlation between bending strength and porosity in vermiculite added ceramic bodies. *Journal of Ceramic Processing Research* **2024**, *25*, 624–632. https://doi.org/10.36410/jcpr.2024.25.4.624
150. Krautkrämer, J.; Krautkrämer, H. Metallic Materials and Their Specific Problems for Ultrasonic Testing. *Ultrasonic Testing of Materials* **1990**, 497–513. https://doi.org/10.1007/978-3-662-10680-8_32
151. Satapathy, S.; Mishra, M.; Das, M. R. Use of Mining Waste as Ceramics and Testing for Their Properties. *SpringerBriefs in Earth System Sciences* **2024**, 41–50. https://doi.org/10.1007/978-3-031-67932-2_6
152. Han, Z.; Golev, A.; Edraki, M. A Review of Tungsten Resources and Potential Extraction from Mine Waste. *Minerals* **2021**, 11, 701. https://doi.org/10.3390/min11070701
153. Özkan, İ.; Yayla, Z. Evaluation of Correlation between Physical Properties and Ultrasonic Pulse Velocity of Fired Clay Samples. *Ultrasonics* **2016**, 66, 4–10. https://doi.org/10.1016/j.ultras.2015.12.008
154. Erasmus, E. The Influence of Thermal Treatment on Properties of Kaolin. *Hemijska Industrija* **2015**, 70, 595–601. https://doi.org/10.2298/hemind150720066e
155. Figueirêdo, J. M. R. de; Costa, F. P. da; Fernandes, J. V.; Rodrigues, A. M.; Neves, G. de A.; Menezes, R. R.; Santana, L. N. de L. Development of Scheelite Tailings-Based Ceramic Formulations with the Potential to Manufacture Porcelain Tiles, Semi-Stoneware and Stoneware. *Materials* **2020**, 13, 5122. https://doi.org/10.3390/ma13225122
156. Carreiro, M. E. A.; da Silva, V. J.; Rodrigues, A. M.; Barbosa, E. P. de A.; da Costa, F. P.; Menezes, R. R.; Neves, G. A.; Santana, L. N. de L. Firing Parameters Effect on the Physical and Mechanical Properties of Scheelite Tailings-Containing Ceramic Masses. *Sustainability* **2021**, 14, 333. https://doi.org/10.3390/su14010333
157. Azam, R.; Riaz, M. R.; Haq, E. U.; Shihata, A.; Zawam, M. Development of Quality Assessment Criteria for Burnt Clay Bricks of Different Ages Based on Ultrasonic Pulse Velocity Test. *Buildings* **2022**, 12, 1069. https://doi.org/10.3390/buildings12081069
158. Almeida, E. P.; Carreiro, M. E. A.; Rodrigues, A. M.; Ferreira, H. S.; Santana, L. N. L.; Menezes, R. R.; Neves, G. A. A New Eco-Friendly Mass Formulation Based on Industrial Mining Residues for the Manufacture of Ceramic Tiles. *Ceramics International* **2021**, 47, 11340–11348. https://doi.org/10.1016/j.ceramint.2020.12.260
159. Anjum, F.; Ghaffar, A.; Jamil, Y.; Majeed, M. I. Effect of Sintering Temperature on Mechanical and Thermophysical Properties of Biowaste-Added Fired Clay Bricks. Journal of Material Cycles and Waste Management **2018**, 21, 503–524. https://doi.org/10.1007/s10163-018-0810-x
160. Flores Nicolás, M.; Chávez Cano, M. M.; Vlasova, M.; Pi Puig, T. Low-Temperature Sintering of Ceramic Bricks from Clay, Waste Glass and Sand. Boletín de La Sociedad Española de Cerámica y Vidrio **2024**. https://doi.org/10.1016/j.bsecv.2024.06.003
161. Almuqrin, A. H.; Mahmoud, K. A.; Sayyed, M. I.; Al-Ghamdi, H. Impacts of Sintering Temperature on the Mechanical Properties and Gamma Ray Protection Capacity of Clay Bricks. Nuclear Engineering and Technology **2024**, 56, 2489–2497. https://doi.org/10.1016/j.net.2024.02.007
162. Baygan, G. D.; Abellana, V. Mechanical Properties of Fireclay Bricks from Binaliw Clay. Asian Review of Mechanical Engineering **2022**, 11, 16–19. https://doi.org/10.51983/arme-2022.11.2.3581
163. Elias, M. L.; Cultrone, G. On the Use of Sodium Chloride and Calcined Diatomite Sludge as Additives to Improve the Engineering Properties of Bricks Made with a Clay Earth from Jun (Granada, Spain). Minerals **2019**, 9, 64. https://doi.org/10.3390/min9010064
164. Goltsman, B. M.; Yatsenko, E. A.; Smoliy, V. A.; Yatsenko, V. S.; Timofeeva, A. A. *Study of Structural Changes During Firing of Clays with Flux Additives. Lecture Notes in Civil Engineering* **2025**, 540–549. https://doi.org/10.1007/978-3-031-80482-3_51
165. Ngayakamo, B.; Komadja, G. C.; Bello, A.; Onwualu, A. P. Valorization of Granite Micronized Stones Wastes for Eco-Friendly Production of Fired Clay Bricks. SN Applied Sciences **2021**, 3. https://doi.org/10.1007/s42452-021-04828-6
166. Tabak, Y. The Utilization of Wet Silica Sand Sludge as an Additive in Different Temperature Sustainable Brick Production. Buildings **2025**, 15, 849. https://doi.org/10.3390/buildings15060849
167. Moustapha, A.; Arkame, Y.; Imgirne, A.; Manni, A.; Tamri, T.; Harrati, A.; Hassani, F. O.; Laasri, L.; Sadik, C. Enhancing Sintering of Kaolinitic Clay from DRC Using Cassava Waste Ash: A Novel Aid for

© 2026 by the author(s). Distributed under a Creative Commons CC BY license.

Preprints.org (www.preprints.org) | NOT PEER-REVIEWED | Posted: 13 April 2026 doi:10.20944/preprints202604.0805.v1

Optimizing Ceramic Performance. Next Materials **2025**, 8, 100882. https://doi.org/10.1016/j.nxmate.2025.100882

168. Makni, H.; Becquart, F.; Khlif, M.; Abriak, N.-E.; Bradai, C. *Multiphysics Properties of Fired Clay Bricks Incorporating Deinking Paper Sludge. Springer Proceedings in Materials* **2024**, 261–269. https://doi.org/10.1007/978-981-97-2000-2_30
169. Cobîrzan, N.; Thalmaier, G.; Balog, A.-A.; Constantinescu, H.; Timiş, I.; Streza, M. Thermophysical Properties of Fired Clay Bricks with Waste Ceramics and Paper Pulp as Pore-Forming Agent. Journal of Thermal Analysis and Calorimetry **2018**, 134, 843–851. https://doi.org/10.1007/s10973-018-7092-3
170. Cultrone, G.; Sebastián, E.; de la Torre, M. J. *Mineralogical and Physical Behaviour of Solid Bricks with Additives. Construction and Building Materials* **2005**, 19, 39–48. https://doi.org/10.1016/j.conbuildmat.2004.04.035
171. Akpomie, K. G.; Alhadji Malloum; Akpotu, S. O.; Adegoke, K. A.; Olisah, C. Effect of Biomass-Based Additives on the Thermal, Physical, and Mechanical Properties of Fired Clay Bricks: A Review. International Journal of Thermophysics **2024**, 46. https://doi.org/10.1007/s10765-024-03476-3
172. Khan, A.; Ali, A.; Khattak, M. J.; Hume, L. A.; Pesacreta, T. C. *Development of Sustainable High-Strength Fired Clay Bricks Using Rice Husk Ash. Sustainability* **2026**, 18, 2199. https://doi.org/10.3390/su18052199
173. Achik, M.; Benmoussa, H.; Oulmekki, A.; Ijjaali, M.; El Moudden, N.; Kizinievic, O.; Kizinievic, V. Evaluation of Physical and Mechanical Properties of Fired-Clay Bricks Incorporating Both Mineral and Organic Wastes. Vilniustech Repository **2019**. https://etalpykla.vilniustech.lt/handle/123456789/156033
174. Bilgil, A.; Şimşek, O.; Sevim, Ö.; Demir, İ. Development of Lightweight and Thermally Efficient Clay Bricks Using Expansion Additives: Effects of Firing Temperature and Additive Ratios on Physicomechanical Properties. Journal of the Australian Ceramic Society **2025**. https://doi.org/10.1007/s41779-025-01170-7
175. Bidoung, J. C.; Mpoung, L. A.; Mbey, J. A.; Meva'a, J. R. L. Experimental and Numerical Study of Mechanical Behaviour of Fired Clay Bricks after Exposure to High Temperatures. Journal of Minerals and Materials Characterization and Engineering **2023**, 11, 143–160. https://doi.org/10.4236/jmmce.2023.115012
176. AENOR. UNE 67019:1996 EX. Ladrillos Cerámicos de Arcilla Cocida. Definiciones, Clasificaciones y Especificaciones. Asociación Española de Normalización, **1996**.
177. AENOR. UNE-EN 1996-1-1:2013. Eurocódigo 6: Proyecto de Estructuras de Fábrica. Parte 1-1: Reglas Generales para Edificios. Asociación Española de Normalización, **2013**.
178. Solismaa, S.; Ismailov, A.; Karhu, M.; Sreenivasan, H.; Lehtonen, M.; Kinnunen, P.; Illikainen, M.; Räisänen, M. L. Valorization of Finnish mining tailings for use in the ceramics industry. *Bulletin of the Geological Society of Finland* **2018**, 90(1), 33–54. https://doi.org/10.17741/bgsf/90.1.002
179. Liu, J.; Ou, Y.; Xu, C.; Qi, H. Effect of heat treatment method on microstructure of tailings glass ceramics. *Journal of Wuhan University of Technology-Mater. Sci. Ed.* **2008**, 23(6), 883–888. https://doi.org/10.1007/s11595-008-6883-y
180. Loutou, M.; Hakkou, R.; Argane, R.; Mansori, M.; Grase, L.; Svinka, R.; Mezinskis, G. Clayey quarry sludges: Thermal transformation, microstructure and technological properties. *Waste and Biomass Valorization* **2017**, 9(10), 1805–1815. https://doi.org/10.1007/s12649-017-9972-3
181. Conte, S.; Molinari, C.; Ardit, M.; Cruciani, G.; Dondi, M.; Zanelli, C. Porcelain versus porcelain stoneware: So close, so different. Sintering kinetics, phase evolution, and vitrification paths. *Materials* **2022**, 16(1), 171. https://doi.org/10.3390/ma16010171
182. Jannetto, P.J.; Cowl, C.T. Elementary Overview of Heavy Metals. *Clinical Chemistry* **2023**. https://doi.org/10.1093/clinchem/hvad022
183. Ávila, P.F.; Silva, E.F. da; Salgueiro, A.R.; Farinha, J.A. Geochemistry and Mineralogy of Mill Tailings Impoundments from the Panasqueira Mine (Portugal): Implications for the Surrounding Environment. *Mine Water and the Environment* **2008**, *27*(4). https://doi.org/10.1007/s10230-008-0046-4
184. Candeias, C.; Melo, R.; Ávila, P.F.; Ferreira da Silva, E.; Salgueiro, A.R.; Teixeira, J.P. Heavy Metal Pollution in Mine–Soil–Plant System in S. Francisco de Assis – Panasqueira Mine (Portugal). *Applied Geochemistry* **2014**, *44*, 12–26. https://doi.org/10.1016/j.apgeochem.2013.07.009
185. Suppes, R.; Heuss-Aßbichler, S. Resource Potential of Mine Wastes: A Conventional and Sustainable Perspective on a Case Study Tailings Mining Project. *Journal of Cleaner Production* **2021**, *297*, 126446. https://doi.org/10.1016/j.jclepro.2021.126446

© 2026 by the author(s). Distributed under a Creative Commons CC BY license.

Preprints.org (www.preprints.org) | NOT PEER-REVIEWED | Posted: 13 April 2026 doi:10.20944/preprints202604.0805.v1

186. Abd Elnabi, M.K.; Elkaliny, N.E.; Elyazied, M.M.; Azab, S.H.; Elkhalifa, S.A.; Elmasry, S.; Mouhamed, M.S.; Shalamesh, E.M.; Alhorieny, N.A.; Abd Elaty, A.E.; Elgendy, I.M.; Etman, A.E.; Saad, K.E.; Tsigkou, K.; Ali, S.S.; Kornaros, M.; Mahmoud, Y.A.-G. Toxicity of Heavy Metals and Recent Advances in Their Removal: A Review. *Toxics* **2023**, *11*(7), 580. https://doi.org/10.3390/toxics11070580
187. Bonglaisin, J.N.; Kunsoan, N.B.; Bonny, P.; Matchawe, C.; Tata, B.N.; Nkeunen, G.; Mbofung, C.M. Geophagia: Benefits and Potential Toxicity to Humans—A Review. *Frontiers in Public Health* **2022**, *10*. https://doi.org/10.3389/fpubh.2022.893831
188. Jomova, K.; Alomar, S.Y.; Nepovimova, E.; Kuca, K.; Valko, M. Heavy Metals: Toxicity and Human Health Effects. *Archives of Toxicology* **2024**, *99*(1). https://doi.org/10.1007/s00204-024-03903-2
189. Zhao, D.; Wang, P.; Zhao, F.-J. Toxic Metals and Metalloids in Food: Current Status, Health Risks, and Mitigation Strategies. *Current Environmental Health Reports* **2024**. https://doi.org/10.1007/s40572-024-00462-7
190. Karius, V.; Hamer, K. pH and Grain-Size Variation in Leaching Tests with Bricks Made of Harbour Sediments Compared to Commercial Bricks. *Science of the Total Environment* **2001**, *278*(1–3), 73–85. https://doi.org/10.1016/s0048-9697(00)00889-5
191. Qu, F.; Zheng, W. Cadmium Exposure: Mechanisms and Pathways of Toxicity and Implications for Human Health. *Toxics* **2024**, *12*(6), 388. https://doi.org/10.3390/toxics12060388
192. Rose, A.W.; Hawks, H.E.; Webb, J.H. *Geochemistry in Mineral Exploration*, 2nd ed.; Academic Press: London, UK, **1979**.
193. Belmonte, A.P.; Ottosen, L.M.; Kirkelund, G.M.; Jensen, P.E.; Vestbø, A.P. Screening of Heavy-Metal-Containing Waste Types for Use as Raw Material in Arctic Clay-Based Bricks. *Environmental Science and Pollution Research* **2018**, *25*(33), 32831–32843. https://doi.org/10.1007/s11356-016-8040-z
194. CIE. *Colorimetry—Part 4: CIE 1976 L*a*b* Colour Space.* **n.d.** Available online: https://cie.co.at/publications/colorimetry-part-4-cie-1976-lab-colour-space-0
195. Gareev, K.G. *Diversity of Iron Oxides: Mechanisms of Formation, Physical Properties and Applications.* Magnetochemistry **2023**, 9, 119. https://doi.org/10.3390/magnetochemistry9050119
196. Touzi, N.; Horchani-Naifer, K. *A Study on the Preparation and Characterization of Pigment Quality from Mill Scale Steel Wastes.* Environ. Sci. Pollut. Res. **2023**. https://doi.org/10.1007/s11356-023-25594-5
197. Chen, H.; Liu, Y.; Zhang, H.; Zhao, S.; Nemsak, S.; Liu, H.; Salmeron, M. *Resolving the Valence of Iron Oxides by Resonant Photoemission Spectroscopy.* arXiv **2024**, arXiv:2409.15649. https://arxiv.org/abs/2409.15649
198. Nurdini, N.; Ilmi, M.M.; Maryanti, E.; Setiawan, P.; Kadja, G.T.M.; Ismunandar. *Thermally-Induced Color Transformation of Hematite: Insight into the Prehistoric Natural Pigment Preparation.* Heliyon **2022**, 8, e10377. https://doi.org/10.1016/j.heliyon.2022.e10377
199. Rzepa, G.; Bajda, T.; Gaweł, A.; Debiec, K.; Drewniak, L. *Mineral Transformations and Textural Evolution during Roasting of Bog Iron Ores.* J. Therm. Anal. Calorim. **2015**, 123, 615–630. https://doi.org/10.1007/s10973-015-4925-1
200. Elert, K.; Monasterio-Guillot, L.; Cultrone, G. Effect of Iron and Organic Matter on Mineralogy and Texture of Replacement Bricks for Heritage Conservation: The Alhambra Formation Soil (Granada, Spain). J. Eur. Ceram. Soc. **2024**, 44, 4294–4306. https://doi.org/10.1016/j.jeurceramsoc.2024.01.062
201. Di Febo, R.; Molera, J.; Pradell, T.; Vallcorba, O.; Capelli, C. *Technological Implications of Neo-Formed Hematite Crystals in Ceramic Lead Glazes.* Sci. Technol. Archaeol. Res. **2017**, 3, 366–375. https://doi.org/10.1080/20548923.2017.1419675
202. Danish, A.; Totiç, E.; Bayram, M.; Sütçü, M.; Gencel, O.; Erdoğmuş, E.; Ozbakkaloglu, T. Assessment of Mineralogical Characteristics of Clays and the Effect of Waste Materials on Their Index Properties for the Production of Bricks. Materials **2022**, 15, 8908. https://doi.org/10.3390/ma15248908
203. Assunção, A.R.S.; Correia, G.S.; Vasconcelos, N.S.L.S.; Cabral, A.A.; Angélica, R.S.; Costa, F.P.; Menezes, R.R.; Araújo Neves, G.; Rodrigues, A.M.; Rivas-Mercury, J.M. *New Clayey Deposit and Their Potential as Raw Material for Red or Structured Ceramics: Technological Characterization.* Materials **2021**, 14, 7672. https://doi.org/10.3390/ma14247672

© 2026 by the author(s). Distributed under a Creative Commons CC BY license.

Preprints.org (www.preprints.org) | NOT PEER-REVIEWED | Posted: 13 April 2026 doi:10.20944/preprints202604.0805.v1

204. Sharma, G.; Wu, W.; Dalal, E.N. The CIEDE2000 Color-Difference Formula: Implementation Notes, Supplementary Test Data, and Mathematical Observations. Color Res. Appl. **2004**, 30, 21–30. https://doi.org/10.1002/col.20070
205. Ruyter, I.E.; Nilner, K.; Möller, B. *Color Stability of Dental Composite Resin Materials for Crown and Bridge Veneers.* Dent. Mater. **1987**, 3, 246–251. https://doi.org/10.1016/S0109-5641(87)80081-7
206. Douglas, R.D.; Brewer, J.D. *Variability of Porcelain Color Reproduction by Commercial Laboratories.* J. Prosthet. Dent. **2003**, 90, 339–346. https://doi.org/10.1016/S0022-3913(03)00513-4
207. Manni, M.; Landi, F.F.A.; Giannoni, T.; Petrozzi, A.; Nicolini, A.; Cotana, F. *A Comparative Study on Opto-Thermal Properties of Natural Clay Bricks Incorporating Dredged Sediments.* Energies **2021**, 14, 4575. https://doi.org/10.3390/en14154575
208. Pérez-Monserrat, E.; Maritan, L.; Garbin, E.; Cultrone, G. *Production Technologies of Ancient Bricks from Padua, Italy: Changing Colors and Resistance over Time.* Minerals **2021**, 11, 744. https://doi.org/10.3390/min11070744
209. Al-Khazraji, K.; Sleibi, A. Analysis of Colour Differences Obtained by Acceptability and Perceptibility Threshold (Visual Method): Review. Mustansiria Dent. J. **2023**, 19, 280–289. https://doi.org/10.32828/mdj.v19i2.900
210. Dehon, C.; Halim, M.E.; Fagel, N.; Daoudi, L.; Cools, C.; Rousseau, V.; El Ouahabi, M. *Restoration of Decorative Glazed Ceramic from Morocco: Technical Replicas.* CeROArt **2024**, 13. https://doi.org/10.4000/12ldb
211. Carangi, M.C.; Corti, C.; Rampazzi, L. Looking at the Modern to Better Understand the Ancient: Differentiating Mars Pigments from Archaeological Ochres. Heritage **2024**, 7, 6192–6212. https://doi.org/10.3390/heritage7110291
212. Madariaga, I.; Lama, E.; Calparsoro, E.; Prieto-Taboada, N.; Arana, G.; Rodríguez Laso, M.D.; Madariaga, J.M. *Enhancement and Recovery of Tiles Affected by Atmospheric Pollutants in the Galleries of Punta Begoña, Getxo (Bizkaia).* Bol. Soc. Esp. Ceram. Vidr. **2018**, 58, 161–170. https://doi.org/10.1016/j.bsecv.2018.11.001
213. Martínez-Moya, J.A.; Gual-Ortí, J. *Graphic Restitution and Recovery of the Chronos Pavement of the Marquis of Benicarló's House.* Heritage **2024**, 7, 4206–4226. https://doi.org/10.3390/heritage7080198
214. Genua, F.; Lancellotti, I.; Leonelli, C. Geopolymer-Based Stabilization of Heavy Metals, the Role of Chemical Agents in Encapsulation and Adsorption: Review. **2025**, Polymers, 17(5), 670–670. https://doi.org/10.3390/polym17050670
215. Wang, Z.; Chen, H. J.; Pei, L. Z.; Guo, X. Y.; Fan, C. G. Preparation and characterisation of environmental-friendly ceramsites from iron ore tailings and sludge. **2020**, International Journal of Sustainable Engineering, 14(4), 884–892. https://doi.org/10.1080/19397038.2020.1737753
216. Amir Detho, K.; Kadir, A. A.; Shayuti, A.; Rahim, B. A.; Nejib Ghazouani; Mabrouk, A.; Elhag, A. B.; Hesham Hussein Rassem. *Improvement of engineering properties and environmental impact of fired clay bricks utilizing industry sludge waste*. **2025**, *Scientific Reports*, 15(1). https://doi.org/10.1038/s41598-025-89147-1
217. Roshchupkina, I. Yu.; Abdrakhimova, E. S.; Abdrakhimov, V. Z. Phase Composition of Ceramic Materials Based on Waste of the Fuel and Energy Complex. **2023**, Theoretical Foundations of Chemical Engineering, 57(5), 1141–1148. https://doi.org/10.1134/s0040579523050287
218. Omerašević, M.; Pavkov, V.; Milena Rosić; Marija Egerić; Snežana Nenadović; Dušan Bučevac; Nebojša Potkonjak. *Fabrication of Porous Anorthite Ceramic Insulation Using Solid Wastes*. **2024**, *Materials*, 17(7), 1478–1478. https://doi.org/10.3390/ma17071478
219. Guo, C.; Kong, J.; Wang, Z.; Meng, X.; Zhao, Y.; Wu, W.; Quan, H. *Study on Preparation and Properties of Sintered Brick from Multi-Source Solid Waste*. **2022**, *Applied Sciences*, 12(19), 10181–10181. https://doi.org/10.3390/app121910181
220. Bao, P.; Jing, J.; Qi, Y.; Ma, J.; Ping, H.; Wang, C.; Liu, Z.; Zheng, Y.; Zhai, Y.; Liu, F. Firing mechanism and benefit evaluation of high-strength fired water permeable brick containing vanadium-titanium iron ore tailings. **2023**, Frontiers in Earth Science, 11. https://doi.org/10.3389/feart.2023.1214184
221. Tong, Z.; Xie, Z.; Hua, P.; Zeng, Q.; Zhang, S.; Li, X. Study on the high-temperature resistance of tungsten tailings-based alkali-activated materials by pressure forming. **2024**, International Journal of Applied Ceramic Technology, 21(6), 4280–4292. https://doi.org/10.1111/ijac.14851

© 2026 by the author(s). Distributed under a Creative Commons CC BY license.

Preprints.org (www.preprints.org) | NOT PEER-REVIEWED | Posted: 13 April 2026 doi:10.20944/preprints202604.0805.v1

222. Jamshidi, A.; Sousa, L. Strength Characteristics, Ultrasonic Wave Velocity, and the Correlation between Them in Clay Bricks under Dry and Saturated Conditions. **2024**, Materials, 17(6), 1353–1353. https://doi.org/10.3390/ma17061353
223. Cabané, A.; Seneschal, T.; Roca, P.; Pelà, L. Non-destructive evaluation of solid fired clay brick strength using the SonReb method. **2025**, Construction and Building Materials, 485, 141919. https://doi.org/10.1016/j.conbuildmat.2025.141919
224. Aslam, M.; Choi, Y.; Lee, J. Enhancing structural integrity of refractories during manufacturing through integration of UPV and acoustic nonlinearity measurements. **2024**, Nondestructive Testing and Evaluation, 40(6), 2645–2669. https://doi.org/10.1080/10589759.2024.2385073
225. Kaur, D. P.; Raj, S.; Tipu, R. K.; Gupta, S.; Sorout, J.; Lamba, P. Optimizing brick manufacturing: integrating ceramic waste and predictive analytics for sustainable production. **2025**, Journal of Material Cycles and Waste Management, 28(1), 612–636. https://doi.org/10.1007/s10163-025-02443-w
226. Zhou, W.; Du, H.; Kang, L.; Du, X.; Shi, Y.; Qiang, X.; Li, H.; Zhao, J. *Microstructure Evolution and Improved Permeability of Ceramic Waste-Based Bricks*. **2022**, *Materials*, 15(3), 1130. https://doi.org/10.3390/ma15031130
227. Liu, H.-D.; Fan, L. Optimization and mechanism analysis of a compound additive for unfired bricks made of construction and demolition wastes. **2024**, Frontiers in Materials, 11. https://doi.org/10.3389/fmats.2024.1308884
228. Ding, D.; Guan, Y.; Xiao, G.; Mao, Z.; Shi, X.; Gao, K.; Chong, X.; Luo, J.; Lei, C. Effects of Sintering Temperature on Microstructure and Mechanical Properties of Pressureless Sintering Alumina Ceramics with Al_2O_3–SiO_2–CaO Sintering Aids. **2023**, Refractories and Industrial Ceramics, 64(2), 136–146. https://doi.org/10.1007/s11148-023-00816-y
229. Mizerna, K.; Król, A. The importance of time and other determinants in the assessment of heavy metals release during solid waste management. **2023**, Scientific Reports, 13(1). https://doi.org/10.1038/s41598-023-28926-0
230. Gu, X.; Ling, Y. Characterization and properties of Chinese red clay for use as ceramic and construction materials. **2024**, Science Progress, 107(1). https://doi.org/10.1177/00368504241232534
231. EL Khazanti, F.; Rachid, A.; El Ouahabi, M.; Nasri, H.; Azerkane, D.; Et-Tayea, Y.; Gharibi, E. K. Valorization of Iron Ore Tailings from Nador, Morocco, as a Sustainable Additive in the Manufacture of Red Clay Fired Bricks. **2024**, Journal of Ecological Engineering, 25(7), 137–150. https://doi.org/10.12911/22998993/187956

Disclaimer/Publisher's Note: The statements, opinions and data contained in all publications are solely those of the individual author(s) and contributor(s) and not of MDPI and/or the editor(s). MDPI and/or the editor(s) disclaim responsibility for any injury to people or property resulting from any ideas, methods, instructions or products referred to in the content.

© 2026 by the author(s). Distributed under a Creative Commons CC BY license.